The Pennsylvania State University
The Graduate School

TOPOLOGICAL PHOTONIC CRYSTALS IN ONE, TWO AND THREE DIMENSIONS

A Dissertation in
Physics
by
Sachin Vaidya

Submitted in Partial Fulfillment
of the Requirements
for the Degree of

Doctor of Philosophy

May 2023

The dissertation of Sachin Vaidya was reviewed and approved by the following:

Mikael C. Rechtsman
Downsbrough Early Career Development Professor of Physics
Dissertation Advisor
Chair of Committee

Chaoxing Liu
Professor of Physics

Eric Hudson
Associate Professor of Physics
Associate Head for Diversity and Equity

Noel Christopher Giebink
Professor of Electrical Engineering

Nitin Samarth
Professor of Physics
George A. and Margaret M. Downsbrough Department Head

Abstract

The recent discovery of topological phases of matter has revolutionized our understanding of condensed matter systems. The information that describes these phases is stored across the entire system, and as a result, some of their properties are protected from local perturbations. These systems exhibit unique phenomena such as transport channels that exist on their boundaries and features that are robust to disorder. Topological phases were first discovered in condensed matter physics but the underlying principles were soon extended to many wave systems such as photonic and acoustic systems. The field of topological photonics aims to both realize novel topological phases in photonic systems and develop applications based on their robust properties.

This dissertation aims to further our understanding of topological photonics and lies at the intersection between photonic crystals and topological band theory. In the first two parts of this dissertation, we present two studies that experimentally realize charge-2 Weyl points and observe their splitting in three-dimensional chiral woodpile photonic crystals. This is done at technologically-useful infrared wavelengths by using a state-of-the-art 3D micro-printing technique that employs low loss materials.

In the next two parts, we focus on developing a complete topological classification of bands in one- and two-dimensional photonic crystals under crystalline symmetries. Based on this classification, we propose a strategy to diagnose and design a wide variety of topological photonic crystals. We then use this framework to show that Chern insulators can have a meaningful notion of relative polarization whose effects can be seen at the boundary between two Chern insulators with the same Chern number.

In the last two parts, we explore miscellaneous topics in photonic crystals. In the first of the two parts, we theoretically predict bound states in the continuum that are localized to point defects in two-dimensional photonic crystals. This allows for the confinement of light in the absence of photonic bandgaps. In the last part, we present the observation of a localization transition in one-dimensional photonic quasicrystals. In addition, we observe a surprising phenomenon that occurs in this system, a second transition of some states to a delocalized regime upon further increasing the quasiperiodic disorder.

Table of Contents

List of Figures

List of Tables

Acknowledgments

First and foremost, I would like to express my immense gratitude to my advisor and academic parent, Prof. Mikael C. Rechtsman, who has been a constant source of guidance, support, and encouragement throughout my time at Penn State. Through his mentorship, I learned the importance of having a broad perspective of physics which lead me to undertake both theoretical and experimental projects spanning a wide range of topics. I also learned several valuable lessons that helped me successfully navigate the challenges of academia which I will carry with me for the rest of my life. I am also grateful to Prof. Chao-xing Liu, Prof. Noel C. Giebink, and Prof. Eric Hudson for serving on my dissertation committee and for their helpful comments.

My research could not have been possible without significant contributions from my collaborators. In particular, I would like to thank the incredibly talented and knowledgeable postdocs who I worked with and had the opportunity to learn from: Alexander Cerjan, Wladimir A. Benalcazar, and Christina Jörg. Alex was one of my earliest mentors along with Mikael and patiently taught me everything about photonic crystals while always entertaining my questions and curiosities. From Wladimir, I learned about topological systems and how to approach problems with rigor and depth. Christina always kept me grounded by teaching me the importance of being aware of the experimental viability of my theoretical ideas. It is from her that I truly learned to enjoy undertaking experimental challenges. I would also like to thank Jiho Noh and Marius Jürgensen, with whom I enjoyed working and discussing many ideas. I feel very fortunate to have shared some of the most exciting moments of my graduate school research with these people.

I also owe a lot of gratitude to the other members of my research group and my cohort who provided much-needed camaraderie during the first few difficult years of graduate school. I had the privilege of learning from a few great physics and mathematics teachers during my time at Penn State and at the University of Hyderabad, to whom I am eternally grateful. Without the solid foundation that they provided, I would not

have been able to tackle difficult research problems in graduate school.

I am extremely grateful to Debadarshini Mishra for her companionship through all the highs and lows of life. Her unwavering support has been instrumental to my success. Lastly, I would like to give special thanks to my parents, Sharada Vaidya and Shashank Vaidya, and to Anna for always believing in me and encouraging me to pursue my dreams.

The work presented in this dissertation was supported by the Office of Naval Research (ONR) YIP program under Grant No. N00014-18-1-2595; the Packard foundation under Fellowship No. 2017-66821; Penn State NSF-MRSEC Center for Nanoscale Science, under Grant No. DMR1420620; Office of Naval Research (ONR) Multidisciplinary University Research Initiative (MURI) under Grand No. N00014-20-1-2325 on Robust Photonic Materials with Higher-Order Topological Protection; Charles E. Kaufman Foundation under Grant No. KA2020-114794 as well as the U.S. Army Research Office MURI under Grant No. W911NF22-2-0103. Any opinions, findings, conclusions, or recommendations expressed in this dissertation are those of the author and do not necessarily reflect the views of the funding agencies.

Further financial support was provided through various Pennsylvania State University fellowships including the Homer F. Braddock Fellowship, Troxell Scholarship in Physics, Downsbrough and David C. Duncan Graduate Fellowships, and the David H. Rank Memorial Physics Award.

Chapter 1
Introduction

1.1 Overview

We begin with a brief review of photonic crystals and their mathematical treatment, followed by a review of some concepts from topological band theory that are central to this dissertation. For additional details, see [3–5].

1.2 Photonic Crystals

Photonic crystals (PhCs) are periodic arrangements of dielectric materials that allow for optical control and manipulation of light. The periodic dielectric profile in PhCs is analogous to a periodic potential that is experienced by electrons in a solids and therefore, many concepts from solid-state physics can be used to analyze and study PhCs. Here, we will focus on systems where the dielectric permittivity is a scalar function of spatial coordinates and the magnetic permeability of all materials is set to that of vacuum. Under the further assumptions that the system is linear, the materials are isotropic and that any frequency dependence of the dielectric function can be ignored, we can write down the source-free Maxwell's equations as:

$$\begin{aligned} \nabla \cdot \mathbf{H}(\mathbf{r}, t) &= 0 \\ \nabla \times \mathbf{E}(\mathbf{r}, t) + \mu_0 \frac{\partial}{\partial t} \mathbf{H}(\mathbf{r}, t) &= 0 \\ \nabla \cdot [\epsilon(\mathbf{r}) \mathbf{E}(\mathbf{r}, t)] &= 0 \\ \nabla \times \mathbf{H}(\mathbf{r}, t) - \epsilon_0 \epsilon(\mathbf{r}) \frac{\partial}{\partial t} \mathbf{E}(\mathbf{r}, t) &= 0. \end{aligned} \tag{1.1}$$

where $\mathbf{H}$ and $\mathbf{E}$ are the magnetic and electric fields respectively, $\epsilon(\mathbf{r})$ is the dielectric function, and ϵ_0 and μ_0 are the vacuum permittivity and permeability respectively. We next express the fields as spatial harmonic modes multiplied by a complex exponential in time as $\mathbf{H}(\mathbf{r},t) = \mathbf{H}(\mathbf{r})e^{-i\omega t}$ and $\mathbf{E}(\mathbf{r},t) = \mathbf{E}(\mathbf{r})e^{-i\omega t}$. The divergence equations impose a transversality requirement for the solutions, i.e. that the field oscillations are perpendicular to the direction of propagation. Keeping this in mind, the fields are described by two second-order equations:

$$\begin{aligned} \nabla \times \left(\frac{1}{\epsilon(\mathbf{r})} \nabla \times \mathbf{H}(\mathbf{r}) \right) &= \left(\frac{\omega}{c} \right)^2 \mathbf{H}(\mathbf{r}) \\ \nabla \times \nabla \times \mathbf{E}(\mathbf{r}) &= \left(\frac{\omega}{c} \right)^2 \epsilon(\mathbf{r}) \mathbf{E}(\mathbf{r}). \end{aligned} \tag{1.2}$$

The first equation above leads to an eigenvalue problem for the magnetic field $\mathbf{H}$ and its corresponding frequency eigenvalue ω. The differential operator $\nabla \times ([1/\epsilon(\mathbf{r})]\nabla\times)$ is linear, Hermitian and positive semi-definite. The second equation is a generalized eigenvalue problem for the electric field $\mathbf{E}$. We can choose to solve for just one of these fields, usually the magnetic field, and compute the other field from the appropriate Maxwell's equation.

Type	Photonic system
HHH	Homogeneous medium
HHF	Homogeneous dielectric slab
HFF	Dielectric waveguide
HHP	1D PhC
HPP	2D PhC, 2D PhC fiber
HPF	1D PhC slab
PPP	3D PhC
PPF	2D PhC slab
PFF	Periodic dielectric waveguide
FFF	Dielectric resonator

Table 1.1. Various photonic systems depending on the whether they possess homogeneous, periodic or finite dimensions

The dielectric function $\epsilon(\mathbf{r})$ can describe a variety of photonic systems depending on the exact combination of homogeneous (H), periodic (P) or finite (F) dimensions that the system possesses as shown in Table 1.1. The analysis of these systems can be simplified

by exploiting translational symmetry along homogeneous or periodic dimensions. Along homogeneous dimensions the system has continuous translational symmetry and the solutions in those dimensions take the form of plane waves with a well-defined wavevector (or momentum). Along periodic dimensions, the system has discrete translational symmetry and the solutions in those dimensions take the form of plane waves modulated by a periodic envelope. This is commonly known as Bloch's theorem. In this case, the solutions are characterized by a quasi wavevector (or quasi momentum) whose values are restricted to a finite range called the Brillouin zone. If a system has one or more finite dimensions and is surrounded by vacuum, in- and out-coupling of light becomes an important consideration.

1.2.1 1D, 2D and 3D photonic crystals

A 1D PhC is characterized by a dielectric profile that is periodic along one direction (x) and is uniform along the other two directions (y and z). The magnetic field eigenmode can therefore be written as a plane wave solution in the y, z plane multiplied by an x-dependent vector field, $\mathbf{H}(\mathbf{r}) = e^{i\mathbf{k}_\parallel \cdot \boldsymbol{\rho}}\mathbf{h}(x)$, where $\mathbf{k}_\parallel$ is the momentum along the uniform directions and $\boldsymbol{\rho} = y\hat{\mathbf{y}} + z\hat{\mathbf{z}}$. However, when we are only concerned with propagation along the periodic direction, $\mathbf{k}_\parallel = 0$. Moreover, since the fields must be perpendicular to the propagation direction, we can define two orthogonal polarizations where the vector fields lie in the y, z plane. Without loss of generality and assuming isotropy, we can take these polarized fields to be $\mathbf{h_z}(x) = h_z(x)\hat{\mathbf{z}}$ and $\mathbf{h_y}(x) = h_y(x)\hat{\mathbf{y}}$. This leads to the following 1D eigenvalue problem for the scalar fields, $h_{\xi=y,z}(x)$,

$$\hat{\Theta}_1 h_\xi(x) = \left(\frac{\omega}{c}\right)^2 h_\xi(x), \quad \hat{\Theta}_1 \equiv -\partial_x \left(\frac{1}{\epsilon(x)}\partial_x\right), \tag{1.3}$$

where $\hat{\Theta}_1$ is the 1D Maxwell operator that plays a role analogous to the Hamiltonian in quantum mechanics. By exploiting the periodicity of the dielectric function, the above equation can be solved using Bloch's theorem. Specifically, the ansatz given by $h_{\xi,n,k_x}(x) = e^{ik_x x}u_{\xi,n,k_x}(x)$, can be used to solve (1.3), where $u_{\xi,n,k_x}(x)$ is the periodic part of the field defined over a unit cell and k_x is the quasi momentum along the x-direction. This yields field solutions distributed across discrete frequency bands labeled by the index n and with their quasi momentum, k_x, restricted to lie within the first BZ. It will

also be useful to define the inner product between two fields over a unit cell (UC) as

$$\langle u_{\xi,n_1,k_1}|u_{\xi,n_2,k_2}\rangle = \int_{\mathrm{UC}} u^*_{\xi,n_1,k_1}(x)u_{\xi,n_2,k_2}(x)\mathrm{d}x. \tag{1.4}$$

2D PhCs consist of a periodic patterning of the dielectric along two directions (x and y) and a uniform dielectric profile along the third direction (z), with wave propagation restricted to lie in the x, y plane. For such a system, the equations in (1.2) can be simplified by exploiting the mirror symmetry through the x, y plane that sends $z \to -z$. This separates the states into two orthogonal polarizations: transverse electric (TE) with $\mathbf{E}(\mathbf{r}) = \mathcal{E}_x(x,y)\hat{\mathbf{x}}+\mathcal{E}_y(x,y)\hat{\mathbf{y}}$, $\mathbf{H}(\mathbf{r}) = \mathcal{H}_z(x,y)\hat{\mathbf{z}}$, which is even under the mirror symmetry, and transverse magnetic (TM) with $\mathbf{E}(\mathbf{r}) = \mathcal{E}_z(x,y)\hat{\mathbf{z}}$, $\mathbf{H}(\mathbf{r}) = \mathcal{H}_x(x,y)\hat{\mathbf{x}} + \mathcal{H}_y(x,y)\hat{\mathbf{y}}$, which is odd under the mirror symmetry. For these generally non-degenerate TE and TM polarizations, the problem is most easily solved for the scalar fields $\mathcal{H}_z(x,y)$ and $\mathcal{E}_z(x,y)$ respectively, using [4]

$$\begin{aligned} -\left[\frac{\partial}{\partial x}\frac{1}{\varepsilon(x,y)}\frac{\partial}{\partial x} + \frac{\partial}{\partial y}\frac{1}{\varepsilon(x,y)}\frac{\partial}{\partial y}\right]\mathcal{H}_z(x,y) =& \frac{\omega^2}{c^2}\mathcal{H}_z(x,y) \\ -\frac{1}{\varepsilon(x,y)}\left[\frac{\partial^2}{\partial x^2} + \frac{\partial^2}{\partial y^2}\right]\mathcal{E}_z(x,y) =& \frac{\omega^2}{c^2}\mathcal{E}_z(x,y) \end{aligned} \tag{1.5}$$

These equations can be succinctly written as

$$\begin{aligned} \hat{\Theta}_{2,\mathbf{TE}}\mathcal{H}_z(x,y) =& \frac{\omega^2}{c^2}\mathcal{H}_z(x,y) \\ \hat{\Theta}_{2,\mathbf{TM}}\mathcal{E}_z(x,y) =& \frac{\omega^2}{c^2}\mathcal{E}_z(x,y) \end{aligned} \tag{1.6}$$

Similar to the 1D case, these eigenvalue problems can be solved using Bloch's theorem using the ansatz: $\mathcal{H}_z(x,y) = e^{i\mathbf{k}\cdot\mathbf{r}}u_{\mathbf{TE},n,\mathbf{k}}(x,y)$ (for TE) and $\mathcal{E}_z(x,y) = e^{i\mathbf{k}\cdot\mathbf{r}}u_{\mathbf{TM},n,\mathbf{k}}(x,y)$ (for TM). The solutions are distributed into frequency bands with their momenta ($\mathbf{k}$), being restricted to the first 2D BZ. The inner products between the fields take the form

$$\begin{aligned} \langle u_{\mathbf{TE},n_1,\mathbf{k}_1}|u_{\mathbf{TE},n_2,\mathbf{k}_2}\rangle &= \int_{\mathrm{UC}} u^*_{\mathbf{TE},n_1,\mathbf{k}_1}(x,y)u_{\mathbf{TE},n_2,\mathbf{k}_2}(x,y)\mathrm{d}^2\mathbf{r} \\ \langle u_{\mathbf{TM},n_1,\mathbf{k}_1}|u_{\mathbf{TM},n_2,\mathbf{k}_2}\rangle &= \int_{\mathrm{UC}} \varepsilon(x,y)u^*_{\mathbf{TM},n_1,\mathbf{k}_1}(x,y)u_{\mathbf{TM},n_2,\mathbf{k}_2}(x,y)\mathrm{d}^2\mathbf{r} \end{aligned} \tag{1.7}$$

where $u_{\mathbf{TE},n,\mathbf{k}}(x,y)$ is the periodic part of the scalar field $\mathcal{H}_z(x,y)$ (for TE) and $u_{\mathbf{TM},n,\mathbf{k}}(x,y)$ is the periodic part of the scalar field $\mathcal{E}_z(x,y)$ (for TM).

3D PhCs consist of a periodic patterning of the dielectric in all three directions of space and we are required to solve for the full vectorial fields in (1.2). As before, the eigenvalue problem can be solved using Bloch's theorem by the following ansatz for the magnetic and electric fields respectively: $\mathbf{H}(\mathbf{r}) = e^{i\mathbf{k}\cdot\mathbf{r}}\mathbf{u}_{\mathbf{H},n,\mathbf{k}}(\mathbf{r})$, $\mathbf{E}(\mathbf{r}) = e^{i\mathbf{k}\cdot\mathbf{r}}\mathbf{u}_{\mathbf{E},n,\mathbf{k}}(\mathbf{r})$. The inner products are then given by

$$\begin{aligned}\langle \mathbf{u}_{\mathbf{H},n_1,\mathbf{k}_1} | \mathbf{u}_{\mathbf{H},n_2,\mathbf{k}_2} \rangle &= \int_{\mathrm{UC}} \mathbf{u}^*_{\mathbf{H},n_1,\mathbf{k}_1}(\mathbf{r}) \cdot \mathbf{u}_{\mathbf{H},n_2,\mathbf{k}_2}(\mathbf{r}) \mathrm{d}^3\mathbf{r} \\ \langle \mathbf{u}_{\mathbf{E},n_1,\mathbf{k}_1} | \mathbf{u}_{\mathbf{E},n_2,\mathbf{k}_2} \rangle &= \int_{\mathrm{UC}} \varepsilon(\mathbf{r}) \mathbf{u}^*_{\mathbf{E},n_1,\mathbf{k}_1}(\mathbf{r}) \cdot \mathbf{u}_{\mathbf{E},n_2,\mathbf{k}_2}(\mathbf{r}) \mathrm{d}^3\mathbf{r}\end{aligned} \tag{1.8}$$

1.3 Topological systems

In this section, we briefly review central concepts relevant to the study of topological systems. More details can be found in [5].

1.3.1 Berry phase, Berry curvature and Chern number

Consider a single isolated band of a 1D PhC with the periodic part of its field eigenmode given by $|u_{n,k}\rangle$. The relative phase between eigenmodes at two different momentum points k_1 and k_2 is given by

$$e^{i\theta_{12}} = \frac{\langle u_{n,k_1} | u_{n,k_2} \rangle}{|\langle u_{n,k_1} | u_{n,k_2} \rangle|}. \tag{1.9}$$

If we choose a closed contour in k-space that is discretized into N points, k_1, k_2, ..., k_N (and $k_{N+1} = k_1$), the phase accumulated on this contour is given by

$$e^{i\theta_B} = e^{i(\theta_{12}+\theta_{23}+\ldots+\theta_{N1})} \tag{1.10}$$

θ_B is a gauge-invariant quantity called the Berry phase. In the continuous limit of this discretization, the Berry phase can be expressed in terms of an integral over the Berry connection, $\mathcal{A}(k) = -i\langle u_{n,k} | \partial_k u_{n,k} \rangle$ along a closed contour $\mathcal{C}$ as

$$\theta_B = \oint_{\mathcal{C}} \mathcal{A}(k) \mathrm{d}k. \tag{1.11}$$

The Berry connection and the Berry phase can be generalized to higher dimensions: $\mathcal{A}(\mathbf{k}) = -i\langle \mathbf{u}_{n,\mathbf{k}} | \nabla_{\mathbf{k}} \mathbf{u}_{n,\mathbf{k}} \rangle$, $\theta_B = \oint_{\mathcal{C}} \mathcal{A}(\mathbf{k}) \cdot \mathrm{d}\mathbf{k}$. The Berry connection encodes information about a state's adiabatic transport in momentum space. The Berry phase then measures the holonomy or phase acquired due to the "parallel" transport of a state along a closed contour. Under inversion symmetry that sends $\mathbf{r} \to -\mathbf{r}$, the value of Berry phase is quantized to 0 or π, due to which the Berry phase can serve as a topological invariant for such systems.

Instead of working with extended Bloch states, it is sometimes useful to switch to a basis of localized states by taking an inverse Fourier transform. These localized states also form a basis and are called Wannier functions. In 1D, they are given by

$$|w_{n,x_0}\rangle = \frac{a}{2\pi} \int_{\mathrm{BZ}} e^{-ikx_0} |u_{n,k}\rangle \mathrm{d}k \tag{1.12}$$

It can then be shown that the center of a Wannier function, defined as the diagonal position operator matrix element, is related to the Berry phase via

$$\tilde{x}_n = \langle w_{n,0} | x | w_{n,0} \rangle = \frac{a}{2\pi} \theta_B. \tag{1.13}$$

This remarkable fact implies that the center of a Wannier function, referred to as a "Wannier center", is a gauge-invariant quantity. In solids, the Wannier center is the location in each unit cell where the electronic charge density is sharply peaked. The Wannier basis is therefore useful for defining concepts such as dipole moments and polarization in solids. We shall see in future chapters that despite the lack of electronic charges in PhCs, the Wannier centers are related to topological effects and observable quantities.

In a 2D parameter space, such as a 2D Brillouin zone, the states of the system can be used to define a generalized notion of a gauge-invariant curvature over this space. This is known as the Berry curvature, which can be derived from the Berry connection as

$$\Omega(\mathbf{k}) = \nabla_{\mathbf{k}} \times \mathcal{A}(\mathbf{k}) \tag{1.14}$$

The Berry curvature integrated over a closed surface, usually taken to be the 2D Brillouin zone, is an integer called the Chern number:

$$C = \frac{1}{2\pi} \iint_{\mathrm{BZ}} \Omega(\mathbf{k}) \cdot \mathrm{d}^2\mathbf{k} \tag{1.15}$$

The Chern number is a $\mathbb{Z}$ invariant that topologically characterizes the bands and is at the heart of many physical phenomena in condensed matter physics such as the quantum Hall effect. Under time-reversal symmetry, the Berry curvature is odd and the Chern number vanishes. Therefore, for bands in 2D with non-zero Chern numbers, the breaking of time-reversal symmetry is required.

The value of the Berry curvature a given point is equal to the limiting value of the Berry phase acquired on a loop that encircles and shrinks to this point. Due to this Stokes-theorem relationship, the Chern number can also be inferred from the winding number of the Berry phase when computed as a function of one direction in momentum space. Since the Berry phase is directly related to the locations of the Wannier centers, a winding in the Berry phase indicates that the notion of Wannier centers is ill-defined for bands with Chern numbers.

1.4 Outline

The rest of the dissertation is organised as follows: in chapter 2 and 3, we present experimental studies on the realization of charge-2 Weyl points in 3D chiral woodpile PhCs and the observation of its splitting under symmetry breaking. In chapter 4, we develop a complete topological classification of bands in 1D and 2D PhCs under crystalline symmetries. In chapter 5, we use this classification to show that Chern insulators can have a well-defined notion of relative polarization, despite not having Wannier centers. We demonstrate the boundary manifestations of this relative polarization using a 2D Chern PhC. In Chapter 6, we show that point defects in 2D PhCs can support bound states in the continuum, allowing for light confinement without the requirement of a photonic bandgap. In chapter 7, we explore localization and delocalization transitions in 1D photonic quasicrystals.

Chapter 2
Charge-2 Weyl points in chiral woodpile photonic crystals

In this chapter, we discuss our experimental observation of a charge-2 Weyl point in a three-dimensional chiral woodpile photonic crystal. The exploration of three-dimensional topological photonic crystals has always been somewhat challenging due to the lack of flexible fabrication methods. Here, we employ a state-of-the-art 3D micro-printing technique to fabricate chiral woodpile structures that host charge-2 Weyl points at near- and mid-infrared wavelengths. This chapter is based on work that was done in collaboration with Jiho Noh, Alexander Cerjan, Christina Jörg, Georg von Freymann and Mikael C. Rechtsman [6].

2.1 Overview

Over the past decade, topological materials have been studied extensively in the hopes of harnessing properties such as protection from defects and scatter-free transport. The simplest topological systems in three dimensions are Weyl materials, which possess a set of point degeneracies in momentum space that act as sources of Berry curvature [7], and are thus topologically protected against perturbations to the system. In this sense, Weyl points are analogous to magnetic monopoles in momentum space and are associated with a quantized topological charge. A direct consequence of their non-zero charge is that perturbations that preserve periodicity cannot cause a gap to open at the Weyl point but merely move it around in the band structure. Moreover, these materials exhibit remarkable surface states that lie on Fermi arcs connecting Weyl points of opposite charges. The necessary conditions for the existence of Weyl points are very general and only require breaking either inversion symmetry, time-reversal symmetry or both.

Since this can happen in a wide range of systems, Weyl points have been shown to exist in solids [8–15], microwave [16,17] and optical photonic crystals (PhC) [18], optical waveguide arrays [19,20], circuit-based systems [21], mechanical crystals [22], phononic crystals [23,24], metamaterials [25], magnetized plasmas [26] and can also be realized using synthetic dimensions [27].

If a Weyl material has additional spatial symmetries, it is possible for multiple Weyl points of the same charge and between the same two bands to accumulate at high symmetry points in the Brillouin zone leading to Weyl points with a higher topological charge [28,29]. For example, a parity-breaking chiral woodpile PhC made of stacked layers of dielectric rods (n = 3.4) has been predicted to have charge-2 Weyl points [30] that form due to the presence of a screw symmetry. This symmetry pins the location of the ± 2 charges to high symmetry points in the Brillouin zone of the PhC [29], which implies that as long as the required spatial symmetries are present, these charge-2 Weyl points must continue to exist regardless of index contrast. While other studies report findings of higher-charged Weyl points, their implementations are limited to macroscopic metallic PhCs that work in microwave frequencies [31] and acoustic structures [32].

In this chapter, we report the experimental observation of a charge +2 Weyl point in the mid-infrared regime in a low-index (n = 1.52) chiral woodpile PhC fabricated by two-photon polymerization and characterized using angle-resolved Fourier-transform infrared (FTIR) spectroscopy. For such a low index contrast, there is only an incomplete bandgap surrounding the Weyl point. Nevertheless, we show that this is sufficient to directly observe the dispersion features associated with the Weyl point in the reflection spectrum of the PhC. Furthermore, we numerically show the existence of topological surface resonances, akin to Fermi arc states, associated with Weyl points that satisfy the bulk-boundary correspondence in the absence of a bandgap. The prospect of lowering the index contrast requirements for topological photonic structures is of importance since it can allow for readily accessible fabrication techniques such as colloidal self-assembly and two-photon polymerization as well as wider material choices.

2.2 Results

2.2.1 Chiral woodpile photonic crystal band structure

The specific PhC we use to realize a charge +2 Weyl point is a chiral woodpile as shown in Fig. 2.1 (a), whose 3D unit cell consists of four layers of rectangular rods stacked on top

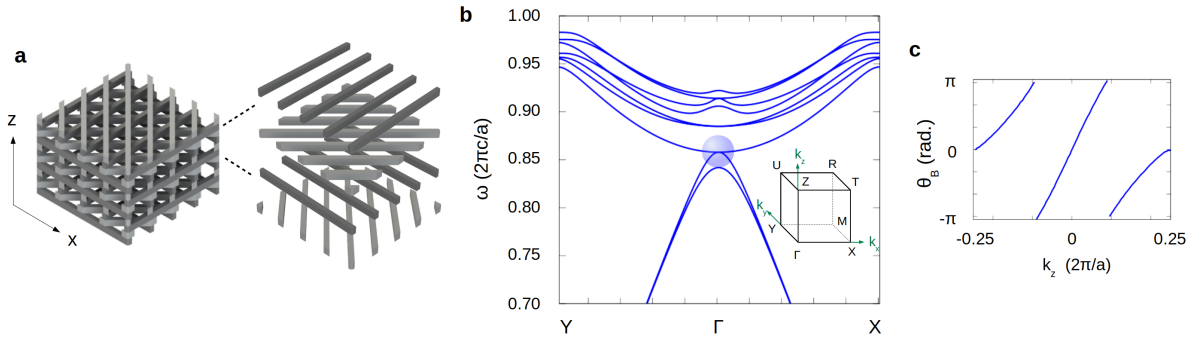

Figure 2.1. (a) The chiral woodpile structure made by stacking layers of rods with an in-plane rotation of 45° between layers. (b) Band structure along $\mathbf{Y}-\mathbf{\Gamma}-\mathbf{X}$ showing bands 3 to 11. The Weyl point of interest is the degeneracy between bands 4 and 5 at $\mathbf{\Gamma}$ (blue circle). The 3D Brillouin zone of the PhC is shown in the inset. (c) Berry phase plot for band 4 around the $\mathbf{\Gamma}$ point. The double winding indicates that the degeneracy has a topological charge of 2.

of each other with a relative 45° in-plane rotation. The width and height of the rods are $0.175a$ and $0.25a$ respectively, where a is the lattice constant in all three directions. The spacing between the rods in the 45° and 135° layers is $a/\sqrt{2}$. The rods have a dielectric constant ($\varepsilon_{\text{rods}}$) of 2.31, which corresponds to the material used in the experiment [33]. Using these parameters, the band structure of our PhC is numerically calculated using MIT Photonic Bands (MPB) [2], and bands 3 to 11 along $\mathbf{Y}-\mathbf{\Gamma}-\mathbf{X}$ are shown in Fig. 2.1 (b). The degeneracy at $\mathbf{\Gamma}$ between bands 4 and 5 is the Weyl point of interest. These bands along $\mathbf{\Gamma}-\mathbf{Z}$ direction in the Brillouin zone are very close in frequency but convergence tests show that the degeneracy only occurs at the $\mathbf{\Gamma}$ point.

2.2.2 Berry phase winding around the Weyl points

To confirm the topological nature of this degeneracy, we directly calculate its topological charge (Chern number) by using a discrete algorithm to compute Berry phase (θ_B) given in Ref. [34]. The phase is calculated using magnetic field eigenmodes from MPB on contours that are defined by constant k_z and enclose the Weyl point. The topological charge of the Weyl point is the number of times the phase winds around as a function of k_z as shown in Fig. 2.1 (c). A second Weyl point of charge -2 between the same two bands is located at the $\mathbf{R}$ point in the Brillouin zone, which exhibits double winding of Berry phase in the opposite sense as shown in Fig. Fig. 2.2 (d). Since this Weyl point is located below the light line of air and as such is inaccessible without the use of gratings or high-index fluids, we will focus on the Weyl point at $\mathbf{\Gamma}$ in our experiment.

The Berry phase is calculated on circular contours that lie on constant k_z planes as

shown in Fig. 2.2 (b). The topological charge of the Weyl point is the number of times the Berry phase winds as a function of k_z.

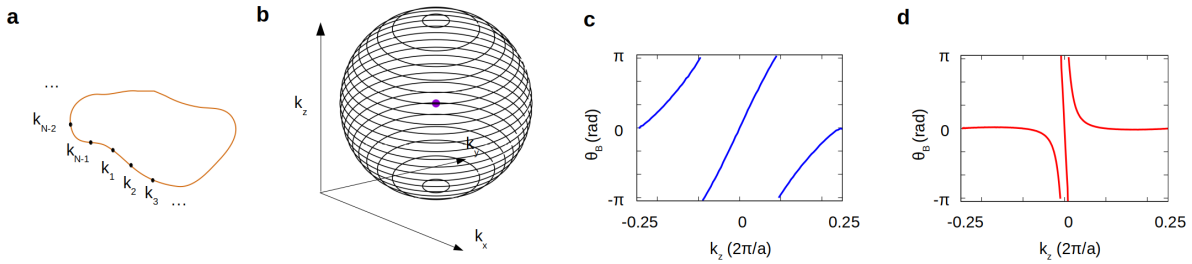

Figure 2.2. (a) Closed contours in k-space discretized into N points. (b) The Berry phase is calculated on circular contours that enclose the Weyl point. Each contour lies on a constant k_z plane. (c), (d) Berry phase vs. k_z plots for charge $+2$ and charge -2 Weyl points at $\mathbf{\Gamma}$ and $\mathbf{R}$ respectively.

2.2.3 Experimental results

For the experiment, we fabricate the chiral woodpile PhC by 3D lithography (direct laser writing, DLW [35]) using a DLW instrument (Photonic Professional GT, Nanoscribe GmbH), which employs two-photon-polymerization of a liquid negative tone photoresist (IP-DIP, Nanoscribe GmbH) (n = 1.52). Here, we use DLW in dip-in configuration [36], where the microscope objective (63x, NA=1.4) for DLW is dipped into the photoresist which is applied below the fused-silica substrate. The 3D structure is then written layer by layer starting from the bottom surface of the substrate by moving the microscope objective in z-direction. The structure is developed in propylene glycol monomethyl ether acetate (PGMEA) for 20 minutes and then developed in isopropanol for 3 minutes. The thickness of the rods is controlled by varying number of superpositions of individual laser writing for each rod [37]. The sample has a lattice constant of 4 μm and rod width and height equal to 700 nm and 1 μm respectively. We fabricate 20 unit cells in the z-direction (80 layers) and 250 unit cells in x- and y-directions. An image of one such sample taken by field emission scanning electron microscopy (FESEM) is shown in Fig. 2.3.

Reflection measurements are carried out using the Bruker Vertex 80 FTIR spectrometer at wavelengths ranging from $4.2-6$ μm with the frequency resolution set to 8 cm^{-1}. A variable angle reflection accessory (Seagull) is used to observe the angle-resolved spectra from 0° to 15° along the $\mathbf{\Gamma}-\mathbf{X}$ direction with a resolution of 1°. The data for $-15°$ to 0° is identical to the data for the corresponding positive angles since the structure is

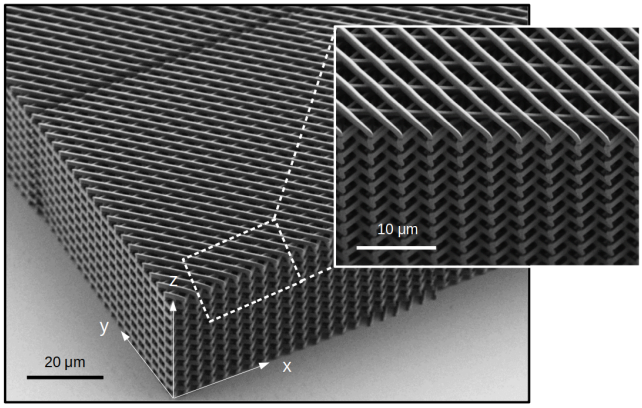

Figure 2.3. FESEM image of a parity-breaking chiral woodpile fabricated using two-photon polymerization.

invariant under 180° rotational symmetry about the z-axis and hence we only measure data for positive angle and reflect it for negative angles. A polarizer is used at the output port to obtain spectra for 0° (s-), 45° and 90° (p-) polarizations. The spectrum is normalized to the maximum value of reflection for each angle and interpolated. The results from the experiment are shown in Fig. 2.4 (a), (b) and (c). We also numerically simulate the reflection spectrum using rigorous coupled-wave analysis (RCWA) as implemented in Stanford Stratified Structure Solver (S^4) [38] where periodic boundary conditions are imposed in the lateral directions and the structure is finite in the z direction having 20 unit cells. The simulation results are shown in Fig. 2.4 (d), (e) and (f) for comparison. As can be seen, the simulated and experimentally measured spectra match very well and show sharp quadratic boundaries separating reflective and transmissive regions that match each of the two relevant bulk Weyl bands in orthogonal polarizations. As expected, the measurement for 45° polarization is a superposition of measurements for s- and p-polarizations and shows clear signatures from both bands forming the Weyl point at the degeneracy.

To provide additional evidence for the robust symmetry protection of the Weyl point, we fabricate and measure another sample with significantly different parameters: rod width of 300 nm and lattice constant of 2.1 μm. Fig 2.5 (a) shows a SEM image of the sample, along with its transmission spectra. In this case, the transmission measurement was performed using the Hyperion 3000 microscope attached to the FTIR with the in-coupling Cassegrain objective covered except for a small pinhole of 2 mm diameter. This resulted in better k-space resolution for the measurement. We see in Fig. 2.5 (b) that the charge +2 Weyl point continues to exist, even for these different parameters,

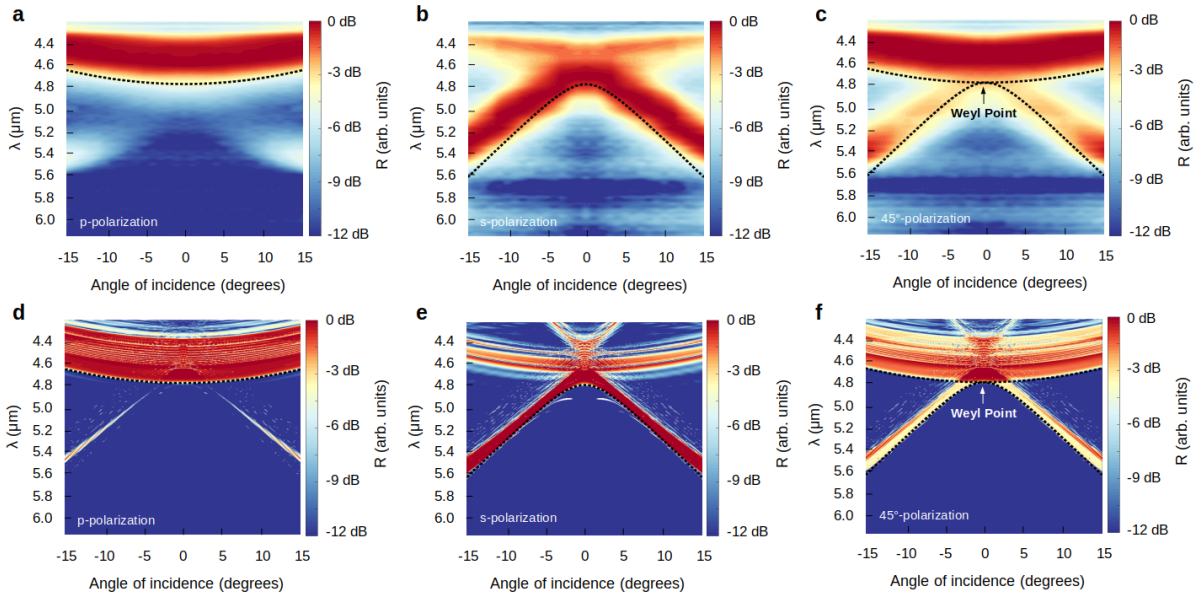

Figure 2.4. (a), (b), (c) Experimentally measured angle-resolved FTIR reflection spectra for 90° (p-), 0° (s-) and 45° polarizations respectively. The dotted lines in all plots are Weyl bulk bands from MPB. (d), (e), (f) S^4 (RCWA) simulation of the angle-resolved reflection spectra for all three polarizations.

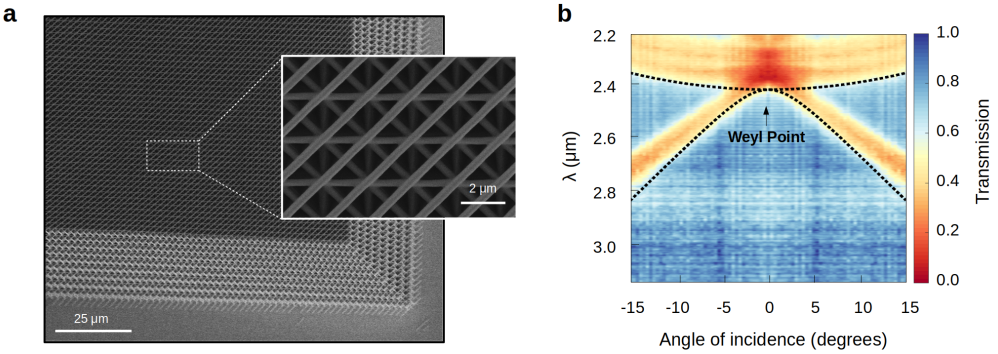

Figure 2.5. (a) A SEM image of the chiral woodpile PhC with rod width of 300 nm and lattice constant 2.1 μm. (b) Experimentally measured transmission spectrum in the $\mathbf{\Gamma - X}$ direction for the PhC shown in (a), overlaid with the bands calculated from MPB shown using black dotted lines.

and now resides at a wavelength of 2.4 μm.

2.2.4 Coupling coefficients between incident plane waves and photonic crystal Bloch modes

Since the PhC investigated here has low index-contrast, there is no complete band gap around the Weyl point, and therefore this relatively unobscured direct observation

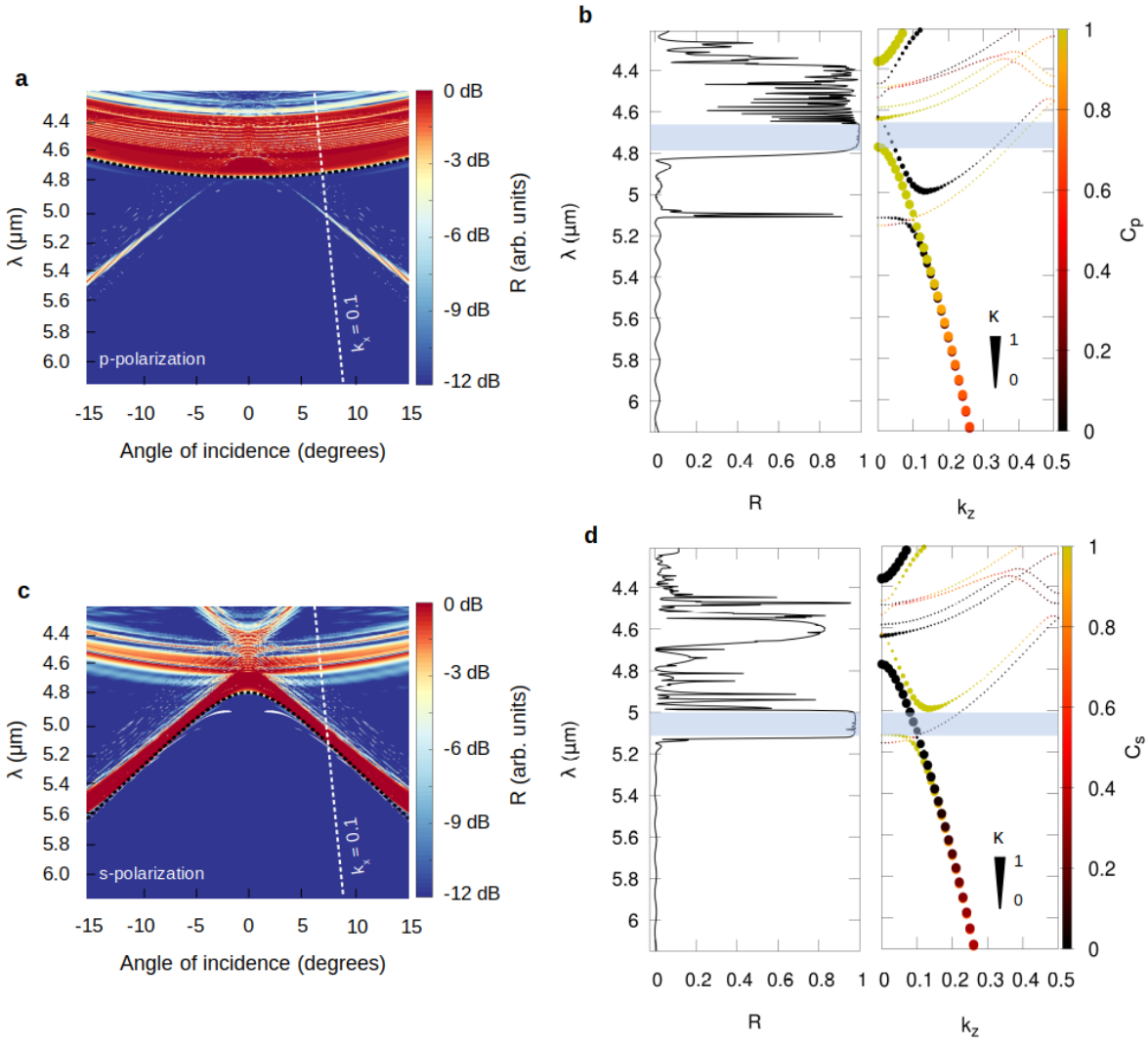

Figure 2.6. (a), (c) Angle-resolved RCWA simulation of reflection spectra for p and s polarizations respectively as shown in Fig. 3 of the main text. (b), (d) Reflection spectrum along the cut shown by the dashed line in (a) and (c) and the band structure showing bands 3 to 12 for $\mathbf{k} = (0.1, 0, 0)$ to $(0.1, 0, 0.5)$ $(2\pi/a)$. The color of the circular dots indicates the value of $C_{s/p}$ for the corresponding Bloch modes and their size is proportional to the value of κ.

warrants further explanation. When probing reflection through the chiral woodpile, we make the assumption that the sample is effectively infinite in the x and y directions (parallel to the surface) and truncated in the z-direction; we thus examine the projected band structure, since k_z is no longer conserved (but k_x and k_y still are). As such, the projected band structure consists of states with both $k_z = 0$ and $k_z \neq 0$ projected onto the (k_x, k_y) plane. Thus, even though the Weyl point exists in an incomplete band gap in the 3D Brillouin zone of our chiral woodpile PhC, in the projected band structure

there are states from other bands which are now degenerate with the Weyl point in frequency and with the same k_x and k_y, and one may expect that these overlapping states would obscure the signature of the Weyl point in the reflection spectrum. However, the agreement we observe between the 3D band structure calculations (Fig. 2.1 (b) and dashed lines in Fig. 2.4) and the reflection spectrum (Fig. 2.4) suggests that this measurement is relatively insensitive to these overlapping states. To further explore this feature in our results, we calculate the modal overlaps between s- and p-polarized plane waves and the Bloch modes of the PhC. Two parameters are defined using these modal overlaps which measure the polarization of the Bloch modes and the overall in-coupling of an arbitrarily polarized plane wave [39–42]. These parameters indicate that the modes with $k_z \neq 0$ in the projected band structure, that would have otherwise obscured the observation of the Weyl point, either have a polarization mismatch with the incident light and/or have inefficient mode in-coupling. This leads to the observed features in the reflection spectrum wherein the boundaries of highly reflecting regions correspond to the $k_z = 0$ Weyl bands, which we now explore in detail.

To understand the relationship between the observed spectral features and the bulk bands, we calculate coefficients that measure the polarization of Bloch modes. For this, we consider plane waves with s- and p- polarizations incident along the $\mathbf{\Gamma} - \mathbf{X}$ direction on the PhC-air interface and define the polarization coupling coefficients C_s and C_p and mode coupling index κ [39–42]

$$\kappa = \eta_{s,\mathbf{k},n} + \eta_{p,\mathbf{k},n}; \quad C_{s/p} = \frac{\eta_{s/p,\mathbf{k},n}}{\kappa} \tag{2.1}$$

$$\eta_{p,\mathbf{k},n} = \frac{\left|\iiint \hat{\mathbf{y}} \cdot \mathbf{H}_{\mathbf{k},n}(x,y,z)\mathrm{d}x\mathrm{d}y\mathrm{d}z\right|^2}{V \iiint \left|\mathbf{H}_{\mathbf{k},n}(x,y,z)\right|^2 \mathrm{d}x\mathrm{d}y\mathrm{d}z} \tag{2.2}$$

$$\eta_{s,\mathbf{k},n} = \frac{\left|\iiint (\cos\theta\hat{\mathbf{x}} - \sin\theta\hat{\mathbf{z}}) \cdot \mathbf{H}_{\mathbf{k},n}(x,y,z)\mathrm{d}x\mathrm{d}y\mathrm{d}z\right|^2}{V \iiint \left|\mathbf{H}_{\mathbf{k},n}(x,y,z)\right|^2 \mathrm{d}x\mathrm{d}y\mathrm{d}z} \tag{2.3}$$

where $\mathbf{H}_{\mathbf{k},n}(x,y,z)$ is the magnetic field eigenmode of the PhC with momentum $\mathbf{k}$ and band index n, θ is the angle of incidence along $\mathbf{\Gamma} - \mathbf{X}$ and all integrals are calculated over a unit cell with volume V. κ goes from 0 to 1 and measures the strength of coupling to a plane wave of any arbitrary polarization while C_s and C_p measure the overlap between s- and p-polarized plane waves and the Bloch modes. Large reflection for a certain range of angles and frequencies in the absence of band gaps can then be thought of as either a polarization mismatch between the incident wave and the Bloch mode, indicated by small $C_{s/p}$, and/or inefficient mode in-coupling, indicated by small κ.

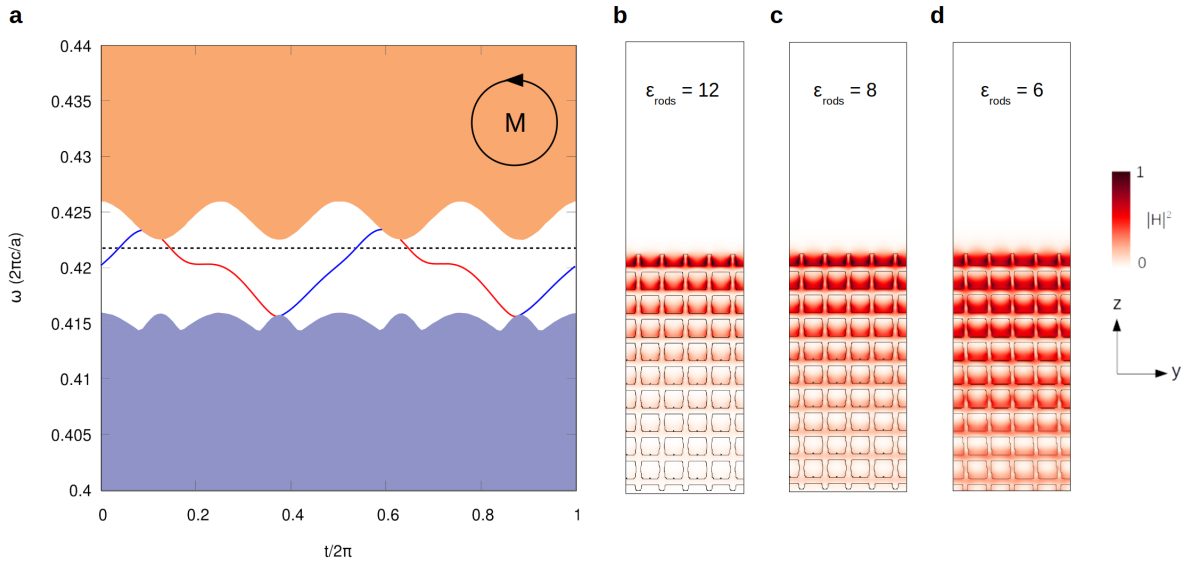

Figure 2.7. (a) The k_z-projected band structure for the truncated chiral woodpile PhC ($\varepsilon_{\text{rods}} = 12$, rod width = 0.175a, rod height = 0.25a) along a loop enclosing the **M** point with radius 0.15 $(2\pi/a)$ and parametric angle $0 \leq t/2\pi \leq 1$. Solid colors are projections of bulk bands, the solid red and blue lines are surface states localized to the top and bottom surfaces respectively and the black dotted line marks the frequency of the Weyl point. (b)-(c) Magnetic field intensity of the surface state at $t/2\pi = 0.25$ for $\varepsilon_{\text{rods}} = 12$ and 8 respectively. (d) Magnetic field intensity of the surface resonance for $\varepsilon_{\text{rods}} = 6$ calculated using FDTD method as implemented in MEEP [1].

In Fig. 2.6, we analyze a slice of the reflection spectrum that corresponds to Bloch modes with momenta $\mathbf{k} = (0.1, 0, k_z)$ $(2\pi/a)$. As previously stated, the band structure weighted by the coupling coefficients shows that there are wavelength ranges where the states are nearly completely s- or p- polarized and/or have small mode coupling index. We particularly point out the wavelength ranges $\sim 4.65 - 4.8$ μm in Fig. 2.6 (b) and $\sim 5.0 - 5.15$ μm in Fig. 2.6 (d) (highlighted in blue) which coincide with the sharp increases in reflection. Moreover, the boundary separating the reflecting and transmissive region coincides with band 4 at $k_z = 0$ in s-polarization and band 5 at $k_z = 0$ in p-polarization plots, which are the Weyl bulk bands of interest. Thus the signatures of both bands and the Weyl point are present in simulations and measurements done with 45° polarization.

2.2.5 Bulk-boundary correspondence and surface states

The topological charge associated with Weyl points gives rise to Fermi arc-like surface states which are a direct consequence of the bulk-boundary correspondence. However, at

low dielectric contrast, as in the present experiment, the overlapping states and the lack of a bandgap imply that any surface states associated with the Weyl points are leaky resonances that are degenerate with bulk eigenstates of the PhC. Even at high dielectric contrast, the surfaces states associated with the Weyl point at $\mathbf{\Gamma}$ are resonances for two reasons: (1) When the structure is truncated, surface states lie above the light line of air and confinement on this side requires a trivial bandgap material and (2) the dispersion of the bands for our structure does not allow the opening of a local bandgap around the Weyl point. We have found that such resonances (if present) are too broadened by leakage to be observable for the index contrast of the photonic crystal used here. However, both these issues are resolved when examining a high-contrast version of our PhC, in the vicinity of the charge -2 Weyl point at $\mathbf{R}$ $[k_x = k_y = k_z = 0.5\ (2\pi/a)]$, which we consider for the following numerical analysis.

In a chiral woodpile PhC with $\varepsilon_{\text{rods}} = 12$ and truncated in the z-direction, we examine the surface band structure along a circular loop enclosing the projection of the Weyl point (at $\mathbf{M}$) [32, 43]. This loop has radius $0.15\ (2\pi/a)$ and is parametrized by an angle $0 \leq t/2\pi \leq 1$. The surface band structure as plotted in Fig. 2.7 (a) reveals the existence of Fermi arc surface states in the non-trivial gap formed along the loop. Due to the bulk-boundary correspondence, the number of these surface states that cross the bulk band gap is equal to the Chern number of the enclosed degeneracy, which in this case is -2. The sign corresponds to the direction of motion of the surface states. The magnetic field intensity of the surface state localized to the top edge is plotted in Fig. 2.7 (b), which shows strong confinement to the PhC-air interface. We repeat these calculations for progressively smaller values of dielectric contrast and find that a local gap fails to open at $\varepsilon_{\text{rods}} \sim 6$ around the loop considered here and at $\varepsilon_{\text{rods}} \sim 5$, a local gap fails to open for a loop of any radius. Examining the field intensity profile from a finite-difference time-domain (FDTD) simulation [1], shown in Fig. 2.7 (d), reveals that at $\varepsilon_{\text{rods}} = 6$, the surface state is now a leaky resonance with a Q-factor $\sim 10^3$. As we can see, the confinement of the surface state relies on the existence of at least a local bandgap, which heavily depends on the dielectric contrast. For the dielectric contrast of our experiment, namely $\varepsilon_{\text{rods}} = 2.31$, the resonances have broadened sufficiently to be effectively unobservable. On the other hand, changing the dielectric contrast does not break the screw symmetry in our structure and as such does not affect the existence of the Weyl points, whether at the $\mathbf{\Gamma}$ or $\mathbf{R}$-points. Therefore, although the surface states in our low-contrast PhC have turned into resonances that extend into the bulk, the charge ± 2 Weyl points have a continued existence due to their symmetry protection.

2.3 Conclusion

To summarize, in this chapter, we have presented the observation of a charge +2 Weyl point in a 3D PhC in the mid-infrared regime. The fact that we have used a relatively low refractive index polymer opens the door to exploring 3D topological phenomena in the IR and into optical frequencies, where very high-index, low-loss materials may not be available or amenable to 3D device fabrication. It will be of interest in the future to explore surface resonances in 3D PhCs with Weyl points; these will have fundamentally different properties compared to traditional surface states because of radiative loss, which will give rise to non-Hermitian effects on the surface.

Chapter 3
Charge-2 Weyl point splitting in chiral woodpile photonic crystals

In this chapter, we theoretically and experimentally explore the splitting of the charge-2 Weyl point discussed in the previous chapter, into two charge-1 Weyl points. Using a theoretical analysis rooted in symmetry arguments, we show that this splitting occurs along high-symmetry directions in the Brillouin zone. This chapter is based on work that was done in collaboration with Christina Jörg, Jiho Noh, Alexander Cerjan, Shyam Augustine, Georg von Freymann and Mikael C. Rechtsman [44].

3.1 Overview

As discussed in the previous chapter, a Weyl point (WP) is a topological degeneracy that can possess an arbitrary integer charge, m, and can be described by the generic three-dimensional Hamiltonian of the form [45],

$$\mathcal{H}(\mathbf{k}) = k_+^{|m|}\sigma_+ + k_-^{|m|}\sigma_- + k_z\sigma_z + \omega_0 I \tag{3.1}$$

where $k_\pm = (k_x \pm ik_y)$, $\sigma_\pm = 1/2(\sigma_x \pm i\sigma_y)$, $\sigma_{x,y,z}$ are the Pauli matrices, I is the identity matrix, and ω_0 is the frequency at which the WP occurs in the spectrum. The eigenvalues of $\mathcal{H}(\mathbf{k})$ describe the two bands in the vicinity of the WP and are given by

$$\lambda_\pm = \omega_0 \pm \sqrt{(k_x^2 + k_y^2)^{|m|} + k_z^2}. \tag{3.2}$$

From equation (3.2) it is evident that the leading order $k_{x,y}$-dependence in the dispersion around a WP is governed by its charge and henceforth in this chapter, charge-1 WPs

will be referred to as "linear" and charge-2 WPs as "quadratic".

While charge-1 WPs have been extensively studied in various systems, higher-charged WPs have received relatively less attention. As explored in the previous chapter, higher-charged WPs can occur in non-symmorphic crystals, such as the chiral woodpile structure, due to the stabilization of multiple linear WPs at high symmetry points in momentum space [46–48]. Such structures exhibit several additional symmetries and therefore provide an ideal platform for tuning the locations of linear WPs that can form from splitting a quadratic WP due to symmetry breaking [48, 49]. This tunability of WPs could be of importance in the realization of three-dimensional large-volume, single-mode lasing devices that rely on the vanishing photonic density of states at frequency-isolated linear WPs [50].

In this chapter, we experimentally demonstrate that under careful symmetry breaking, quadratic WPs can be split into two linear WPs of the same charge. We show by analyzing the underlying symmetries of the structures that for certain choices of defects this splitting occurs strictly along high symmetry directions in momentum space. We also show that the momentum-space separation of the resulting linear WPs can be readily controlled via geometric parameters of the structure. While WPs have mostly been observed in large-scale structures with mm- or cm-scale lattice constants [51–53], our platform of choice is a micron-scale three-dimensional photonic crystal (PhC), similar to the one employed in the previous chapter, fabricated by a two-photon polymerization process [54, 55]. This allows for the realization of WPs at near-infrared wavelengths that we characterize using Fourier transform infrared (FTIR) spectroscopy.

3.2 Results

3.2.1 Simulations and symmetry analysis

The particular structure that we employ to realize this phenomenon is again a chiral woodpile PhC whose unit cell consists of stacked and partially overlapping layers of rods that have a relative 45° in-plane rotation between them as shown in Fig. 3.1 (a). The lattice constant in all three directions is $a = 2.1\,\mu\text{m}$. The four rods in the unit cell have height h and widths w_0, w_{45}, w_{90}, w_{135} where the subscripts identify the rods by their angle of orientation with respect to the x-axis. The rods are made out of a nearly lossless, non-magnetic dielectric material of dielectric constant $\varepsilon = 2.31$. Due to the chirality of this structure, inversion symmetry is broken which allows WPs to exist. Furthermore,

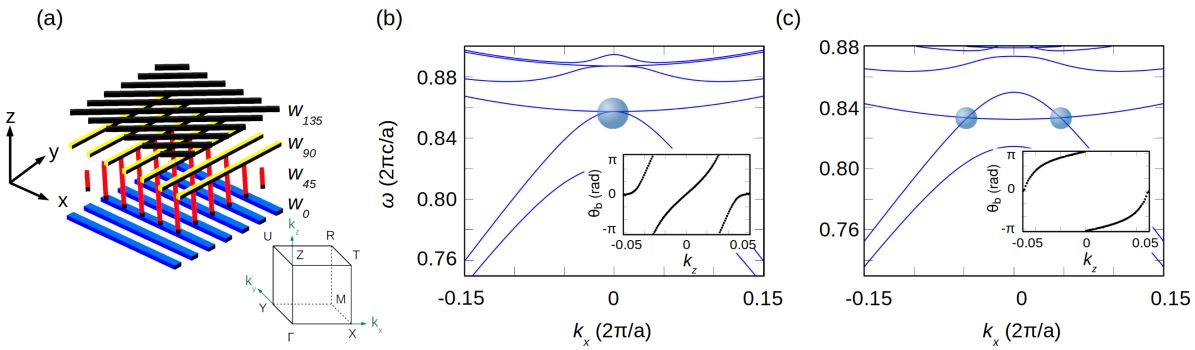

Figure 3.1. (a) An exploded view of the chiral woodpile PhC (one unit cell in z) and its Brillouin zone. (b) Band structure of the chiral woodpile PhC, made out of dielectric rods ($\varepsilon = 2.31$), with equal widths for all rods at $k_y = k_z = 0$ showing bands 3 to 8. The quadratic WP at $\mathbf{\Gamma}$ is marked with a blue circle. The inset shows a plot of the Berry phase for band 4 around $\mathbf{\Gamma}$. The double winding indicates that the degeneracy has a charge of 2. (c) The band structure of the same chiral woodpile PhC in (b) but with increased rod width w_0 in the blue layer of each unit cell. The linear WPs that occur due to the splitting of the quadratic WP in (b) are marked with blue circles. The inset shows a plot of the Berry phase for band 4 around one of the degeneracies. The single winding indicates that the degeneracy has a charge of 1.

when all rod widths and heights are equal, this structure belongs to the non-symmorphic space group $P4_222$ (# 93), which has a screw axis along the z direction. This screw symmetry, defined by a 90° rotation in the x-y plane and $a/2$ shift along the z direction, results in the presence of a quadratic WP at the Brillouin zone center ($\mathbf{\Gamma}$), as shown in Fig. 3.1 (b) and corner ($\mathbf{R}$).

Instead, when the rod width in one layer in the unit cell is taken to be different from the widths of the other three layers, the screw symmetry is broken, resulting in a splitting of the quadratic WP into two linear WPs as shown in Fig. 3.1 (c). For example, when a width defect is introduced such that $w_{45} = w_{90} = w_{135} = w$ and $w_0 \neq w$, the space group of the structure is reduced to $P222$ (# 16). While this subgroup does not contain the screw symmetry, it retains C_2 rotations about the x, y and z axes that restrict the splitting directions of the WPs to high symmetry lines in momentum space. This can be argued as follows: Let the splitting associated with this change in space group by a small perturbation result in two linear WPs, one of which is located at a generic momentum point (k_x, k_y, k_z). The location of both WPs can be inferred from the symmetry operations of the space group $P222$ and time reversal symmetry as they must either map to themselves or to each other under these operations. Time reversal symmetry requires a WP to be located at ($-k_x$, $-k_y$, $-k_z$). However, the aforementioned C_2 rotations require a WP to be located at ($-k_x$, k_y, $-k_z$), (k_x, $-k_y$, $-k_z$)

and $(-k_x, -k_y, k_z)$. Since there are only two linear WPs that can occur from the splitting of a single quadratic WP, at least two components of these momentum vectors must be set to 0 or π/a such that they map to themselves under a sign flip. As a result, for the quadratic WP at $\mathbf{\Gamma}$, the symmetry-consistent directions of splitting are $\mathbf{\Gamma} - \mathbf{X}$, $\mathbf{\Gamma} - \mathbf{Y}$ or $\mathbf{\Gamma} - \mathbf{Z}$, and for the quadratic WP at $\mathbf{R}$, the symmetry-consistent directions of splitting are $\mathbf{R} - \mathbf{U}$, $\mathbf{R} - \mathbf{T}$ or $\mathbf{R} - \mathbf{M}$. A similar analysis shows that the splitting can be made to occur along diagonal directions in momentum space (e.g. along $\mathbf{\Gamma} - \mathbf{M}$ for the WP at $\mathbf{\Gamma}$) when w_{45} or w_{135} is chosen to be different from the other three rod widths. In the most general case where all four rod widths are different, the space group is further reduced to $P2$ (#3) which retains C_2 rotation about the z axis. This still restricts the splitting to occur in the $k_z = 0$ plane or along $\mathbf{\Gamma} - \mathbf{Z}$ for the quadratic WP at $\mathbf{\Gamma}$ and $k_z = \pi/a$ plane or along $\mathbf{R} - \mathbf{M}$ for the quadratic WP at $\mathbf{R}$. For the remainder of this article, we will focus on the case where a width defect is introduced in a single layer in each unit cell such that $w_{45} = w_{90} = w_{135} = w$ and $w_0 \neq w$.

To demonstrate the topological nature of WPs in the split and unsplit cases, we directly calculate their topological charges from the electromagnetic eigenmodes extracted from MIT Photonic Bands (MPB) [56]. Since WPs act as sources or sinks of Berry curvature, their charge can be obtained by integrating the Berry curvature over a closed sphere enclosing the WP in momentum space. Alternatively, this can also be calculated using a series of line integrals of Berry connection on closed contours that are sampled from such a sphere. These line integrals represent the geometric phase, called the Berry phase (θ_B), acquired by the eigenmodes as they are adiabatically transported around the closed contours. These contours can be chosen to lie parallel to the k_x-k_y plane and θ_B can therefore be plotted as a function of k_z. The topological charge of the WP is the winding number of $\theta_B(k_z)$. The plots for θ_B for the split and unsplit cases are shown in the insets of Fig. 3.1 (b)-(c) which confirm that the degeneracy at $\mathbf{\Gamma}$ is a quadratic WP of charge +2 and the split degeneracies along the $\mathbf{\Gamma} - \mathbf{X}$ direction are linear WPs of charge +1 each.

3.2.2 Fabrication process

For the fabrication of the chiral photonic woodpile samples in the IP-Dip resist, we use a Nanoscribe Professional GT at a scan speed of 20 mm/s and laser power of 62%, which corresponds to 34 mW on the entrance lens of the objective. The structures are printed onto Menzel cover slips (borosilicate glass). Since we use the dip-in configuration of the Nanoscribe the cover slips need to be coated with approximately 13 nm of Al_2O_3

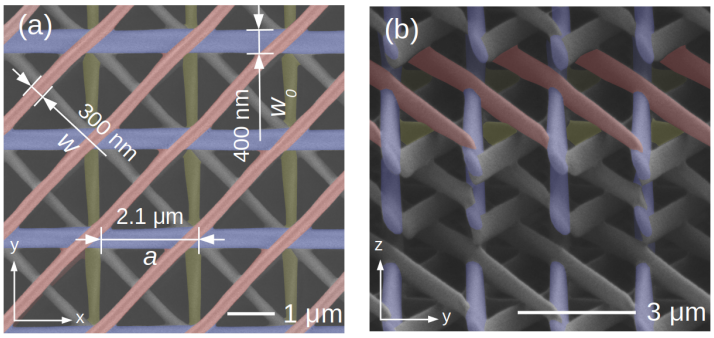

Figure 3.2. False color SEM image of a typical chiral woodpile photonic crystal with increased rod width w_0 in the blue rods. (a) Top view, (b) side view.

in order to facilitate interface finding. The coated cover slips show a transmission of greater than 75% for all wavelengths used in our measurements. After printing, the sample is developed for 10 min in PGMEA and 10 min in isopropanol, subsequently. It is then transferred to a solution of 150 mg Irgacure 651 in 24 ml of isopropanol and illuminated for 60s with UV light from an Omnicure S2000 with 95% iris opening. This post-print UV curing [57] increases the stability of the woodpile structure. In the end, the sample is blow-dried in a stream of nitrogen. The complete footprint of the structure is approximately 1 mm^2 with 20 layers in height. To achieve such a large footprint within reasonable writing time we use elaborate stitching: The structure is printed in portions of 4×4 angled blocks between which the stage is moved for larger travel distance. Inside each block and layer we print the sample using the galvanometer-scanning in combination with piezo-stitching for reduced vignetting and more precise positioning. The alignment of the stage, piezo and galvo axes is ensured by employing the axis transformation implemented in NanoWrite. While the usual rods consist of just one printed line, the defect rod width is increased by printing multiple lines at a hatching distance between 10 nm and 50 nm. We print several samples of this PhC with a lattice constant of 2.1 µm with varying values of w_0, while fixing w to 0.2 µm for the symmetry broken samples. Due to the voxel's height in z, adjacent layers overlap by approximately 50% of the rod height. A scanning electron microscope (SEM) image of a typical sample is shown in Fig. 3.2.

3.2.3 Experimental measurements

For characterizing the fabricated PhC, we measure the angle-resolved transmittance via Fourier-transform infrared spectroscopy (FTIR). This measurement is performed using

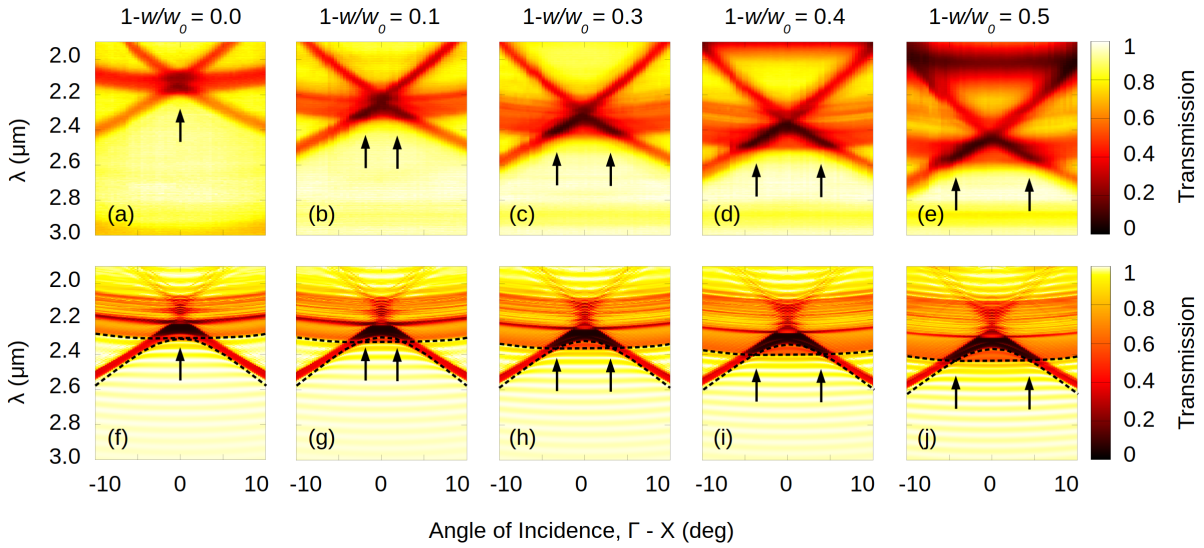

Figure 3.3. (a)-(e) Measured angle-resolved FTIR spectra of the chiral woodpile PhC with varying values of the width w_0. The locations of the WPs are marked with arrows. (f)-(j) The corresponding RCWA simulated spectra of the chiral woodpile PhC. The dashed black lines are the $k_z = 0$ bulk bands calculated from MPB.

the Hyperion 3000 microscope attached to a Bruker Vertex v70 FTIR. The spectra are taken in transmission mode with a halogen lamp and a Mercury-Cadmium-Telluride (MCT) detector cooled by liquid nitrogen. To increase k-space resolution, the lower 15× Cassegrain objective is covered except for a pinhole of 1 mm in diameter, such that we obtain a nearly collimated beam. We estimate the spread of this beam to be approximately ±0.3° in the direction along which we measure (the k_x direction in Fig. 3.3), and approximately ±2° perpendicular to that [58]. The sample is then tilted with respect to the beam along its x-axis, around the direction of perpendicular incidence of the beam. This is done by tilting the sample holder in steps of approximately 0.4°. As we cannot determine the position of perfect perpendicular incidence from the sample positioning (within an error of approximately 5°), we take spectra for both positive and negative tilting angles, and determine Γ from the symmetry of the measured angle resolved transmittance spectra. All spectra are referenced to the transmission of the used substrates, and individually scaled to their maximum at each angle. For each angle we average over 64 measurements with an FTIR resolution set to 4 cm^{-1} in wavelength. The small dip in transmittance around 2.8 µm wavelength is constant across angles and is due to the absorption in the IP-Dip [59]. The spectra are post-processed to remove fringes due to multiple reflections in the glass and Al_2O_3.

For the case of all equal rod widths, we observe a quadratic WP at 2.2 µm wavelength

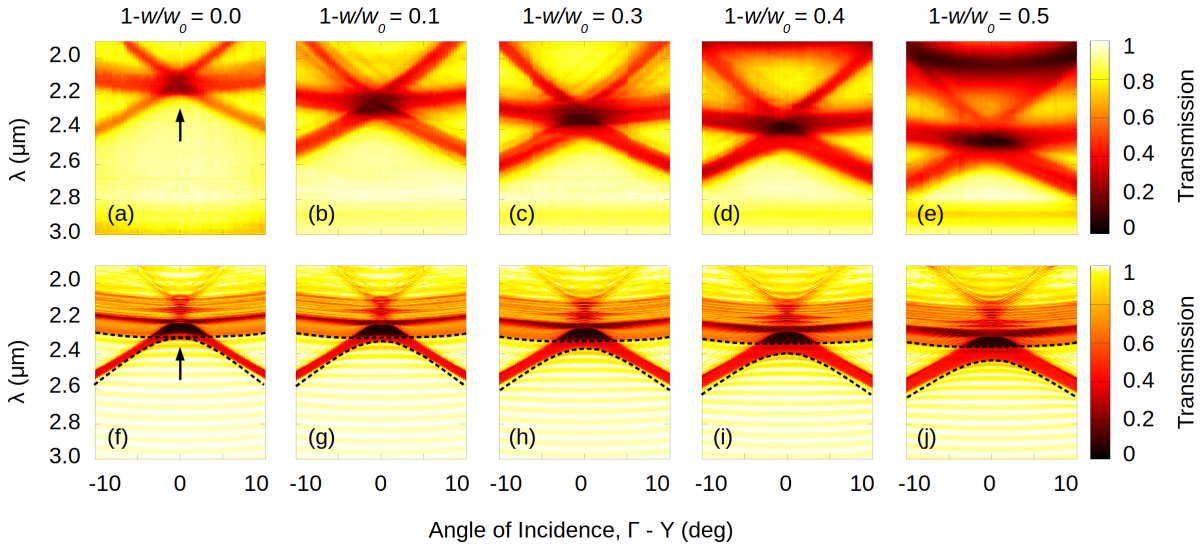

Figure 3.4. Spectra along $\mathbf{\Gamma} - \mathbf{Y}$: (a)-(e) Measured angle-resolved FTIR spectra of the chiral woodpile PhC with varying values of the width w_0. (f)-(j) The corresponding RCWA simulated spectra of the chiral woodpile PhC. The dashed black lines are bulk bands calculated from MPB. We see that the two bands that form the quadratic WP for $w = w_0$ move apart on increasing rod width w_0.

at the $\mathbf{\Gamma}$ point (Fig. 3.3 (a)). As previously described, an increase in w_0 splits the WP along the $\mathbf{\Gamma} - \mathbf{X}$ direction into two linear WPs. This splitting can be seen as a spectral feature corresponding to the two involved bands piercing through each other with the linear WPs occurring at their intersection points as shown in Fig. 3.3 (b)-(e). Furthermore, the angular separation between the two linear WPs increases with w_0. In addition to the spectra taken along the $\mathbf{\Gamma} - \mathbf{X}$ direction, we also performed measurements and simulations along $\mathbf{\Gamma} - \mathbf{Y}$, which are shown in Fig. 3.4. We see here that the two bands, which form the quadratic WP for equal rod widths in all layers, move apart upon increasing w_0 and are no longer degenerate. This is as expected since the linear WPs are point degeneracies that only occur along the $\mathbf{\Gamma} - \mathbf{X}$ direction.

To compare our experimental results with theory, we also perform RCWA (rigorous coupled-wave analysis) simulations as implemented in Stanford Stratified Structure Solver (S^4) [38], to obtain the transmission spectrum of this PhC. The simulated spectra are plotted in Fig. 3.3 (f)-(j) and Fig. 3.4 (f)-(j) and show an excellent agreement with the experimentally obtained data. Moreover, the sharp spectral features match the $k_z = 0$ Weyl bands obtained from MPB (dashed lines in Fig. 3.3 (f)-(j) and Fig. 3.4) allowing for a direct observation of the splitting.

We extract the angular separation θ between the two linear WPs from the experimental

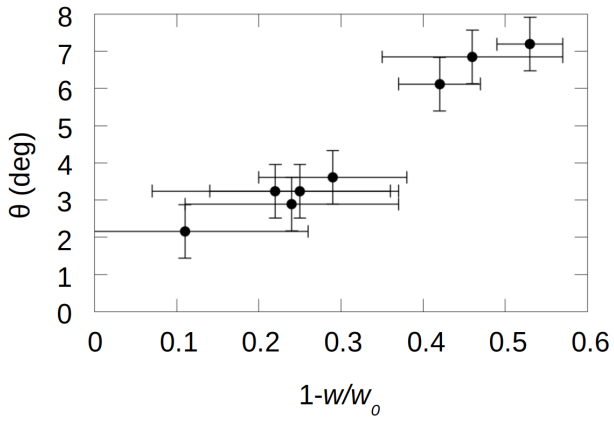

Figure 3.5. The angular separation of WPs, θ, as a function of the symmetry-breaking parameter, $1 - w/w_0$. All data points correspond to samples that were fabricated with the same value of w.

data and plot it as a function of the symmetry-breaking parameter $1 - w/w_0$ in Fig. 3.5, demonstrating the tunable nature of WP splitting in our experiments.

3.2.4 Accidental Charge-2 Weyl points

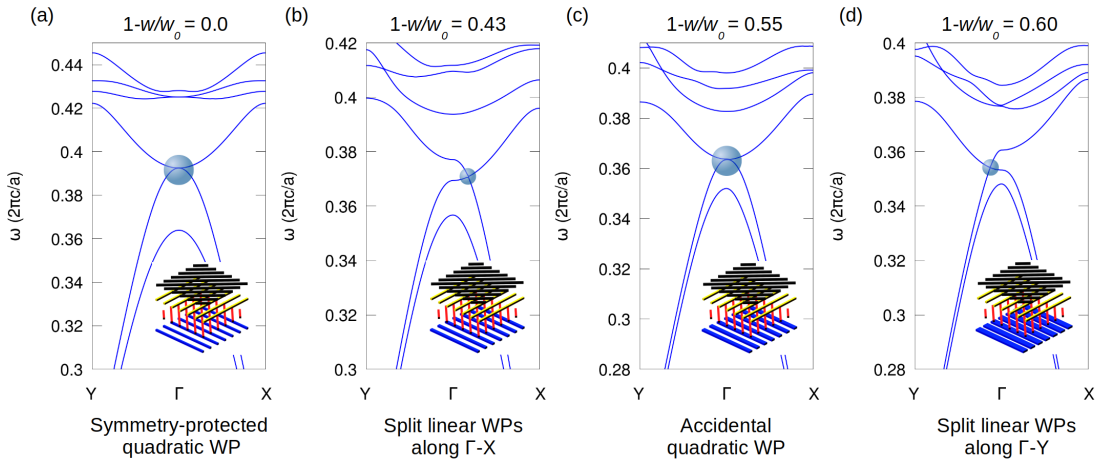

Figure 3.6. (a) Symmetry-protected quadratic WP for $w_0 = w$. (b) This quadratic WP first splits into two linear WPs along $\mathbf{\Gamma} - \mathbf{X}$ upon increasing w_0. (c) Further increasing w_0 re-merges the two linear WPs, leading to the formation of an accidental quadratic WP. (d) Increasing w_0 beyond the re-merging point leads to a splitting of this quadratic WP along $\mathbf{\Gamma} - \mathbf{Y}$.

In our PhCs, the separation of WPs in momentum space is found to be a monotonic function of the symmetry-breaking parameter, however we point out here that this is not true in general. For higher dielectric contrast, the separation of the WPs can first increase

and then decrease to zero for increasing values of the symmetry-breaking parameter. This can lead to the formation of accidental quadratic WPs which are not symmetry protected but are obtained on the fine tuning of parameters. We present an example of an accidental quadratic WP which is formed due to the re-merging of the split linear WPs on increasing the symmetry-breaking parameter. The band structure for a chiral woodpile made out of Si rods ($\varepsilon = 12$) is shown in Fig. 3.6. For $w_0 = w$ we have the quadratic WP, protected by screw symmetry (Fig. 3.6 (a)). As with the low-contrast PhC in the experiment, upon increasing w_0, this quadratic WP splits into two linear WPs, whose separation first increases along the $\mathbf{\Gamma} - \mathbf{X}$ direction (Fig. 3.6 (b)). However, on increasing w_0 further, their separation decreases to zero (Fig. 3.6 (c)), leading to the formation of an accidental quadratic WP. Increasing w_0 beyond this re-merging point leads to a splitting of this quadratic WP along a different symmetry-allowed direction, $\mathbf{\Gamma} - \mathbf{Y}$ in this case (Fig. 3.6 (d)).

3.2.5 Interface states associated with Weyl points

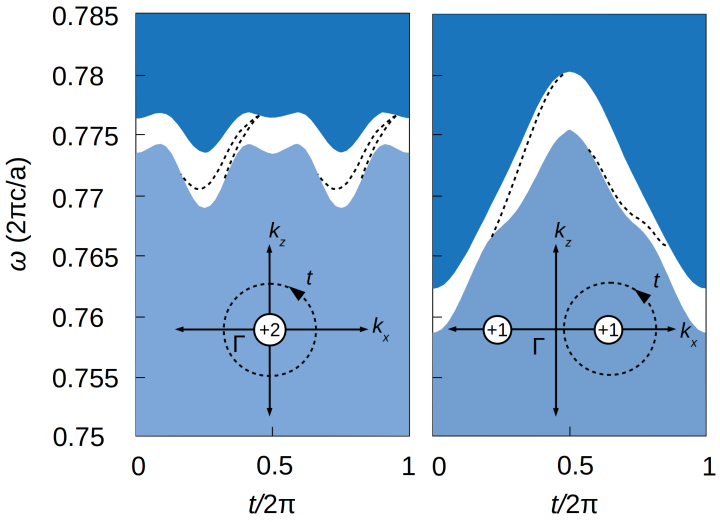

Figure 3.7. Surface states associated with the WPs at the interface between two low-contrast chiral woodpile PhCs with opposite chirality. (a) The k_y-projected band structure along the circular loop, parameterized by t, enclosing the quadratic WP at $\mathbf{\Gamma}$. The non-trivial gap formed along the loop contains two pairs of hybridized surface states (dashed lines) with even and odd symmetry with respect to the mirror plane at the interface. The blue solid colors are projections of the bulk bands. (b) The k_y-projected band structure along the circular loop enclosing one of the split linear WPs, showing only a single pair of even and odd surface states.

Perhaps the most direct physical manifestation of the non-trivial topology of a WP is the presence of surface states that form Fermi arcs connecting WPs of opposite charges.

In the previous chapter, we explored the surface states due to the Weyl point whose momentum was below the light line of air. As a result, the surface states were confined to the surface due to index guiding.

We now present a numerical exploration of the surface states associated with both the quadratic and linear WPs in our structure that lie above the light line of air. Due to their momentum being close to the Brillouin zone center, the surface states are leaky resonances that radiate away from the surface with a finite lifetime. At low dielectric contrast such as in our experiment, the lifetime of such resonances can be so low that they are effectively unobservable in experiment and hard to extract and analyze numerically. To overcome this difficulty, we consider an interface between two chiral woodpile PhCs with opposite handedness for our analysis. This leads to a doubling of the number of surface states due to the presence of WPs on both sides of the interface. Moreover, the surface states originating from both structures are degenerate in frequency and momentum and can therefore hybridize to form states with even and odd symmetry with respect to the mirror plane at the interface. Nevertheless, the topological origin of these surface states can be directly confirmed by examining the surface spectrum along a circular contour that encloses the projection of the WPs.

We consider a system consisting of two chiral woodpile PhCs with opposite chirality and equal rod widths in all layers that meet at an interface parallel to the $y = 0$ plane. The surface band structure calculated along a circular loop in the k_x-k_z plane enclosing the quadratic WP at $\mathbf{\Gamma}$ is shown in Fig. 3.7 (a). This loop has a radius of 0.05 $(2\pi/a)$ and is parametrized by a single angular variable $0 \leq t/(2\pi) < 1$. The surface band structure reveals the existence of two pairs of hybridized states that cross the non-trivial gap formed along the loop. Due to the bulk-boundary correspondence principle, the number of surface states implies that the magnitude of charge of the enclosed WPs is 2. Next, we consider the same simulation but for an increased rod width w_0 that splits the quadratic WP. The surface band structure along a loop of radius 0.033 $(2\pi/a)$ enclosing just one of the linear WPs is shown in Fig. 3.7 (b) which reveals only one pair of surface states in the gap formed along the loop. This indicates that the charge of the enclosed WP has magnitude of 1.

3.3 Conclusion

In conclusion, we have observed the splitting of a quadratic Weyl point into two linear Weyl points in a low-contrast 3D PhC. We find that the splitting can be made to occur

strictly along high-symmetry directions in momentum space, a consequence of controlled symmetry breaking and that their separation can be readily tuned via the geometric parameters of the crystal. The micron-scale periodicity of our structure allows us to access Weyl points in the near-infrared optical spectrum. Our approach opens new avenues for designing large-volume single-mode lasers [50], using Weyl points and exploring Fermi arc surface states in microscale photonic structures, relevant to near-infrared optics.

Chapter 4
Topological phases of photonic crystals under crystal symmetries

In this chapter, we focus our attention on topological one- and two-dimensional photonic crystals (PhCs). Such PhCs have recently emerged as a popular platform for realizing various types of topological phases due to their flexibility, ease of fabrication, and potential for device applications. Here, we develop a complete classification of topological bands in one- and two-dimensional photonic crystals with and without time-reversal symmetry. Our approach relies only on the symmetry representations of the field eigenmodes at high-symmetry points in momentum space and therefore this approach can be used to efficiently guide the design of a wide range of topological PhCs. In particular, we show that the classification provided here is useful for diagnosing photonic crystal analogs of obstructed atomic limits, fragile phases, and stable topological bands that include Dirac semi-metals and Chern insulators. This chapter is based on work that was done in collaboration with Ali Ghorashi, Thomas Christensen, Mikael C. Rechtsman and Wladimir A. Benalcazar.

4.1 Overview

As we discussed in Chapter 1, Photonic crystals (PhCs) are periodically patterned dielectric media that can be described by a Maxwell eigenvalue problem [3, 4]. The periodicity of the dielectric medium acts analogously to a potential for electromagnetic waves and the solutions take the form of Bloch functions that are distributed into photonic bands. Similar to electronic states in conventional solids, PhC eigenmodes can be characterized by topological indices that are global properties across momentum space [60–62]. One of the physical manifestations of these topological indices is the

existence of states that reside on the boundaries of the system, which are protected by the bulk-boundary correspondence of these phases.

A wide variety of topological phases have been realized using PhC-based platforms (as distinct from waveguide-arrays [63] or coupled-resonator [64] based realizations). In one and two dimensions, this includes analogs of the SSH model with quantized polarization [65–67], Chern insulators [68–72], quantum spin-Hall phases [73–77], Dirac semi-metals [78–84], valley-Hall phases [85–87], bulk-obstructed higher-order topological insulators (HOTIs) [88–93], including quadrupolar HOTIs [94–96], and fragile phases [97]. Several of these have also been proposed for photonic device applications such as for lasing [67, 98–100], harmonic generation [101, 102] and light transport [103]. Moreover, the flexibility of the PhC-based platform has made it possible to explore the effects of non-linearity [104, 105] and non-Hermiticity [106, 107] alongside topology – novel physics that is difficult to realize in conventional solids.

Topological systems have been classified in the tenfold way [108, 109] by the presence or absence of the three fundamental symmetries: time-reversal, chiral and particle-hole symmetries. PhCs generally do not possess chiral and particle-hole symmetries and therefore belong in either class A (TR-broken) or class AI (TR-symmetric) of the tenfold way. However, the presence of crystalline symmetries enriches this classification and can help identify finer topological phases within these classes.

There are three kinds of topological bands: (i) Obstructed "atomic limit" (OAL) bands [110], that admit exponentially-localized Wannier functions [111] (such bands are referred to as "Wannierizable") (ii) fragile bands [112, 113] that are non-Wannierizable but become Wannierizable when combined with other atomic limit bands and (iii) stable topological bands that are not Wannierizable. These bands are generally identified by computing Berry phases (or more generally, Wilson loops) over the entire Brillouin zone. In the presence of crystalline symmetries, it is possible to identify and distinguish a subset of them by constructing symmetry-indicator invariants [114–116]. Compared to Berry phases, this symmetry-based approach can be substantially less intensive for computation since it only requires looking at the eigenmodes at high-symmetry points of the Brillouin zone (BZ).

In this chapter, we build on previous works in electronic systems [114, 116] and comprehensively develop a complete classification for topological bands in one- and two-dimensional PhCs under crystalline symmetries with and without time-reversal (TR) symmetry. For each point-group symmetry setting, we exhaustively calculate the topological indices, defined using symmetry-indicator invariants, for the basis set of

atomic limits that span the space of all possible atomic limit bands via the procedure of induction of band representations [117, 118]. This allows us to establish a bulk-boundary correspondence for OAL bands in PhCs where we show that despite the the absence of a Fermi level, the notion of a filling anomaly remains valid and can be used to infer the topological origin of boundary states directly from their frequency spectrum. Furthermore, this classification also allows us to diagnose topological bands that are not OALs, namely fragile phases and bands with Dirac points and Chern numbers, which is made possible by exploiting the algebraic structure of the classification. Based on this, we propose a strategy to diagnose and design topological PhCs. Finally, we discuss the PhC-based implementations of a few other topological systems that lie outside of this framework but where symmetry plays an important role.

4.2 1D photonic crystals

Maxwell's equations with no sources and for a medium that is linear, isotropic, and lossless are [3, 4]

$$\begin{aligned} \nabla \cdot \mathbf{H}(\mathbf{r},t) &= 0 \\ \nabla \times \mathbf{E}(\mathbf{r},t) + \mu_0 \frac{\partial}{\partial t}\mathbf{H}(\mathbf{r},t) &= 0 \\ \nabla \cdot [\epsilon(\mathbf{r})\mathbf{E}(\mathbf{r},t)] &= 0 \\ \nabla \times \mathbf{H}(\mathbf{r},t) - \epsilon_0 \epsilon(\mathbf{r}) \frac{\partial}{\partial t}\mathbf{E}(\mathbf{r},t) &= 0. \end{aligned} \tag{4.1}$$

Expanding the temporal component of the electric and magnetic fields into harmonics as $\mathbf{H}(\mathbf{r},t) = \mathbf{H}(\mathbf{r})e^{-i\omega t}$, $\mathbf{E}(\mathbf{r},t) = \mathbf{E}(\mathbf{r})e^{-i\omega t}$, these equations reduce to

$$\begin{aligned} \nabla \times \left(\frac{1}{\epsilon(\mathbf{r})} \nabla \times \mathbf{H}(\mathbf{r}) \right) &= \left(\frac{\omega}{c} \right)^2 \mathbf{H}(\mathbf{r}) \\ \nabla \times \nabla \times \mathbf{E}(\mathbf{r}) &= \left(\frac{\omega}{c} \right)^2 \epsilon(\mathbf{r})\mathbf{E}(\mathbf{r}). \end{aligned} \tag{4.2}$$

We can choose to solve only the equation for $\mathbf{H}(\mathbf{r})$ in (4.2) since $\mathbf{E}(\mathbf{r})$ can be found from $\mathbf{H}(\mathbf{r})$ using the last equation in (4.1).

A 1D PhC, shown schematically in Fig. 4.1 (a), is a 3D material characterized by a refractive index that is periodic along one direction (x) and is uniform along the other two directions (y and z). The magnetic field eigenmode can therefore be written as a plane

wave solution in the y, z plane multiplied by an x-dependent vector field, $\mathbf{H} = e^{i\mathbf{k}_\parallel \cdot \boldsymbol{\rho}}\mathbf{h}(x)$, where $\mathbf{k}_\parallel$ is the momentum along the uniform directions and $\boldsymbol{\rho} = y\hat{\mathbf{y}} + z\hat{\mathbf{z}}$. However, we are only concerned with propagation along the periodic direction, which implies that $\mathbf{k}_\parallel = 0$. Moreover, since the fields must be perpendicular to the propagation direction, we can define two orthogonal polarizations where the vector fields lie in the y, z plane. Without loss of generality and assuming isotropy, we can take these polarized fields to be $\mathbf{h_z}(x) = h_z(x)\hat{\mathbf{z}}$ and $\mathbf{h_y}(x) = h_y(x)\hat{\mathbf{y}}$. This leads to the following eigenvalue problem for the scalar fields, $h_{\xi=y,z}(x)$,

$$\hat{\Theta}_1 h_\xi(x) = \left(\frac{\omega}{c}\right)^2 h_\xi(x), \;\; \hat{\Theta}_1 \equiv -\partial_x \left(\frac{1}{\epsilon(x)}\partial_x\right), \tag{4.3}$$

where $\hat{\Theta}_1$ is the 1D Maxwell operator that plays a role analogous to the Hamiltonian in quantum mechanics. By exploiting the periodicity of the dielectric function, the above equation can be solved using Bloch's theorem. Specifically, the ansatz given by $h_{\xi,n,k_x}(x) = e^{ik_x x}u_{\xi,n,k_x}(x)$, can be used to solve (4.3), where $u_{\xi,n,k_x}(x)$ is the periodic part of the field defined over a unit cell. As a result of this, (4.3) can be written as

$$\hat{\Theta}_{1,k_x} u_{\xi,n,k_x}(x) = \left(\frac{\omega_n}{c}\right)^2 u_{\xi,n,k_x}(x), \tag{4.4}$$

where

$$\hat{\Theta}_{1,k_x} \equiv -(\partial_x + ik_x)\left(\frac{1}{\epsilon(x)}(\partial_x + ik_x)\right). \tag{4.5}$$

This yields field solutions distributed across discrete frequency bands labeled by the index n and with their momentum, k_x, restricted to lie within the first BZ, as shown in Fig. 4.1 (b). It is also useful to define the inner product between two fields over a unit cell (UC) as

$$\langle u_{\xi,n_1,k_1} | u_{\xi,n_2,k_2} \rangle = \int_{\mathrm{UC}} u^*_{\xi,n_1,k_1}(x) u_{\xi,n_2,k_2}(x) dx. \tag{4.6}$$

Similar to electrons in conventional solids, the introduction of frequency gaps allows for a topological characterization of isolated individual photonic bands or a group of bands, as discussed in the following section.

4.2.1 Classification due to inversion symmetry

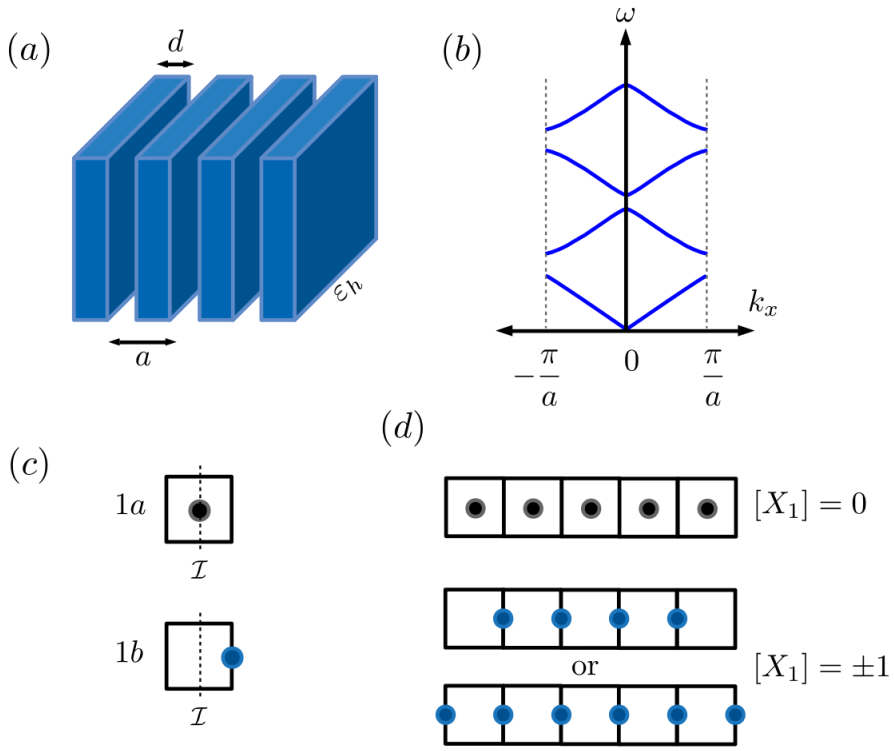

Figure 4.1. (a) Schematic of a 1D PhC made out of alternating layers of dielectric material of dielectric constants ε_h and ε_l with lattice constant a. (b) Schematic of the dispersion of light in a 1D PhC. (c) Wannier centers (solid circles) are located at the two possible maximal Wyckoff positions for inversion-symmetric unit cells (squares). (d) Filling anomaly due to inversion symmetry. The trivial system has a number of states equal to the number of unit cells and is inversion symmetric. The topological system requires at least one more or one fewer state to maintain inversion symmetry.

1D PhCs fall into class A or AI of the tenfold way, depending on whether they break or preserve time-reversal symmetry (TRS), respectively. In either case, 1D PhCs are topologically trivial in the absence of other symmetries. However, additional symmetries enrich the classification. For example, inversion symmetry protects two topological phases in both A or AI. The invariant for a single band in these phases is the Berry phase

$$\theta = \int_{\mathrm{BZ}} \mathcal{A}_{n,k} dk \tag{4.7}$$

where $\mathcal{A}_{n,k} = -\mathrm{i} \langle u_{\xi,n,k} | \partial_k | u_{\xi,n,k} \rangle$ is the Berry connection. Under an inversion-symmetric choice of unit cell, the Berry phase is quantized to 0 or π. This quantization has an intuitive interpretation: in 1D, all photonic bands admit maximally localized Wannier

functions whose centers are gauge invariant quantities [119–125]. Due to inversion symmetry, a single Wannier center (per unit cell) can only be located in two distinct positions in the unit cell, as shown in Fig. 4.1 (c). These positions are called Maximal Wyckoff positions and are labeled by $1a$ and $1b$. The Berry phase in (4.7) of a single non-degenerate band indicates the location of the (one) Wannier center within each unit cell, where $\theta = 0$ and π correspond to the Wannier center being located at the position $1a$ (middle of the unit cell) and $1b$ (edge of the unit cell), respectively.

The calculation of (4.7) involves an integral over the entire BZ, but it can be greatly simplified by looking at the representations of the $\mathbf{H}$ or $\mathbf{E}$ fields at the high-symmetry points (HSPs) of the BZ [126], which are $\mathbf{\Gamma}$ ($k_x = 0$) and $\mathbf{X}$ ($k_x = \pi/a$). Under inversion symmetry $\mathcal{I} : \mathbf{r} \to -\mathbf{r}$, the 1D Maxwell operator obeys

$$\hat{\mathcal{I}}\hat{\Theta}_{1,k_x}\hat{\mathcal{I}}^{-1} = \hat{\Theta}_{1,-k_x}, \tag{4.8}$$

where $\hat{\mathcal{I}}$ is the inversion operator. (4.8) implies that $\hat{\Theta}_{1,k_x}$ commutes with $\hat{\mathcal{I}}$ at $\mathbf{\Gamma}$ and $\mathbf{X}$, i.e., $[\hat{\Theta}_{1,\mathbf{\Gamma}}, \hat{\mathcal{I}}] = [\hat{\Theta}_{1,\mathbf{X}}, \hat{\mathcal{I}}] = 0$, since these HSPs map to themselves under a negative sign, modulo a reciprocal lattice vector. Thus, the eigenmodes at these HSPs can be labeled by the eigenvalues of $\hat{\mathcal{I}}$, which are ± 1 since $\hat{\mathcal{I}}^2 = \mathbb{1}$. To aid with generalization to 2D later, we denote these eigenvalues at the HSP $\mathbf{\Pi}$ as $\mathbf{\Pi}_{1,2} = \pm 1$. We can define the symmetry-indicator invariant for a set of bands as

$$[X_1] \equiv \#\mathbf{X}_1 - \#\mathbf{\Gamma}_1 \quad \in \mathbb{Z}, \tag{4.9}$$

where $\#\mathbf{\Pi}_1$ is the number of states at the HSP $\mathbf{\Pi}$ with $\mathcal{I}$ eigenvalue $+1$. The invariant in (4.9) encodes the value of the Berry phase as [126, 127]

$$\frac{\theta}{2\pi} = \frac{1}{2}[X_1] \mod 1, \tag{4.10}$$

which provides a $\mathbb{Z}_2$ classification of dipole moments in crystalline structures. We note that the Berry phase and the invariant in (4.9) depend on the choice of unit cell.

The bands that originate from localized and symmetric Wannier functions form a representation of the crystal's symmetry group, called a band representation [117]. The values of $[X_1]$ for a single isolated band can be enumerated exhaustively by working out the inverse problem, i.e., given a set of Wannier functions, we can calculate the band representation that such a set leads to. This inverse problem of band topology has been used to classify topological phases in insulators [117, 118].

In the next section, we explore the physical consequence of a non-trivial invariant: the presence of boundary states. However, as we shall explain shortly, the lack of chiral or particle-hole symmetries to pin the boundary states means that they need not lie within bandgaps, and the issue of bulk-boundary correspondence is somewhat more subtle in PhCs.

4.2.2 Filling anomaly, counting mismatch and boundary states

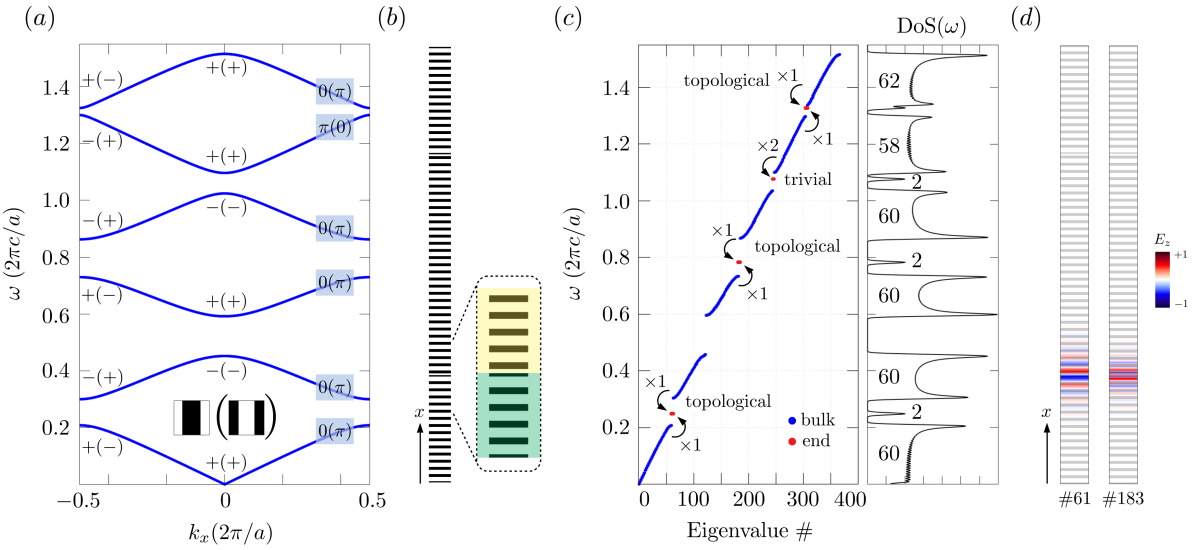

Figure 4.2. (a) The photonic band structure of a 1D PhC with $\varepsilon_h = 6.25$, $\varepsilon_l = 1$ and $d = 0.6a$. The two possible types of inversion-symmetric unit cells are shown in the inset. Eigenvalues of $\mathcal{I}$ at the HSPs for both types of unit cells are labeled with $+/-$ signs. The Berry phases for both types of unit cells are shown in blue boxes. (b) The dielectric profile of a finite system of size 61 unit cells with interfaces between the two types of unit cells. The inset highlights the switch between the unit cell types across the boundary (c) The frequency spectrum for the finite system shown in (b). An odd-integer counting mismatch per band leads to the presence of topological end states in the first and third bandgaps. These end states may also be degenerate with bulk bands, such as in the case of band 6. The photonic DoS is also shown in the same figure. (d) The E_z mode profiles of one of the topological end states in the first and third gaps.

The existence of boundary states ("end" states in 1D) can be heuristically understood by considering the effect of a boundary between two distinct topological phases. Since the invariants are quantized and must change discretely, a gap-closing point at the boundary is required, resulting in boundary states. For 1D systems with inversion symmetry, such boundary states of topological origin are associated with a *filling anomaly* [114, 128, 129], which we describe briefly.

Consider a finite tiling of N inversion-symmetric 1D unit cells which creates two inversion-symmetry-related sectors in real space with two ends as shown in Fig. 4.1 (d). A single isolated band in the bulk gives rise to N states in this finite system. For a trivial bulk band with $[X_1] = 0$, the Wannier centers in the finite tiling must be placed at the $1a$ position of the unit cell, and the number of states that correspond to this bulk band is equal to N. However, for a topological bulk band with $[X_1] = \pm 1$, the Wannier centers in the finite tiling must be placed at the $1b$ position of the unit cell, which leads to a difficulty: N states cannot maintain inversion symmetry due to the position of the Wannier centers. Instead, either $N - 1$ or $N + 1$ (or more generally, $N - \overline{1}_2$ where $\overline{1}_2$ is any integer congruent to 1 mod 2)) Wannier centers are necessary to be consistent with inversion symmetry as shown in Fig. 4.1 (d). This inability to maintain both the correct number of states and inversion symmetry leads to the quantization of fractional charge at boundaries in electronic systems and fractional mode density in PhCs and is called the filling anomaly.

The filling anomaly also presents a practical way to diagnose non-trivial topology by counting states in the spectrum of a finite system [94, 130]. The spectral consequence of the filling anomaly is that the states in the finite system within the frequency range of a single topological bulk band must have an odd number ($= \overline{1}_2$) of missing states as compared to the number of unit cells. These missing states are paired up with missing states from a different topological band in a way that preserves the inversion symmetry of the system and these typically reside inside the bandgap as boundary states. However, due to a lack additional symmetries that pin these boundary states to the middle of the gap, they could be pushed into a bulk band by inversion-symmetry preserving perturbations to the boundaries. Since such perturbations act identically on both boundaries of the system, the bulk band would gain an odd number of states. Crucially, regardless of the details of the perturbation, the number of expected states and the actual states within the frequency range of a single topological band will differ by $\overline{1}_2$; we refer to this as a "counting mismatch". In contrast, trivial boundary states, such as defect states, originate from a single band and would give rise to a counting mismatch of even ($= \overline{0}_2$) states for that band when there are two ends in the system related by inversion symmetry. Therefore, the counting mismatch is a $\mathbb{Z}_2$ invariant that can be determined directly from the frequency spectrum of the PhC and thus can reveal the topological nature of bulk bands.

To summarize this argument, in the absence of chiral or particle-hole symmetry, the bulk-boundary correspondence of topological 1D PhCs with inversion symmetry is subtle

in that the end states *may* or *may not* appear within a bandgap. However, regardless of their location in the frequency spectrum, the states within the frequency range of a topological band in a finite system *must* exhibit an odd-integer counting mismatch.

We now consider an explicit example of a 1D PhC consisting of alternating layers of TiO_2 ($\varepsilon = 6.25$) and air ($\varepsilon = 1$). The TiO_2 layer occupies a filling fraction $d/a = 0.6$ in the unit cell with lattice constant a. The first six bands of this 1D PhC are shown in Fig. 4.2 (a). Two distinct types of inversion-symmetric unit cells are possible for this PhC, as shown in the inset of Fig. 4.2 (a). The two types of unit cells are re-definitions of each other, related by a shift of $a/2$ along the x direction. The eigenvalues of $\mathcal{I}$ at the HSPs $\mathbf{\Gamma}$ and $\mathbf{X}$ for both types of unit cells as well as the Berry phase calculated using (4.7) are shown in the same plot. These show that while the band structure is identical for the two types of unit cells, the Berry phases and, correspondingly, the symmetry-indicator invariants are different. This is consistent with the fact that the re-definition of the unit cell shifts the Wannier center from the $1a$ position to the $1b$ position and, therefore, also the Berry phase from 0 to π and vice versa. This implies that if a band in one of the unit cell types is trivial, the corresponding band in the other type is topological.

Next, we simulate a large inversion-symmetric supercell with interfaces between the two types of unit cells in a strip geometry as shown in Fig. 4.2 (b). This supercell has two inversion-symmetry-related sectors with two ends and consists of a total of 61 unit cells. Therefore we expect to find 61 states per band in the spectrum of this supercell which is shown in Fig. 4.2 (c). However, due to the non-trivial topology of these bands (always originating from the inner or outer PhCs in the strip geometry), each band exhibits a counting mismatch of $\overline{1}_2$ states. For bands 1 to 4, we find the counting mismatch to be one missing state each and that these mismatched states reside in the bandgaps as end states whose field profiles are shown in Fig. 4.2 (d). For band 5, we find a counting mismatch of three missing states, two of which reside in the fourth gap and are trivial states since they originate from the same band. The remaining missing state is paired with another state from band 6. However, we can see that this pair of mismatched states does not lie inside a bandgap but is instead degenerate with band 6. As a result, we find a counting mismatch of one additional state for band 6.

The in-gap topological end states discussed above have been directly observed in experiments in 1D PhCs and 1D periodic-dielectric waveguides [65–67].

Having introduced the notion of topological bands in the presence of crystalline symmetries in 1D, we now extend the topological classification and characterization of photonic bands to 2D.

4.3 2D photonic crystals

Two-dimensional PhCs consist of a periodic patterning of the dielectric along two directions (x and y) and a uniform dielectric profile along the third direction (z), with wave propagation restricted to lie in the x, y plane. For such a system, the equations in (4.2) can be simplified by exploiting the mirror symmetry through the x, y plane that sends $z \to -z$. This separates the states into two orthogonal polarizations: transverse electric (TE) with $\mathbf{E}(\mathbf{r}) = \mathcal{E}_x(x,y)\hat{\mathbf{x}} + \mathcal{E}_y(x,y)\hat{\mathbf{y}}$, $\mathbf{H}(\mathbf{r}) = \mathcal{H}_z(x,y)\hat{\mathbf{z}}$, which is even under the mirror symmetry, and transverse magnetic (TM) with $\mathbf{E}(\mathbf{r}) = \mathcal{E}_z(x,y)\hat{\mathbf{z}}$, $\mathbf{H}(\mathbf{r}) = \mathcal{H}_x(x,y)\hat{\mathbf{x}} + \mathcal{H}_y(x,y)\hat{\mathbf{y}}$, which is odd under the mirror symmetry. For these generally non-degenerate TE and TM polarizations, the eigenvalue problem is most easily solved for the scalar fields $\mathcal{H}_z(x,y)$ and $\mathcal{E}_z(x,y)$ respectively, using [4]

$$\begin{aligned} -\left[\frac{\partial}{\partial x}\frac{1}{\varepsilon(x,y)}\frac{\partial}{\partial x} + \frac{\partial}{\partial y}\frac{1}{\varepsilon(x,y)}\frac{\partial}{\partial y}\right]\mathcal{H}_z(x,y) &= \frac{\omega^2}{c^2}\mathcal{H}_z(x,y) \\ -\frac{1}{\varepsilon(x,y)}\left[\frac{\partial^2}{\partial x^2} + \frac{\partial^2}{\partial y^2}\right]\mathcal{E}_z(x,y) &= \frac{\omega^2}{c^2}\mathcal{E}_z(x,y) \end{aligned} \tag{4.11}$$

Similar to the 1D case, these eigenvalue problems can be solved using Bloch's theorem, and the solutions are distributed into frequency bands with their momenta being restricted to the first 2D BZ. Since TE and TM polarizations are orthogonal, we restrict the discussion to a single polarization of choice. We now characterize the topological phases of 2D PhCs by first constructing the topological invariants that classify them under different point group symmetries and then deriving bulk-boundary correspondences and their associated index theorems.

In 2D, the classification of PhCs can be divided into whether they obey time-reversal symmetry (TRS) (class AI) or not (class A). Without crystalline symmetries, class AI does not host topological phases. In contrast, class A hosts topological phases characterized by the Chern number ($C \in \mathbb{Z}$) that encodes the number of chiral edge states at the boundaries of a finite system. The Chern number also presents an obstruction to the construction of exponentially localized Wannier functions, and hence such bands are referred to as non-Wannierizable [5, 131]. However, when the Chern number vanishes, and in the presence of crystalline symmetries, photonic bands may be associated with Wannier centers fixed at maximal Wyckoff positions of the 2D unit cells (Fig. 4.3). If this association is possible, each distinct configuration of Wannier centers uniquely identifies

a topological phase protected by symmetry. As mentioned previously, such bands are collectively called atomic limits; in particular, obstructed atomic limits (OAL) refer to cases where the Wannier centers are displaced away from the center of the unit cell. Under some circumstances, a Wannier representation of bands may not be possible despite their vanishing Chern number. Such bands are termed *fragile* and have the property of admitting a Wannier representation when considered as a set that includes additional specific atomic limit bands.

Similar to 1D, the location of Wannier centers for 2D PhCs can be identified using Berry phases. However, when bands are degenerate, they must be treated collectively, which requires the use of Wilson loops [132, 133]. The Wilson loop is defined as

$$\mathcal{W}(\mathcal{C}) = \mathcal{P} \exp\left[\left(\int_{\mathcal{C}} \mathcal{A}(\mathbf{k}) \cdot d\mathbf{k}\right)\right] \tag{4.12}$$

where $\mathcal{C}$ is a closed contour in $\mathbf{k}$-space, $\mathcal{P}$ denotes a path ordering of the exponential and $\mathcal{A}(\mathbf{k})$ is the multi-band Berry connection given by

$$\mathcal{A}(\mathbf{k}) \equiv \mathcal{A}_{m,n}(\mathbf{k}) = -\mathrm{i} \left\langle u_{\mathbf{k},m} \left| \nabla_{\mathbf{k}} \right| u_{\mathbf{k},n} \right\rangle . \tag{4.13}$$

When $\mathcal{C}$ is taken to be a straight line in the Brillouin zone, the Wilson loop eigenvalues are proportional to the expectation values of the position operator in the same direction. Therefore, similar to the Berry phase, the eigenvalues of the Wilson loop, when considered in two linearly independent directions, indicate the locations of Wannier centers for a group of OAL bands or indicate the non-Wannierizable nature of fragile bands or Chern bands by their non-trivial winding [5, 111]. The calculations of these Wilson loops are also simplified by looking at the representations of the eigenmodes at the HSPs of the BZ to diagnose each of these situations for a single band or group of bands.

4.3.1 Classification due to rotational symmetries

Consider a projector into the bands of interest given by $P_k = \sum_j \left| u_{j,k} \right\rangle \left\langle u_{j,k} \right|$. The eigenvalues of the rotation operator, $\hat{r}_n$, projected into the bands of interest at the HSP $\mathbf{\Pi}$, $P_{\mathbf{\Pi}} \hat{r}_n P_{\mathbf{\Pi}}$, are

$$\mathbf{\Pi}_p^{(n)} = e^{2\pi \mathrm{i}(p-1)/n}, \quad \text{for } p = 1, 2, \ldots n. \tag{4.14}$$

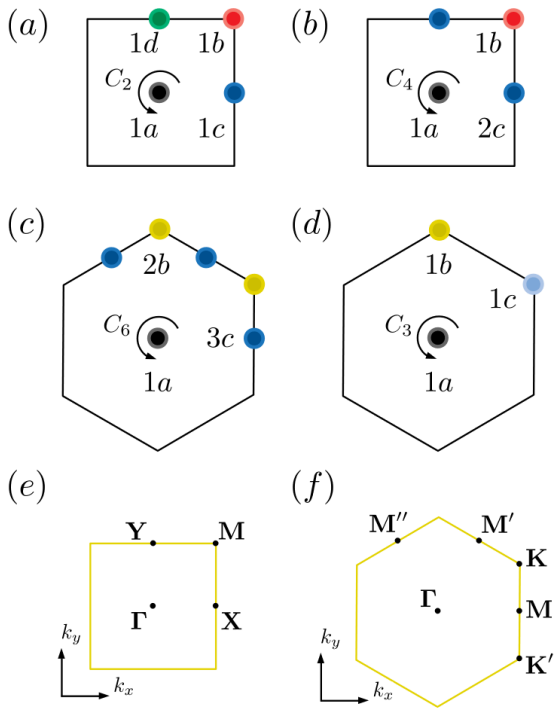

Figure 4.3. Maximal Wyckoff positions for (a) C_2 (b) C_4 (c) C_6 and (d) C_3 symmetric unit cells. (e) BZ of a square lattice with possible HSPs. (f) BZ of a triangular lattice with possible HSPs.

Following previous studies on the characterization of the topology of energy bands in condensed matter systems [114], we define the integer invariants

$$[\Pi_p^{(n)}] \equiv \#\mathbf{\Pi}_p^{(n)} - \#\mathbf{\Gamma}_p^{(n)} \quad \in \mathbb{Z}, \tag{4.15}$$

where $\#\mathbf{\Pi}_p^{(n)}$ is the number of states in the frequency band(s) in question with rotation operator eigenvalue $\mathbf{\Pi}_p^{(n)}$.

These invariants can be constructed for 2D lattices with C_n symmetry at all high symmetry points shown in Fig. 4.3 (e) and (f). However, some of the invariants in (4.15) are redundant for three reasons: (i) Rotation symmetry forces representations at certain HSPs to be the same. Particularly, C_4 symmetry forces equal representations at $\mathbf{X}$ and $\mathbf{Y}$, while C_6 symmetry forces equal representations at $\mathbf{M}$, $\mathbf{M}'$, and $\mathbf{M}''$, as well as at $\mathbf{K}$ and $\mathbf{K}'$; (ii) the fact that the number of bands in consideration is constant across the BZ, from which it follows that $\sum_p \#\mathbf{\Pi}_p^{(n)} = \sum_p \#\mathbf{\Gamma}_p^{(n)}$, or $\sum_p [\Pi_p^{(n)}] = 0$; and (iii) the existence of TRS, which implies that the Chern number will be zero and that rotation eigenvalues at $\mathbf{\Pi}^{(n)}$ and $-\mathbf{\Pi}^{(n)}$ are related by complex conjugation. This leads to $[M_2^{(4)}] = [M_4^{(4)}]$ (for C_4), $[K_2^{(3)}] = [K_3^{\prime(3)}]$ (for C_3), $[K_3^{(3)}] = [K_2^{\prime(3)}]$ (for C_3), $[K_1^{(3)}] = [K_1^{\prime(3)}]$ (for C_3) and

$[K_2^{(3)}] = [K_3^{(3)}]$ (for C_6).

Therefore, in the presence of TRS (class AI in the tenfold way), the classification is given by the following indices [114]

$$\begin{aligned}
\chi_{\mathcal{T}}^{(2)} &= \left([X_1^{(2)}], [Y_1^{(2)}], [M_1^{(2)}]\right) \\
\chi_{\mathcal{T}}^{(3)} &= \left([K_1^{(3)}], [K_2^{(3)}]\right) \\
\chi_{\mathcal{T}}^{(4)} &= \left([X_1^{(2)}], [M_1^{(4)}], [M_2^{(4)}]\right) \\
\chi_{\mathcal{T}}^{(6)} &= \left([M_1^{(2)}], [K_1^{(3)}]\right).
\end{aligned} \tag{4.16}$$

On breaking TRS, the classification of 2D C_n-symmetric PhCs must include the Chern number since it can now admit non-zero values. Furthermore, breaking TRS reduces the number of constraints on the invariants (i.e., condition (iii) above is relaxed) and therefore increases the number of invariants required to identify topological phases uniquely. Taking into account these considerations, the most general classification (class A in the tenfold way) of 2D C_n-symmetric PhCs is given by the following indices

$$\begin{aligned}
\chi^{(2)} &= \left(C \,\middle|\, [X_1^{(2)}], [Y_1^{(2)}], [M_1^{(2)}]\right) \\
\chi^{(3)} &= \left(C \,\middle|\, [K_1^{(3)}], [K_2^{(3)}], [K_1'^{(3)}], [K_2'^{(3)}]\right) \\
\chi^{(4)} &= \left(C \,\middle|\, [X_1^{(2)}], [M_1^{(4)}], [M_2^{(4)}], [M_4^{(4)}]\right) \\
\chi^{(6)} &= \left(C \,\middle|\, [M_1^{(2)}], [K_1^{(3)}], [K_2^{(3)}]\right),
\end{aligned} \tag{4.17}$$

where C is the Chern number given by

$$C = \frac{1}{2\pi} \int_{\mathrm{BZ}} \mathrm{Tr}[\nabla_{\mathbf{k}} \times \mathcal{A}(\mathbf{k})] d^2\mathbf{k}. \tag{4.18}$$

Similar to the 1D case, we can exhaustively calculate the values of $\chi^{(n)}$ (when $C = 0$) or $\chi_{\mathcal{T}}^{(n)}$ following the approach of induction of band representations. To perform this, we require knowledge about the Wannier functions' internal symmetry representation, known as "site symmetry representation", $\rho(C_n)$, as well as the location of their gauge-invariant centers, the Wannier centers. We summarize the results in Tables 4.1-4.4. Furthermore, these tables also show the number of bands required to generate the corresponding indices.

There are relations between the Chern number (4.18) and the symmetry-indicator

# Bands	WP	Site symm.	$\chi_{\mathcal{T}}^{(2)}$	$\chi^{(2)}$
1	$1a$	$\rho(C_2) = \text{any}$	$(0,0,0)$	$(0\,\vert\,0,0,0)$
1	$1c$	$\rho(C_2) = +1$	$(-1,0,-1)$	$(0\,\vert\,-1,0,-1)$
1	$1c$	$\rho(C_2) = -1$	$(1,0,1)$	$(0\,\vert\,1,0,1)$
1	$1d$	$\rho(C_2) = +1$	$(0,-1,-1)$	$(0\,\vert\,0,-1,-1)$
1	$1d$	$\rho(C_2) = -1$	$(0,1,1)$	$(0\,\vert\,0,1,1)$
1	$1b$	$\rho(C_2) = +1$	$(-1,-1,0)$	$(0\,\vert\,-1,-1,0)$
1	$1b$	$\rho(C_2) = -1$	$(1,1,0)$	$(0\,\vert\,1,1,0)$

Table 4.1. C_2 symmetry: Indices induced from all possible maximal Wyckoff positions.

# Bands	WP	Site symm.	$\chi_{\mathcal{T}}^{(3)}$	$\chi^{(3)}$
1	$1a$	$\rho(C_3) = \text{any}$	$(0,0)$	$(0\,\vert\,0,0,0,0)$
1	$1b$	$\rho(C_3) = +1$	$(-1,1)$	$(0\,\vert\,-1,1,-1,0)$
2	$1b$	$\rho(C_3) = e^{\mathrm{i}\frac{2\pi}{3}\sigma_z}$	$(1,-1)$	$(0\,\vert\,1,-1,1,0)$
1	$1b$	$\rho(C_3) = e^{\mathrm{i}\frac{2\pi}{3}}$	-	$(0\,\vert\,0,-1,1,-1)$
1	$1b$	$\rho(C_3) = e^{\mathrm{i}\frac{4\pi}{3}}$	-	$(0\,\vert\,1,0,0,1)$
1	$1c$	$\rho(C_3) = +1$	$(-1,0)$	$(0\,\vert\,-1,0,-1,1)$
2	$1c$	$\rho(C_3) = e^{\mathrm{i}\frac{2\pi}{3}\sigma_z}$	$(1,0)$	$(0\,\vert\,1,0,1,-1)$
1	$1c$	$\rho(C_3) = e^{\mathrm{i}\frac{2\pi}{3}}$	-	$(0\,\vert\,1,-1,0,-1)$
1	$1c$	$\rho(C_3) = e^{\mathrm{i}\frac{4\pi}{3}}$	-	$(0\,\vert\,0,1,1,0)$

Table 4.2. C_3 symmetry: Indices induced from all possible maximal Wyckoff positions.

# Bands	WP	Site symm.	$\chi_{\mathcal{T}}^{(4)}$	$\chi^{(4)}$
1	$1a$	$\rho(C_4) = \text{any}$	$(0,0,0)$	$(0\,\vert\,0,0,0,0)$
2	$2c$	$\rho(C_2) = +1$	$(-1,-1,1)$	$(0\,\vert\,-1,-1,1,1)$
2	$2c$	$\rho(C_2) = -1$	$(1,1,-1)$	$(0\,\vert\,1,1,-1,-1)$
1	$1b$	$\rho(C_4) = +1$	$(-1,-1,0)$	$(0\,\vert\,-1,-1,0,0)$
1	$1b$	$\rho(C_4) = -1$	$(-1,1,0)$	$(0\,\vert\,-1,1,0,0)$
2	$1b$	$\rho(C_4) = \mathrm{i}\sigma_z$	$(2,0,0)$	$(0\,\vert\,2,0,0,0)$
1	$1b$	$\rho(C_4) = +\mathrm{i}$	-	$(0\,\vert\,1,0,-1,1)$
1	$1b$	$\rho(C_4) = -\mathrm{i}$	-	$(0\,\vert\,1,0,1,-1)$

Table 4.3. C_4 symmetry: Indices induced from all possible maximal Wyckoff positions.

# Bands	WP	Site symm.	$\chi_{\mathcal{T}}^{(6)}$	$\chi^{(6)}$
1	$1a$	$\rho(C_6) = \text{any}$	$(0,0)$	$(0\,\vert\,0,0,0)$
2	$2b$	$\rho(C_3) = +1$	$(0,-2)$	$(0\,\vert\,0,-2,1)$
4	$2b$	$\rho(C_3) = e^{\mathrm{i}\frac{2\pi}{3}\sigma_z}$	$(0,2)$	$(0\,\vert\,0,2,-1)$
2	$2b$	$\rho(C_3) = e^{\mathrm{i}\frac{2\pi}{3}}$	-	$(0\,\vert\,0,1,-2)$
2	$2b$	$\rho(C_3) = e^{\mathrm{i}\frac{4\pi}{3}}$	-	$(0\,\vert\,0,1,1)$
3	$3c$	$\rho(C_2) = +1$	$(-2,0)$	$(0\,\vert\,-2,0,0)$
3	$3c$	$\rho(C_2) = -1$	$(2,0)$	$(0\,\vert\,2,0,0)$

Table 4.4. C_6 symmetry: Indices induced from all possible maximal Wyckoff positions.

invariants in the classifications (4.17). These relations are given by

$$\begin{aligned}
C &= -[X_1^{(2)}] - [Y_1^{(2)}] - [M_1^{(2)}] \mod 2 \\
C &= -[K_1^{(3)}] - 2[K_2^{(3)}] + 2[K_1'^{(3)}] + [K_2'^{(3)}] \mod 3 \\
C &= 2[M_1^{(4)}] + [M_2^{(4)}] - [M_4^{(4)}] - 2[X_1^{(2)}] \mod 4 \\
C &= -8[K_1^{(3)}] - 4[K_2^{(3)}] + 3[M_1^{(2)}] \mod 6
\end{aligned} \tag{4.19}$$

The consequence of these relations is that the symmetry-indicator invariants provide a fast and simple way to calculate the Chern number (mod n) for C_n-symmetric PhCs with broken TRS.

4.3.2 Index theorems

C_n-symmetric PhCs with different $\chi^{(n)}$ or $\chi_{\mathcal{T}}^{(n)}$ belong to different topological phases, as they cannot be deformed into one another without closing the bulk energy gap or breaking the symmetry [116, 134, 135]. Furthermore, for Wannierizable bands with a vanishing Chern number, the Wannier center configuration directly determines the existence of a filling anomaly and consequently the possible existence of in-gap edge and corner states. Therefore, finding the symmetry-indicator invariants is useful in establishing a bulk-boundary correspondence for such bands. The presence of edge states is directly related to the dipole moment of the Wannier centers. In 1D, this takes the form of (4.10) whereas in 2D, Ref. [114] showed that the bands have dipole moments

indicated by

$$\begin{aligned}
\mathbf{P}^{(2)} &= \frac{1}{2}\left([Y_1^{(2)}] + [M_1^{(2)}]\right)\mathbf{a_1} + \frac{1}{2}\left([X_1^{(2)}] + [M_1^{(2)}]\right)\mathbf{a_2} \\
\mathbf{P}^{(4)} &= \frac{1}{2}[X_1^{(2)}](\mathbf{a_1} + \mathbf{a_2}) \\
\mathbf{P}^{(6)} &= \mathbf{0},
\end{aligned} \tag{4.20}$$

where the superscript n in $\mathbf{P}^{(n)}$ labels the C_n symmetry. The dipole moments in (4.20) are defined modulo 1 and are valid for both TR-symmetric and TR-broken PhCs, as long as the Chern number vanishes. $\mathbf{P}$ is a $\mathbb{Z}_2 \times \mathbb{Z}_2$ index for C_2 symmetry and $\mathbb{Z}_2$ index for C_4 symmetry. In all cases, non-trivial $\mathbf{P}$ is associated with an edge-induced filling anomaly.

We note that for 2D spinless systems, such as the PhCs considered here, $\mathcal{I}$ and C_2 have identical transformation properties and are isomorphic operations that send $x, y \to -x, -y$. Therefore, for C_2, C_4 and C_6 symmetries, a non-trivial $\mathbf{P}$ is associated with a counting mismatch of $\overline{1}_2$ in the edge spectrum since inversion symmetry ($\mathcal{I}$) is a subgroup of these rotations and an edge supercell (with one periodic direction) can always be chosen such that $\mathcal{I}$ is maintained. In the case of C_2 symmetry, the counting mismatch is a $\mathbb{Z}_2 \times \mathbb{Z}_2$ invariant as edge supercells in both directions must be independently considered (i.e., finite-in-x, periodic-in-y or finite-in-y, periodic-in-x). In the case of C_4 symmetry, the edge spectrum is identical in both directions, and therefore the counting mismatch is a $\mathbb{Z}_2$ invariant. In the case of C_6 symmetry, both $\mathbf{P}$ and the counting mismatch in the edge spectrum are always trivial.

In the case of C_3 symmetry, the dipole moment is given by

$$\begin{aligned}
\mathbf{P}^{(3)} &= \frac{2}{3}\left([K_1^{(3)}] + 2[K_2^{(3)}]\right)(\mathbf{a_1} + \mathbf{a_2}) \quad \text{(under TRS)} \\
\mathbf{P}^{(3)} &= \left([K_1^{(3)}] + [K_2^{(3)}] - \frac{2}{3}[K_1'^{(3)}] - \frac{1}{3}[K_2'^{(3)}]\right)(\mathbf{a_1} + \mathbf{a_2}) \quad \text{(under broken TRS)},
\end{aligned} \tag{4.21}$$

where $\mathbf{P}^{(3)}$ is a $\mathbb{Z}_3$ index for C_3 symmetry. Since $\mathcal{I}$ is not a subgroup of C_3 symmetry, an edge supercell can never be chosen such that $\mathcal{I}$ is maintained. Therefore, the counting mismatch cannot distinguish between different values of $\mathbf{P}^{(3)}$. Instead, in this case, the fractionalization of energy density at the edges must be directly calculated using the eigenmodes of a C_3-symmetric finite system.

Additionally, some Wannier center configurations can lead to higher-order topological

states. In class AI, these phases are determined by the corner "charges"[1]

$$
\begin{aligned}
Q^{(2)}_{\text{corner},\mathcal{T}} &= \frac{1}{4}\left(-[X_1^{(2)}] - [Y_1^{(2)}] + [M_1^{(2)}]\right) \\
Q^{(3)}_{\text{corner},\mathcal{T}} &= \frac{1}{3}[K_2^{(3)}] \\
Q^{(4)}_{\text{corner},\mathcal{T}} &= \frac{1}{4}\left([X_1^{(2)}] + 2[M_1^{(4)}] + 3[M_2^{(4)}]\right) \\
Q^{(6)}_{\text{corner},\mathcal{T}} &= \frac{1}{4}[M_1^{(2)}] + \frac{1}{6}[K_1^{(3)}],
\end{aligned}
\tag{4.22}
$$

as shown initially in Ref. [114]. We extend this to class A, where they are

$$
\begin{aligned}
Q^{(2)}_{\text{corner}} &= \frac{1}{4}\left(-[X_1^{(2)}] - [Y_1^{(2)}] + [M_1^{(2)}]\right) \\
Q^{(3)}_{\text{corner}} &= \frac{1}{3}\left([K_1^{(3)}] + [K_2^{(3)}] - [K_1'^{(3)}]\right) \\
Q^{(4)}_{\text{corner}} &= \frac{1}{4}\left([X_1^{(2)}] + 2[M_1^{(4)}] + \frac{3}{2}[M_2^{(4)}] + \frac{3}{2}[M_4^{(4)}]\right) \\
Q^{(6)}_{\text{corner}} &= \frac{1}{4}[M_1^{(2)}] + \frac{2}{3}[K_1^{(3)}],
\end{aligned}
\tag{4.23}
$$

$Q^{(n)}_{\text{corner},\mathcal{T}}$ (for TR-symmetric) or $Q^{(n)}_{\text{corner}}$ (for TR-broken), are $\mathbb{Z}_n$ topological quantities and are associated with a corner-induced filling anomaly, a counting mismatch of states $\in \{\overline{0}_n, \ldots \overline{n-1}_n\}$ in a finite system with n symmetry-related sectors and possibly the presence of in-gap corner-localized states. $\mathbf{P}$ and Q can simultaneously admit non-trivial values, leading to both edge and corner states that may be degenerate with each other and/or with the bulk bands. However, their associated counting mismatch remains robust. We note that in fermionic systems, where insulating states rely on completely filled bands, a quantization of corner charge requires $\mathbf{P}^{(n)} = \mathbf{0}$. In photonic systems, however, we are only concerned with the *existence* of localized states, and the $\mathbf{P}^{(n)} = \mathbf{0}$ constraint can be relaxed.

We have assumed that the Chern number vanishes in the TR-broken case and that we have OAL bands with well-defined Wannier centers that lead to corner charges. However, it is possible for fractional charges to localize at disclinations in C_n-symmetric systems with non-Wannierizable Chern bands. In such cases, the formulae for disclination charges contain a Chern number contribution along with contributions from the symmetry-indicator invariants [136]. We note that the formulae in (4.23) are consistent with the

[1]In PhCs, the analogous quantity to electronic charges that is fractionally quantized at corners is the electromagnetic energy density.

disclination charges given in Ref. [136] with a vanishing Chern number contribution, as is expected.

4.4 Design and characterization of 2D topological photonic crystals

In the previous sections, we exhaustively built the topological classifications in class A and AI and identified the indices that correspond to OAL phases via the induction of the band representations from the symmetry representation of the Wannier functions and the Wyckoff positions of their Wannier centers. This classification forms a linear algebraic structure, such that when two bands of a C_n symmetric system, in phases χ_1 and χ_2 respectively, are combined, this set of bands is in the phase $\chi_1 + \chi_2$. This observation forms the basis of a strategy we now propose to diagnose and design topological PhCs.

Given a PhC, our starting point is the calculation of the C_n symmetry representations at HSPs for N bands to determine $\chi^{(n)}$, which can always be expressed as the following linear combination

$$\chi^{(n)} = \sum_p \alpha_p \, \chi_p^{(n)} \tag{4.24}$$

where $\chi_p^{(n)}$ correspond to the indices of OALs in Tables 4.1-4.4. Since the $\chi_p^{(n)}$ for different site symmetry representations for the same Wannier center configuration are linearly dependent, the linear combination in (4.24) is non-unique, and all possible linear combinations must be examined to obtain the correct topological characterization. Furthermore, a comparison must be made between the number of bands in question with the number of Wannierizable bands required to give rise to the index $\chi^{(n)}$; this comparison helps identify bands that are not Wannierizable.

The topology of this set of N bands can be inferred using the following guidelines: (i) If the bands are in an OAL phase, at least one possible linear combination exists such that the coefficients $\{\alpha_p\}$ are all positive integers (converse is not true). Additionally, for an OAL phase, the number of bands required to generate the index $\chi^{(n)}$, as inferred from the linear combination, must not exceed the total number of bands in question (this accounts for the possibility of trivial atomic limit bands, with $\chi = 0$, being counted among the total number of bands but leaving $\chi^{(n)}$ unchanged). (ii) If a linear combination with an integer $\{\alpha_p\}$ is not possible, the bands are either gapless under TRS, in which

case we have a Dirac semi-metal phase, or are gapped and have a non-vanishing Chern number under broken TRS. (iii) If all possible linear combinations are such that $\{\alpha_p\}$ are integers, but at least one coefficient is negative, the bands are in a fragile topological phase. Alternatively, if $\{\alpha_p\}$ are positive integers but the number of bands required to generate $\chi^{(n)}$ exceeds the total number of bands in question, the bands are also fragile.

In the following sections, we provide examples that illustrate these cases.

4.4.1 Example 1: OAL phase with four-fold rotation in class AI

We now show an example of an OAL phase and its associated boundary signatures in a 2D PhC. Similar OAL phases have been widely implemented in PhCs [88–93, 98, 99]. Consider two PhCs with unit cells shown in the inset of Fig. 4.4 (a), which consist of four dielectric square pillars in a C_{4v}-symmetric configuration with $\varepsilon = 12$. These two unit cell choices, referred to as "expanded" and "contracted", are related to each other by a half-lattice-constant shift along the x and y directions. We consider the first four TM bands for the following analysis. The symmetry-indicator invariants can be computed using the irreducible representations (irreps) of C_{4v} and its little groups at the HSPs. For the contracted unit cell, bands 1, $2+3$ and 4, all have the index $\chi_{\mathcal{T}}^{(4)} = (0,0,0)$ which corresponds to Wannier centers located at the $1a$ Wyckoff position in the 2D unit cell shown in Fig. 4.3 (b). For the expanded unit cell, bands 1 and 4 have the indices $\chi_{\mathcal{T}}^{(4)} = (-1,-1,0)$ and $\chi_{\mathcal{T}}^{(4)} = (-1,+1,0)$ respectively. Bands 2 and 3 are degenerate at $\mathbf{\Gamma}$ and $\mathbf{M}$ points and have the combined index $\chi_{\mathcal{T}}^{(4)} = (2,0,0)$. Each of these indices corresponds to the Wannier centers at the $1b$ Wyckoff position. These indices lead to $\mathbf{P}^{(4)} = (1/2, 1/2)$ and $Q^{(4)}_{\text{corner},\mathcal{T}} = 1/4$ for bands 1 and 4 and $\mathbf{P}^{(4)} = \mathbf{0}$ and $Q^{(4)}_{\text{corner},\mathcal{T}} = 1/2$ for bands 2+3 .

Alternatively, in this case, it is also possible to extract the position of the Wannier center and therefore their dipole moments and corner charges by using Wilson loops as shown in Fig. 4.4 (b). Here, the Wilson loop eigenvalues for each band are calculated by integrating the Berry connection along one momentum direction and plotting it as a function of the other momentum. This indicates the locations of the hybrid Wannier centers that are exponentially localized in one spatial direction but are de-localized in the other spatial direction. For a C_4-symmetric system, the Wilson loop spectrum along k_x is identical to that along k_y. The plots for the contracted unit cell show that the Wannier functions for the first four bands can be simultaneously localized in both directions and that their Wannier centers are located at the $1a$ position in the 2D unit cell, corresponding to the trivial atomic limit deformable to $(\mathcal{W}_x(k_y), \mathcal{W}_y(k_x)) = (0,0)$ [126].

Similarly, for the expanded unit cell, the Wannier centers are located at the $1b$ position in the 2D unit cell, corresponding to an OAL deformable to $(\mathcal{W}_x(k_y), \mathcal{W}_y(k_x)) = (\pi, \pi)$.

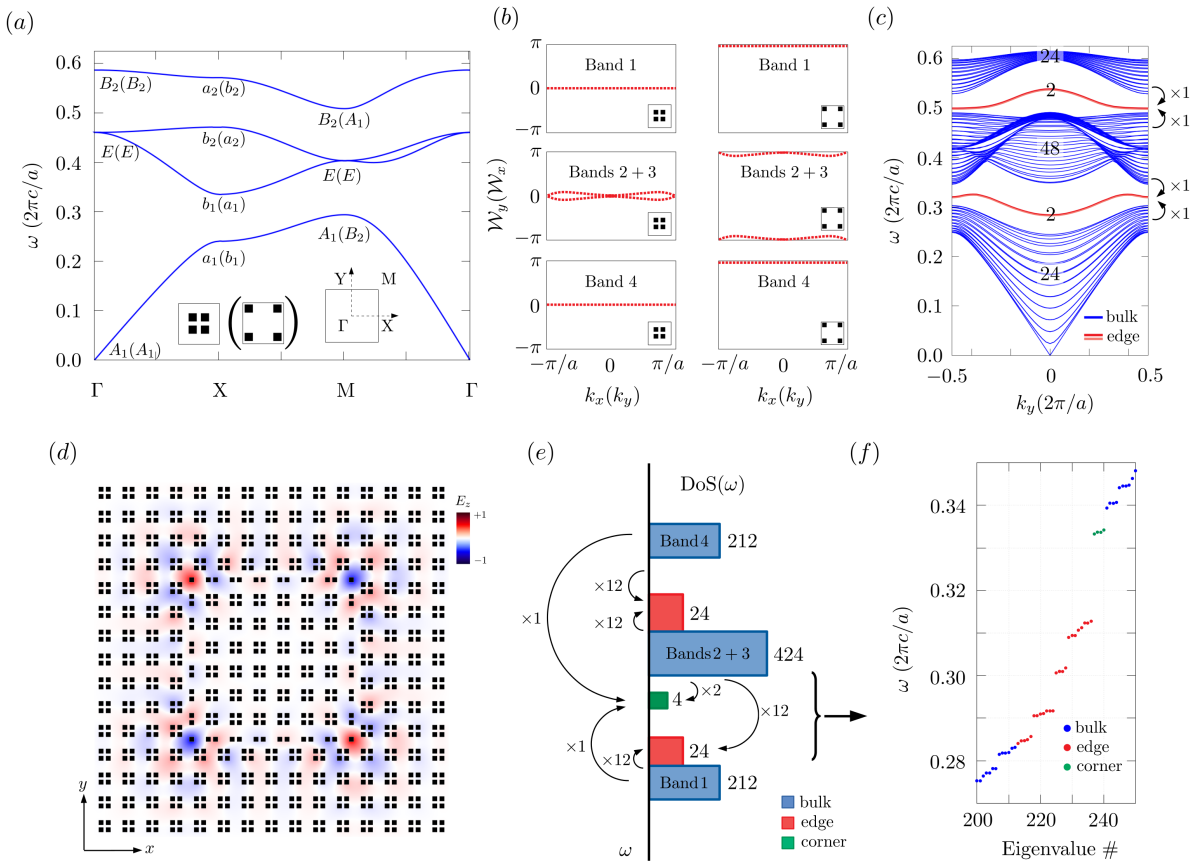

Figure 4.4. (a) TM-polarized band structure of a C_{4v} symmetric PhC with $\varepsilon = 12$. The two possible types of C_4-symmetric unit cells are shown in the insets along with the 2D BZ. The little group irreps of the electromagnetic eigenmodes at HSPs are shown for the first four bands. (b) Wilson loop eigenvalues $\mathcal{W}_y(\mathcal{W}_x)$ for bands 1, $2+3$ and 4 along $k_x(k_y)$ for both types of unit cells. (c) Edge spectrum consisting a total of 25 unit cells of the two types in a strip configuration. An odd-integer counting mismatch per band leads to the presence of edge states in the first and second TM bandgaps. (d) The dielectric and E_z mode profile of one of the four corner modes in a finite system of size 15×15 unit cells consisting of the two types of unit cells in a core-cladding configuration. (e) A schematic of the DoS for the structure in (d). A counting mismatch of states for bands 1 to 4 leads to four degenerate corner states in the first TM bandgap. The counting mismatch for the edge states depends on the system size for such a finite configuration. (f) The spectrum in the vicinity of the first TM bandgap for the finite system shown in (d). The bulk, edge, and corner states are identified with blue, red, and green dots respectively.

To see that the dipole moments lead to edge states, we simulate a finite system consisting of the expanded and contracted unit cells in a strip geometry. The strip geometry is a large supercell consisting of an inner domain with the expanded unit cell and an outer domain with the contracted unit cell with periodic boundaries along both directions. This supercell consists of 25 unit cells, and therefore the spectrum should contain 25 states per band. However, due to the non-zero dipole moments, bands 1 and 4 have a counting mismatch of one missing state ($= \overline{1}_2$) each, whereas bands 2+3 have a vanishing dipole moment and have a counting mismatch of two missing states ($= \overline{0}_2$) as shown in the edge spectrum in Fig. 4.4 (c). Due to the equal dipole moments along x and y directions and the symmetries of the system, the edge spectrum is identical along both x and y directions.

The non-zero corner charges for bands 1 to 4 will similarly lead to a counting mismatch and the presence of corner states in a finite system with corners. To explore this, we simulate a finite C_4-symmetric system in a core-cladding configuration as shown in Fig. 4.4 (d). This finite configuration has four symmetry-related sectors with four corners. A schematic of the spectrum of the finite system, up to the frequency range of the first four TM bands is shown in Fig. 4.4 (e). The bulk, edge, and corner states have been identified from their localization and mode profiles. The finite system has a size of $15 \times 15 = 225$ unit cells, and therefore each band contributes 225 states to the spectrum. However, the dipole moment of the Wannier centers leads to edge states on all edges, as seen previously in Fig. 4.4 (c). In the finite configuration, these edge states have a size-dependent counting mismatch: the 24 boundary unit cells in this example host 24 edge states. In addition to this, the counting mismatch due to the corners is size-independent and is identified as equal to one missing state ($= \overline{1}_4$) each for bands 1 and 4 and two missing states for bands 2+3 ($= \overline{2}_4$). Even if a C_4-preserving perturbation to the corners pushes the four corner states into any of the bulk bands, the counting mismatch for these bands remains unchanged. For example, if the four corner states were pushed into band 1, the counting mismatch for band 1 would go from one missing state to three additional states, both of which are equal modulo 4.

4.4.2 Example 2: Dirac semi-metal in class AI

Next, we show the topological characterization of a PhC with generic Dirac points in class AI. Consider the PhC as shown in the inset of Fig. 4.5 (a), which consists of an elliptical disc ($\varepsilon = 12$) with its semi-major and semi-minor axes oriented along the diagonals of a square unit cell. This PhC exhibits two sets of Dirac points along the $\mathbf{\Gamma} - \mathbf{M}$ direction

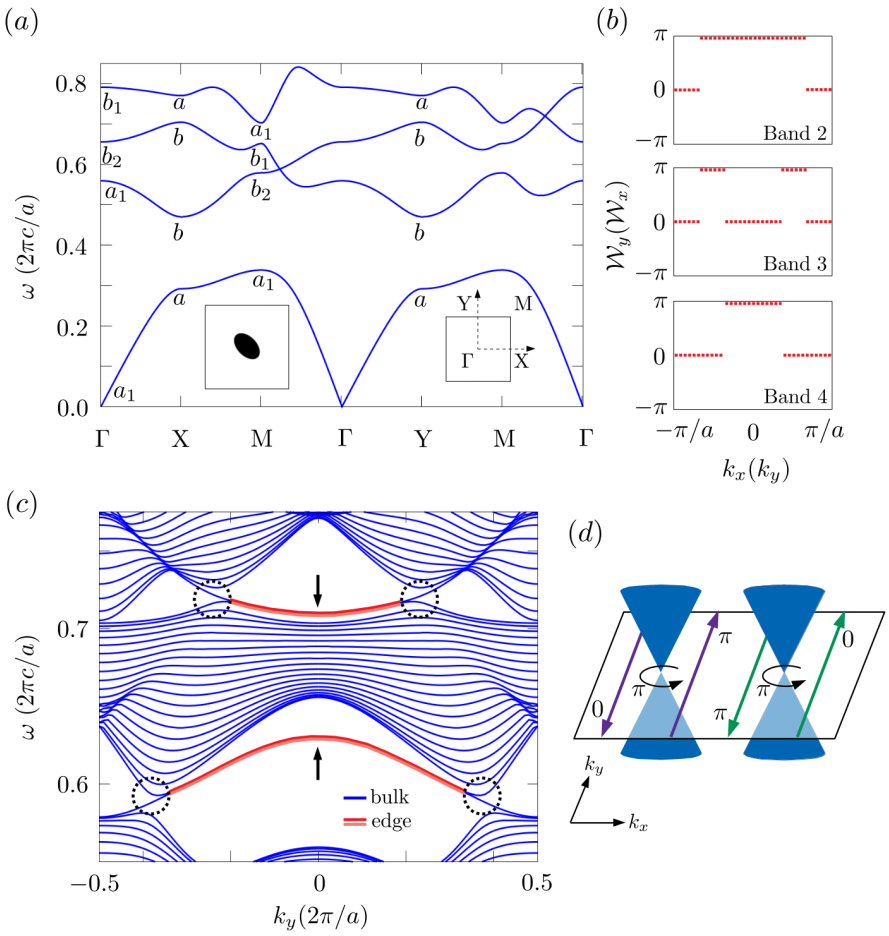

Figure 4.5. (a) TM-polarized band structure of a C_{2v}-symmetric PhC whose unit cell is shown in the inset. The little group irreps of the electromagnetic eigenmodes at HSPs are shown for the first four bands. (b) Wilson loop eigenvalues $\mathcal{W}_y(\mathcal{W}_x)$ for the bands 2, 3 and 4 plotted as a function of $k_x(k_y)$. The discontinuities indicate the presence of Dirac points. (c) Edge spectrum of this PhC showing edge states (marked with arrows) whose dispersion terminates at Dirac points (marked with circles) on the left (red) and right (light red) edges. (d) Dirac points are gap-closing points that separate 1D topological phases with different Berry phases. They can be thought of as sources of Berry phase.

between TM bands 2, 3, and 4 as shown in Fig. 4.5 (a). These Dirac points separate trivial and topological gapped phases of a 1D subsystem that is obtained by fixing one of the momenta, say k_y, while varying k_x across its entire range, constituting a 1D Brillouin zone. In this example, the C_{2v} irreps at the HSPs indicate that bands 2 and 4 have different C_2 (and hence $\mathcal{I}$) eigenvalues at the **Γ** and **X** points, corresponding to a 1D topological phase at the $k_y = 0$ cut with $[X_1] = 1$ (or equivalently, $\theta = \pi$). On the other hand, these bands have the same C_2 (and hence $\mathcal{I}$) eigenvalues at the **Y** and **M** points, corresponding to a trivial phase at the $k_y = \pi/a$ cut with $[X_1] = 0$ (or equivalently, θ

$= 0$).

This change in topology of the one-dimensional subsystem at the Dirac points can also be seen in the Wilson loop spectrum. The Wilson loop eigenvalues plotted in Fig. 4.5 (b) exhibit jump discontinuities from 0 to π at the momenta of the Dirac points, which correspond to a switch in the value of $[X_1]$ from 0 to 1. Consequently, edge states only appear in the portion of the 1D edge Brillouin zone that is topologically non-trivial. Fig. 4.5 (c) shows the edge spectrum for the PhC with open boundaries along x and periodic boundaries along y. Here we clearly see that the Dirac points separate 1D topologically non-trivial and trivial phases, with and without edge states respectively. This is compatible with the fact that Dirac points are sources of π Berry phase. Hence, the Wilson loop eigenvalue along a closed contour enclosing a single Dirac point is equal to π as shown schematically in Fig. 4.5 (d).

Since the bands 2, 3, and 4 are non-degenerate at HSPs, we can classify them by constructing the 2D indices under TRS from table 4.1, which are respectively $\chi^{(2)}_{\mathcal{T}} = (-1,-1,-1)$, $\chi^{(2)}_{\mathcal{T}} = (0,0,0)$ and $\chi^{(2)}_{\mathcal{T}} = (1,1,1)$. The indices for bands 2 and 4 are not found in table 4.1, and expanding these in a linear combination of OALs results in fractional coefficients $\{\alpha_p\}$. These are therefore stable topological bands and must contain a gapless point somewhere in the BZ under TRS. In this example, we directly see that the PhC has Dirac points located on high-symmetry lines as seen in Fig. 4.5 (a). Band 3 is an example of a situation where stable topological bands could have the same indices as atomic limit bands, in which case additional checks such as computing the Wilson loop are required for a correct identification.

Relevant to PhC design, these invariants can be useful for finding spectrally-isolated Dirac points for applications such as creating cavity states that are algebraically localized to embedded point defects [81–84,137] or enabling large-area single-mode lasing [138,139]. Moreover, once such Dirac points are found, breaking TRS can open a gap at the Dirac points and endow the two bands involved with a non-zero Chern number. Thus, the symmetry-indicator invariants could aid in the discovery and design of topological PhCs, especially in fast random searches that require only looking at eigenmodes at HSPs.

4.4.3 Example 3: Chern insulator in class A

Consider the PhC introduced in the previous section consisting of elliptical discs. We break TRS for this PhC by introducing non-diagonal terms in the permeability tensor which correspond to a response of a gyromagnetic material under a magnetic field applied in the z-direction. This opens bandgaps at the Dirac points, and therefore bands 2, 3,

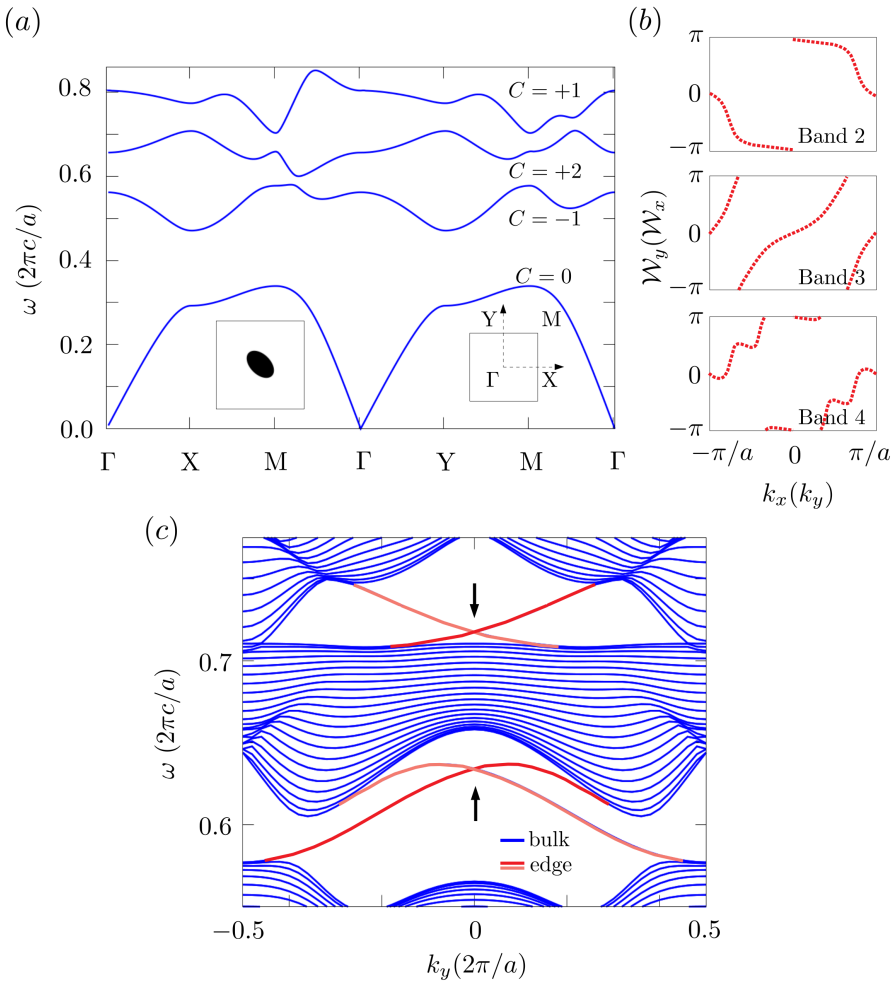

Figure 4.6. (a) TM-polarized band structure of a C_{2v} symmetric gyromagnetic PhC whose unit cell is shown in the inset. The Chern numbers for the first four bands are also shown. (b) Wilson loop eigenvalues $\mathcal{W}_y(\mathcal{W}_x)$ for the bands 2, 3, and 4 plotted as a function of $k_x(k_y)$. The winding of the eigenvalues indicates the non-Wannierizablility of the bands and the winding number is equal to the Chern number of the band. (c) Edge spectrum of this PhC showing chiral edge states (marked with arrows) on the left (red) and right (light red) edges. (d) A schematic of a pair of bands with a non-zero Chern number and the associated chiral edge states.

and 4 are non-degenerate with the invariants $\chi^{(2)} = (-1\,|\,-1,-1,-1)$, $\chi^{(2)} = (+2\,|\,0,0,0)$ and $\chi^{(2)} = (+1\,|\,1,1,1)$ respectively, where the first index is the Chern number. We obtained these Chern numbers by examining the winding number of the Wilson loop eigenvalues shown in 4.6 (b). These plots indicate that bands 2, 3, and 4 have Chern numbers of -1, $+2$, and $+1$, respectively, consistent with the constraints imposed by the symmetry-indicator invariants given in (4.19). The Chern number leads to chiral edge states at the boundary of a finite system as shown in Fig. 4.6 (c). These edge states

exhibit perfect unidirectional transport and have been observed in gyromagnetic PhCs at microwave frequencies [69, 72]. Furthermore, devices with topological slow-light modes that significantly outperform their conventional counterparts in terms of bandwidth have been proposed as an application of such chiral edge states in PhCs [140–142].

4.4.4 Example 4: Fragile phase in class AI

Fragile phases consist of bands that exhibit symmetry-protected non-trivial winding in their Wilson loop spectrum, indicating that these bands are non-Wannierizable. However, when considered as a set along with additional atomic limit bands, the full set becomes Wannierizable, and accordingly, the Wilson loop winding is lost. They are characterized by indices that can be written as a linear combination of the invariants in tables 4.1-4.4 with at least one negative integer coefficient. Alternatively, the coefficients could be all positive integers, in which case the number of bands required to generate the invariant is greater than the number of bands in question.

We now present a novel realization of fragile bands in a PhC with C_{4v} symmetry whose unit cell is shown in the inset of Fig. 4.7 (a). The PhC is made of three materials, $\varepsilon_1 = 1$ (white), $\varepsilon_2 = 16$ (black) and $\varepsilon_3 = 4$ (gray). We consider the two isolated bands, bands $8 + 9$ in the TE-polarized band structure of this PhC shown in Fig. 4.7 (a). Using the little group irreps of the electromagnetic eigenmodes at the HSPs, we compute the invariant for these bands to be $\chi_{\mathcal{T}}^{(4)} = (0, 2, -1)$. Since this invariant is not found in table 4.3, we express it as the following linear combination of OALs from table 4.3: $\chi_{\mathcal{T}}^{(4)} = (0, 2, -1) = (1, 1, -1) + (-1, 1, 0)$. The coefficients in this linear combination, $\{\alpha_p\}$, are positive integers. However, three atomic limit bands are required to give rise to this invariant (two bands are required to generate $(1, 1, -1)$ and one band is required to generate $(-1, 1, 0)$) indicating that this set of two bands is fragile. The non-Wannierizable nature of these bands is also evident from the Wilson loop spectrum in Fig. 4.7 (b) which shows opposite winding of the two eigenvalues.

A different PhC realization of a fragile phase with C_6 symmetry is reported in [97] where TM bands $2 + 3$ are found to be non-Wannierizable but bands $1 + 2 + 3$ have Wannier centers at the $3c$ position of the C_6-symmetric unit cell. The invariant for bands $2 + 3$ is $\chi_{\mathcal{T}}^{(6)} = (-2, 0)$. Similar to the example above, this invariant requires three bands and therefore the set of two bands is fragile. Adding another atomic limit band (from TM band 1) at the $1a$ position with invariant $\chi_{\mathcal{T}}^{(6)} = (0, 0)$ makes the set of three bands Wannierizable with Wannier centers at the $3c$ position of the unit cell.

Such fragile PhCs host corner states resulting from the total corner charge of all

Wannierizable components in their decomposition [114, 143].

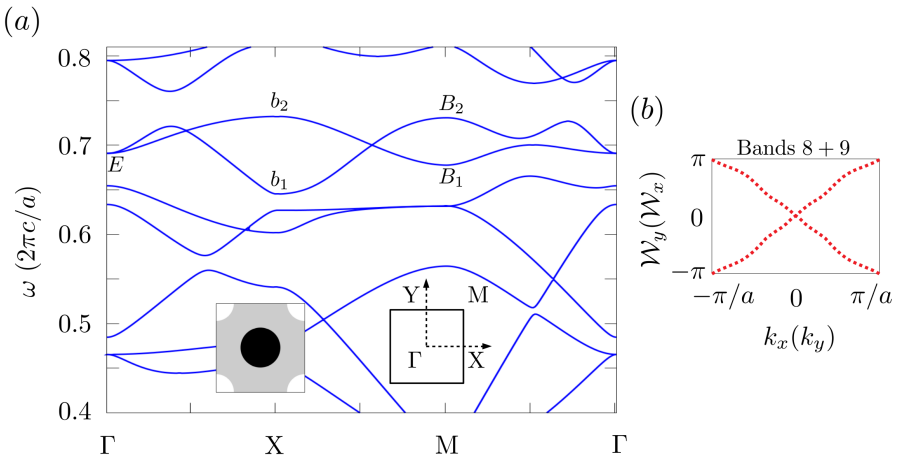

Figure 4.7. (a) TE-polarized band structure of a C_{4v} symmetric PhC with lattice constant, a, whose unit cell is shown in the inset. This unit cell consists of dielectric discs of $\varepsilon_1 = 1$ (white) with $r_1 = 0.2a$ and $\varepsilon_2 = 16$ (black) with $r_2 = 0.225a$ in a background material of $\varepsilon_3 = 4$ (gray). The little group irreps of the electromagnetic eigenmodes at HSPs are shown for bands 8 and 9. (b) Wilson loop eigenvalues $\mathcal{W}_y(\mathcal{W}_x)$ for the bands 8+9, plotted as a function of $k_x(k_y)$. The opposite winding of the eigenvalues indicates the non-Wannierizablility of the bands, particularly that the bands are fragile.

4.5 Other topological phases

We now discuss other topological phases where crystalline symmetries play a crucial role, but whose realization may not be directly inferred from the topological indices presented here. This is because such systems mimic degrees of freedom of spinful systems or are protected by mechanisms beyond bulk-obstructed topological phase transitions, both of which lie outside of the presented classifications.

4.5.1 Quantum spin-Hall analogues

The electronic quantum spin-Hall effect (QSHE) can be thought of as being deformable to two Chern insulators with opposite Chern numbers stacked on top of each other, one for each spin degree of freedom [144–146]. This creates spin-polarized "helical" edge states on the boundary of a finite sample and are protected against back-scattering by Kramers' degeneracy at a time-reversal-invariant momentum point. To construct a PhC realization of the QSHE, a fermionic time-reversal operator is needed that squares to -1, as opposed to the bosonic counterpart for classical electromagnetic waves that

squares to +1. This can be achieved by incorporating spatial symmetries, particularly C_{6v} symmetry, to construct a pseudo-TR operator. It can be shown that the bulk topology of such a PhC is identical to that of the QSHE by explicit calculation of the pseudo-spin polarized Wilson loop spectrum [147], where an opposite winding of the two eigenvalues is observed. However, since this winding is enforced by a crystalline symmetry, it is more appropriate to classify these PhCs as fragile phases than as true QSH systems. Nevertheless, such PhCs have states with a well-defined pseudo-spin, analogous to the spin of electrons [73–77]. A finite system of this kind has pseudo-spin polarized helical edge states, similar to the QSHE, as shown in Fig. 4.8 (a). However, the presence of an edge necessarily breaks the C_{6v} symmetry of the bulk and therefore also the pseudo-TR symmetry allowing for the hybridization of the edge states. This opens a gap in the edge spectrum as shown in Fig. 4.8 (a) and allows for the back-scattering of the edge states.

4.5.2 Valley-Hall phases

As shown previously, Dirac points can be gapped by breaking TRS thereby creating bands with a non-zero Chern number. Breaking inversion symmetry can also gap Dirac points and introduce local Berry curvature with boundary manifestations. Reducing C_{3v} or C_6 symmetry to C_3 gaps the Dirac points that generically exist at the $\mathbf{K}(\mathbf{K}')$ points of the BZ. This causes the Berry curvature to peak at the "valleys" formed at the $\mathbf{K}(\mathbf{K}')$ points. Due to TRS, the total Berry curvature and the Chern number are identically zero. However, the non-zero local Berry curvature at the $\mathbf{K}(\mathbf{K}')$ valleys can be used to define valley Chern numbers such that $C_{\mathbf{K}} = -C_{\mathbf{K}'}$. The bulk-boundary correspondence for such a system is only well-defined at the boundary between two such systems, one spatially inverted with respect to the other. The edge states that thus emerge have a dispersion as shown in Fig. 4.8 (b) and can generally backscatter, unlike the chiral edge states of a Chern insulator. However, it can be shown that certain types of edge geometries and symmetry-preserving perturbations suppress inter-valley scattering, leading to nearly perfect (but incidental) backscatter-free transport [86]. Such edge states have been observed in PhC designs spanning orders of magnitudes in frequency [85–87].

4.5.3 Quadrupole and Octupole topological insulators

Quadrupole and octupole topological insulators (QTIs and OTIs, respectively) are also crystalline symmetry-protected topological phases and host fractional corner charges, similar to OAL insulators [148]. They are $\mathbb{Z}_2$ classified, with fractional charges quantized

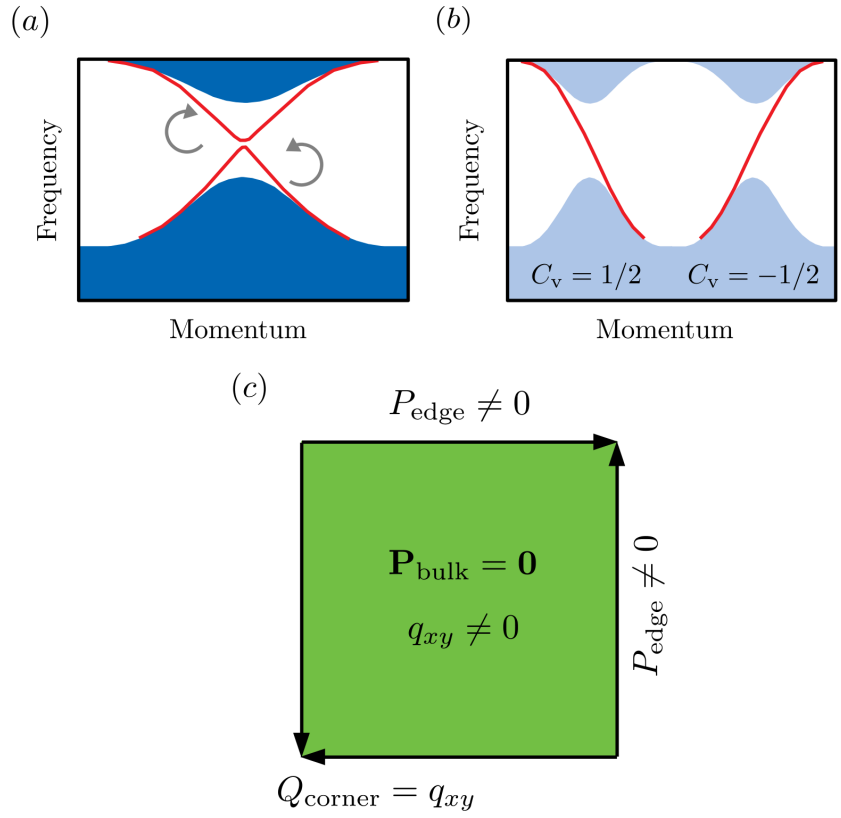

Figure 4.8. (a) Pseudo-spin polarized helical edge states of a quantum spin-Hall analog PhC. (b) Edge states of a valley-Hall PhC. (c) Schematic of a PhC quadrupole insulator with vanishing bulk dipole moment and non-zero bulk quadrupole moment.

to 1/2 (0) mod 1 in the topological (trivial) phases. The prototypical model is C_{4v} symmetric [149]. Under C_4 symmetry, the QTI phase is bulk-obstructed and therefore an atomic limit. However, relaxing C_{4v} down to only reflection symmetries also protects the quantization of corner charge, although their symmetry-indicator invariants due to reflection symmetry vanish. Thus, the protection due to reflection symmetries is more subtle than for OALs; they exhibit a gapped Wilson loop spectrum, not pinned by symmetries, and the change in topology here is accompanied by a gap closing in the Wilson loop spectrum, which implies a gap closing at the edges of the sample, instead of in the bulk spectrum.

QTI and OTI phases require a set of anti-commuting spatial symmetries that can be achieved by threading a π-flux in simple tight-binding models. However, PhCs cannot be accurately described by such models and instead a quadrupole phase can be achieved by breaking time-reversal symmetry while preserving the product of mirror and time-reversal symmetries [94]. Alternatively, QTI phases can also be realized in PhCs

with anti-commuting glide symmetries [95]. Topological indices that diagnose the QTI and OTI topologies have been recently demonstrated [150, 151], and follow the natural extension of the index for dipole moments [152]. They have recently been used to show that QTIs are also protected solely by chiral symmetry [153–155], which has led to the discovery of a $\mathbb{Z}$ classification of higher-order topological insulators in 2D and 3D [156].

4.6 Discussion

In solids, the atomic ions form potentials that bind electronic orbitals. The electrons in the crystal hop between these orbitals, giving rise to energy bands that can often be accounted for by simplified tight-binding models, where the hopping terms in the Hamiltonian are given by the overlap integrals between different orbitals. Photonic analogs of solid-state lattices have been achieved in periodic arrays of coupled waveguide, where each waveguide supports a guided mode so that the extended array can be thought of as having inter-orbital hoppings that also lead to tight-binding descriptions [157]. As a result, the electronic theory of non-interacting topological phases carries over directly to this case. In contrast, the PhCs studied in this work are not well-described by simple tight-binding models.

In the past several years, topological phenomena of various types have been found in PhCs [60–62, 68], validating the notion that topological band theory is a wave phenomenon and transcends the existence of bound orbital states present in electronic systems. Motivated by these recent developments, we have rigorously extended the use of symmetry-indicator invariants to classify one- and two- dimensional PhCs with crystalline symmetries, with and without time-reversal symmetry. Through various examples, we have also demonstrated that the bulk-boundary correspondence of topological band theory carries over to these systems as well.

A further crucial difference between PhCs and solids is that PhCs host classical waves as opposed to electrons, which are fermions. For topological band theory, this has two consequences. First, there is no Kramers' degeneracy for electromagnetic waves, and thus there is no protection of helical edge states as in the QSHE phase of electronic systems. As discussed in Section V, the edge states in the PhC versions of the QSHE phase are not protected in the strictest sense. Second, there is a lack of a notion of filling of bands and a more subtle notion of a filling anomaly in PhCs, the latter of which results in the fractional quantization in the local density of states, as opposed to charges [129]. We have demonstrated that such fractionalization comes from a *counting*

mismatch of states (closely related to the filling anomaly in fermionic systems), and that the boundary-localized states associated with it are the consequence of the conservation of the number of degrees of freedom in the system, and do not require a Fermi level. We have further demonstrated how the topological invariants based on symmetry indicators relate to the presence of counting mismatches and their boundary states. Finally, we have also presented a novel realization of fragile bands in a PhC with C_{4v} symmetry.

Besides being an excellent platform for exploring the novel physics of topological materials, we believe that topological phenomena in PhCs will lead to novel technologies and design strategies. We expect that the algebraic structure of the classification presented here would be useful in this domain.

Chapter 5
Polarization in Chern insulators

Chern insulators are topologically characterized by Chern numbers that present an obstruction to the construction of exponentially-localized Wannier functions and, as a result, electric polarization is believed to be ill-defined in Chern insulators [158]. In this chapter, we show that electronic boundary charges and currents can exist in Chern insulators that are accounted for by a notion of relative polarization. We show further that this relative polarization can be quantized in the presence of inversion symmetry, leading to weak topological phases, similar to those in conventional insulators. A consequence of this is the fractional quantization of charge along with concomitant topological states. This chapter is based on work that was done in collaboration with Mikael C. Rechtsman and Wladimir A. Benalcazar.

5.1 Introduction

In conventional insulators, the electric polarization $\mathbf{P}$ can be formulated in terms of Berry phases along the non-contractible loops of the Brillouin zone or equivalently in terms of the positions of the exponentially-localized Wannier functions, so-called Wannier centers, of occupied bands [5]. In 2D crystalline insulators, the polarization $\mathbf{P} = P_1\mathbf{a}_1 + P_2\mathbf{a}_2$, where $\mathbf{a}_{i=1,2}$ are primitive lattice vectors, has components $P_i = \frac{1}{2\pi}\oint \mathrm{d}^2\mathbf{k}\mathrm{Tr}[\mathcal{A}_i(\mathbf{k})]$, which can be written as

$$P_i = \oint \mathrm{d}k_j p_i(k_j), \tag{5.1}$$

$$p_i(k_j) = \oint \mathrm{d}k_i \mathrm{Tr}[\mathcal{A}_i(\mathbf{k})] \bmod 1 \tag{5.2}$$

for $i, j = 1, 2$; $i \neq j$, and where $\mathcal{A}_i$ is the Berry connection with elements $[\mathcal{A}_i(\mathbf{k})]_{m,n} = -i\langle u_m(\mathbf{k})|\partial_{k_i}|u_n(\mathbf{k})\rangle$ and $|u_m(\mathbf{k})\rangle$ is the Bloch eigenstate of occupied band m.

In Chern insulators, $p_i(k_j)$ winds around the 1D Brillouin zone formed by $k_j \in [-\pi/a_j, \pi/a_j)$. This winding simultaneously reflects the difficulty in building exponentially-localized Wannier functions and defining polarization in Eq. 5.1, as its value depends on the starting point in the loop integral along k_j. Furthermore in Chern insulators, the existence of chiral edge states that cross the Fermi level also complicates establishing the bulk-boundary correspondence to polarization because the boundary charge gets affected by the partial occupation of its chiral edge states [159]. As such, whether the polarization in Chern insulators is a meaningful quantity has remained elusive in topological band theory.

In this chapter, we show that Chern insulators can exhibit boundary charges and currents that can be accounted for by a notion of relative polarization. In the presence of crystalline symmetries, the boundary charge is quantized similar to conventional insulators. We generalize this principle and show that, similarly, corner charges and states akin to those arising from higher-order topology are possible within Chern insulators. Our central argument is based on the observation that boundaries do not respond to the polarization of a bulk, but rather, to the difference in polarization across the two domains separated by the boundary. In the case of polarization, the only meaningful bulk-boundary correspondence at a boundary that separates regions r_1 and r_2 perpendicular to $\hat{\mathbf{n}}$ is the existence of boundary charge σ given by

$$\sigma = \left(\mathbf{P}^{(1)} - \mathbf{P}^{(2)}\right) \cdot \hat{\mathbf{n}} \mod 1, \tag{5.3}$$

where we have set the unit cell lengths at all directions and regions to 1 for simplicity. If for regions r_1 and r_2 we have $C_1 \neq C_2$, n chiral edge states will appear at their common boundary, with $n = |C_1 - C_2|$. This, in conjunction with the winding of $p_i(k_j)$, makes the definition of the polarization problematic. Coh and Vanderbilt studied how a definition of the polarization might be saved in the case $C_1 = 1$, $C_2 = 0$, but only with a knowledge of the wave vector at which the occupancy of the edge state is discontinuous [159]. We instead consider the case in which $C_1 = C_2$ but nevertheless regions r_1 and r_2 belong to different domains. To clearly present our case, we make use of additional crystalline symmetries to force the two domains to belong to different symmetry-protected weak topological phases. Imposing these crystalline symmetries not only facilitates our argument, but also fractionally quantizes the response to polarization. The two domains we choose are such that $C_1 = C_2$ and the difference $p_i^{(1)}(k_j) - p_i^{(2)}(k_j)$ does not wind, even though $p_i^{(\alpha)}(k_j)$, for $\alpha = 1, 2$, individually do. This property enables

a well-defined bulk-boundary correspondence that probes the difference in polarization at the boundary between r_1 and r_2. Similarly, we show the presence of an adiabatic current when one domain is adiabatically varied with respect to the other domain such that the relative polarization changes. This demonstrates that a well-defined, observable response to polarization can exist in systems without a Wannier representation, deeming the bulk polarization as the fundamental physical quantity regardless of whether a Wannier representation is possible, and thereby displacing the existence of a Wannier representation as a sufficient, but not necessary, criterion for bulk polarization, adiabatic current, and boundary charge.

5.2 Results

5.2.1 Tight-binding model

We consider a tight-binding model of a Chern insulator described by the following generalized Qi-Wu-Zhang (QWZ) Hamiltonian

$$h_{\mathrm{QWZ}}(\mathbf{k},\theta) = \sin k_x \sigma_x + \sin(k_y+\theta)\sigma_y + [m + \cos k_x + \cos(k_y+\theta)]\sigma_z, \tag{5.4}$$

where $\mathbf{k} = (k_x, k_y)$ is the crystal momentum, $\sigma_{x,y,z}$ are the Pauli matrices and m is a mass term. For $\theta^* = 0$ and π, this Hamiltonian possesses inversion symmetry, $\mathcal{I}h(\mathbf{k},\theta^*)\mathcal{I} = h(-\mathbf{k},\theta^*)$, with $\mathcal{I} = \sigma_z$, as well as particle-hole symmetry $\Xi h(\mathbf{k},\theta^*)\Xi^{-1} = -h(-\mathbf{k},\theta^*)$ with $\Xi = i\sigma_y\mathcal{K}$ ($\mathcal{K}$ is complex-conjugation). m governs the value of the Chern number (C) of the two bands of this model. Specifically, for the lowest band, $C = 1$ for $0 < m < 2$, $C = -1$ for $-2 < m < 0$, and $C = 0$ otherwise. The plots of $p_x(k_y)$ for $m = 0.25$ and for $\theta = 0$ and π are shown in Fig. 5.1 (a) and (b), respectively.

Under open boundary conditions along one direction, i.e., with vacuum on the exterior, the systems with $\theta = 0$ and π host chiral edge states as shown in Fig. 5.1 (d) and (e). However, due to the relative momentum-space shift between these models introduced by θ, the chiral edge states cross the gap in different portions of the edge Brillouin zone.

5.2.2 Boundary charge and charge pumping

Next, we consider the boundary between two regions, r_1 and r_2 with Bloch Hamiltonians $h_{r_1}(\mathbf{k}) = h_{\mathrm{QWZ}}(\mathbf{k},0)$ and $h_{r_2}(\mathbf{k}) = h_{\mathrm{QWZ}}(\mathbf{k},\pi)$. We observe that h_{r_1} and h_{r_2} have distinct windings in $p_i(k_j)$ such that $\oint \mathrm{d}k_i \Delta p_i(k_j) = \oint \mathrm{d}k_i [p_i^{(1)}(k_j) - p_i^{(2)}(k_j)] = \pi$, as shown in

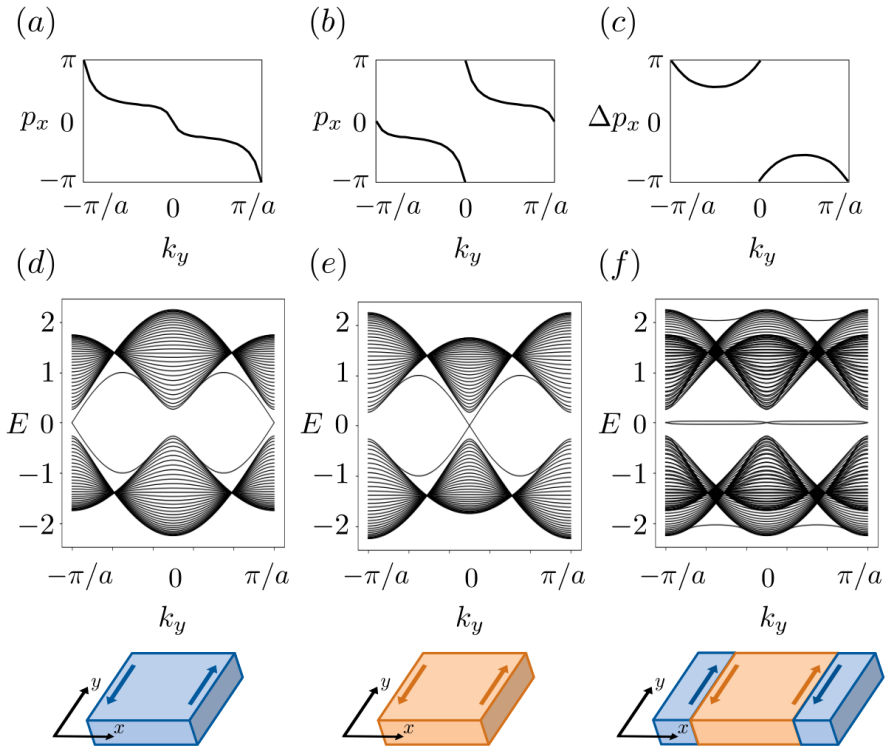

Figure 5.1. (a), (b) $p_x(k_y)$ for the occupied band of $h_{\mathrm{QWZ}}(\mathbf{k}, 0)$ and $h_{\mathrm{QWZ}}(\mathbf{k}, \pi)$ respectively, for m = 0.25. (c) $\Delta p_x(k_y)$ for $h_{\mathrm{QWZ}}(\mathbf{k}, 0)$ and $h_{\mathrm{QWZ}}(\mathbf{k}, \pi)$. (d), (e) Edge spectrum for $h_{\mathrm{QWZ}}(\mathbf{k}, 0)$ and $h_{\mathrm{QWZ}}(\mathbf{k}, \pi)$ respectively, with open boundaries as depicted in the bottom panel. (f) Edge spectrum for an inversion-symmetric configuration consisting of two domains described by $h_{\mathrm{QWZ}}(\mathbf{k}, 0)$ and $h_{\mathrm{QWZ}}(\mathbf{k}, \pi)$.

Fig. 5.1 (c). Now let us consider a finite inversion-symmetric composite system that consists of the two domains described by h_{r_1} and h_{r_2} as shown in orange and blue in the schematic at the bottom of Fig. 5.1 (f). In this case, the hybridization of chiral edge states of the two Chern insulators leads to the formation of bi-directional in-gap edge states. As a result of this and the presence of inversion symmetry, quantized fractional charges appear at each of the two boundaries at exactly half filling[1], as shown in Fig. 5.2 (a).

The prescription above for determining the accumulation of boundary charge due to polarization in Chern insulators also serves as a platform to probe adiabatic currents. Since a Wannier center picture is not possible, the bulk currents are difficult to examine directly. However, we can show the existence of these bulk currents indirectly, via their effects on the boundary charges. To this end, we consider adiabatically evolving the domain r_2 in Fig. 5.1 (f), with respect to the parameter θ, i.e. $h_{r_2}(\mathbf{k}, \theta) = h_{\mathrm{QWZ}}(\mathbf{k}, \theta)$

[1]Inversion symmetry was infinitesimally broken to slightly lift the degeneracy between edge states

for $\theta \in [0, 2\pi)$, while keeping r_1 constant, i.e., $h_{r_1}(\mathbf{k}) = h_{\mathrm{QWZ}}(\mathbf{k}, 0)$. The two domains remain gapped in the bulk for the full cycle of the adiabatic parameter. In Fig. 5.2 (b), we plot the boundary charges as a function of θ, where we clearly observe the pumping of charges from one boundary of the system to the other boundary, as a result of adiabatic currents in the bulk. The formation of adiabatic currents in the bulk can be attributed to a change in the relative polarization between the two domains, leading to a measurable response at their boundary.

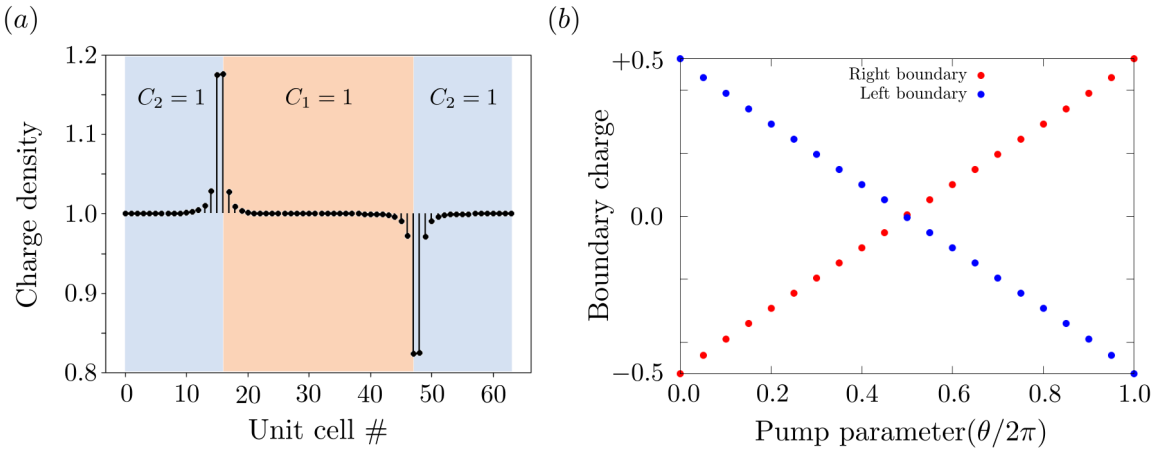

Figure 5.2. (a) Fractionalization of boundary charge at half filling in the system shown in Fig. 5.1 (f). Under inversion symmetry, these boundary charges are quantized to ± 0.5. (b) The change in the left and right boundary charges due to charge pumping as a function of the adiabatic parameter θ. The system has inversion symmetry at $\theta = 0$ and π.

5.2.3 Topological aspects and symmetry indicators

We next turn to a description of inversion-symmetric Chern insulators and atomic limits using a symmetry-indicator approach, similar to that developed in the previous chapter. Bands in class A under inversion symmetry are classified by a set of indices given by

$$\chi = \Big(C \,\Big|\, [X], [Y], [M] \Big) \tag{5.5}$$

where C is the Chern number, the symmetry indicators $[\Pi]$ are defined as $[\Pi] \equiv \#\mathbf{\Pi} - \#\mathbf{\Gamma}$ where $\#\mathbf{\Pi}$ is the number of states in the set of bands under consideration with inversion eigenvalue $+1$, at the high-symmetry point (HSP) $\mathbf{\Pi}$. When $C = 0$, polarization can be

calculated as follows

$$\mathbf{P} = \frac{1}{2}\left([Y] + [M]\right)\mathbf{a_1} + \frac{1}{2}\left([X] + [M]\right)\mathbf{a_2}, \tag{5.6}$$

where $\mathbf{a_1}$ and $\mathbf{a_2}$ are the primitive lattice vectors. Additionally, some indices can lead to higher-order topological corner states determined by the corner charge

$$Q_{\text{corner}} = \frac{1}{4}\left(-[X] - [Y] + [M]\right) \tag{5.7}$$

Both $\mathbf{P}$ are Q_{corner} are defined modulo a unit electronic charge.

For two Chern insulators described by indices χ_1, χ_2 but with the same Chern number $C_1 = C_2 = C$, the difference index, $\Delta\chi = \chi_2 - \chi_1$, defined as

$$\Delta\chi = \left(0 \,\middle|\, [X]_2 - [X]_1, [Y]_2 - [Y]_1, [M]_2 - [M]_1\right), \tag{5.8}$$

has a vanishing Chern component and therefore describes either an atomic limit or a fragile phase. As a result, while $\mathbf{P}$ and Q_{corner} are ill-defined for χ_1 and χ_2 individually, the relative polarization, $\Delta\mathbf{P}$, and relative corner charge, ΔQ_{corner}, can be defined using $\Delta\chi$ as

$$\Delta\mathbf{P} = \frac{1}{2}\left([Y]_2 - [Y]_1 + [M]_2 - [M]_1\right)\mathbf{a_1} + \frac{1}{2}\left([X]_2 - [X]_1 + [M]_2 - [M]_1\right)\mathbf{a_2}, \tag{5.9}$$

$$\Delta Q_{\text{corner}} = \frac{1}{4}\left[-([X]_2 - [X]_1) - ([Y]_2 - [Y]_1) + ([M]_2 - [M]_1)\right]. \tag{5.10}$$

Consequently, edge and corner states would be expected to appear at the boundary between the Chern insulators described by χ_1 and χ_2 when $\Delta\mathbf{P}$ and ΔQ_{corner} are non-zero. In the previous sections, we have already seen the appearance of such polarization-induced edge states in the tight-binding model. We now demonstrate the the presence of these edge states and corner states in experimentally realizable gyro-magnetic Chern photonic crystals (PhCs).

5.2.4 Photonic crystal example

The unit cells of the proposed inversion-symmetric, two-dimensional PhCs are shown in the inset of Fig. 5.3 (a), each of which consist of two dielectric discs made out of Yttrium-Iron-Garnet (YIG), a strong magneto-optical material at microwave frequencies. These two unit cells are related by a half-lattice-constant shift in both x and y directions and

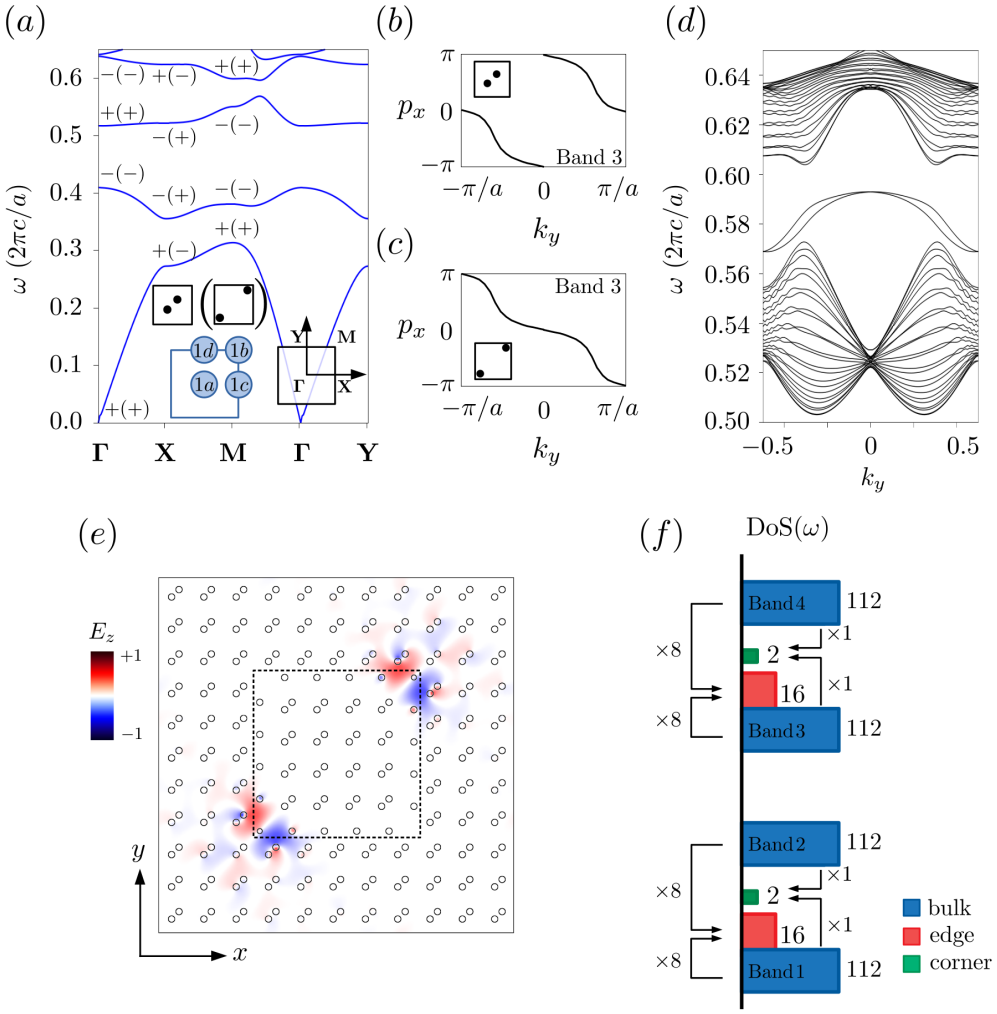

Figure 5.3. (a) The TM band structure of the PhCs with contracted and expanded unit cell types shown in the inset. The high-symmetry points are labelled by inversion eigenvalues for both unit cell types. The inset also shows the maximal Wyckoff positions for inversion-symmetric unit cells. (b) $p_x(k_y)$ for band 3 for the contracted and (c) expanded unit cell. (d) The edge spectrum of a composite inversion-symmetric system made of the two types of unit cells in a strip geometry showing the presence of bi-directional edge states. (e) The E_z mode profile of the corner states and dielectric profile of a finite system made of the two unit cell types in a core-cladding configuration. The corner states shown here originate from the Chern bands with their frequency lying inside the bandgap between bands 3 and 4. (f) A schematic of the photonic density of states for bands 1 to 4 for the finite system in (e) with 11×11 unit cells.

we refer to them as "contracted" and "expanded". On breaking time-reversal symmetry, TM band 3 acquires a Chern number of +1 for PhCs with either unit cell type, as can be seen from the windings in $p_x(k_y)$ shown in Fig. 5.3 (b) and (c). The relative shift in the windings of $p_x(k_y)$ for the two unit cell types is similar to the shift previously seen in

the QWZ Hamiltonians with $\theta = 0$ and π in Fig. 5.1 (a) and (b).

Using the inversion eigenvalues at HSPs for contracted and expanded unit cell types, we now calculate the χ indices, $\Delta\chi$, $\Delta\mathbf{P}$ and ΔQ_{corner} for first four TM bands in the table 5.1.

Band #	χ_2 (Contracted)	χ_1 (Expanded)	$\Delta\chi = \chi_2 - \chi_1$	$\Delta\mathbf{P}(\Delta\chi)$	$\Delta Q_{\text{c}}(\Delta\chi)$
Band 1	$(0 \,\vert\, 0,0,0)$	$(0 \,\vert\, -1,-1,0)$	$(0 \,\vert\, 1,1,0)$	$1/2(\mathbf{a_1}+\mathbf{a_2})$	$1/2$
Band 2	$(0 \,\vert\, 0,0,0)$	$(0 \,\vert\, 1,1,0)$	$(0 \,\vert\, -1,-1,0)$	$1/2(\mathbf{a_1}+\mathbf{a_2})$	$1/2$
Band 3	$(1 \,\vert\, -1,-1,-1)$	$(1 \,\vert\, 0,0,-1)$	$(0 \,\vert\, -1,-1,0)$	$1/2(\mathbf{a_1}+\mathbf{a_2})$	$1/2$
Band 4	$(1 \,\vert\, 1,1,1)$	$(1 \,\vert\, 0,0,1)$	$(0 \,\vert\, 1,1,0)$	$1/2(\mathbf{a_1}+\mathbf{a_2})$	$1/2$

Table 5.1. χ indices, $\Delta\chi$, $\Delta\mathbf{P}$ and ΔQ_{corner} for first four TM bands of the PhCs with the contracted and expanded unit cell typees.

From this analysis, we see that Bands 1 and 2 are atomic limit bands with Wannier centers at the $1a$ position for the contracted unit cell, and at the $1b$ position for the expanded unit cell.[2] Bands 3 and 4 are Chern bands that do not have Wannier centers but nevertheless have a non-zero relative polarization and corner charge between the two unit cell types.

To explore the bulk-boundary correspondence of relative polarization and corner charge, we first simulate a finite system consisting of an inner domain with the expanded unit cell and an outer domain consisting of the contracted unit cell in a "strip geometry" similar to the schematic in Fig. 5.1 (f). In Fig. 5.3 (d), we observe that the edge spectrum contains bi-directional edge states similar to those found in the tight-binding model in Fig. 5.1 (f). Next, we simulate a finite system in a "core-cladding" type of geometry and find corner states as shown in Fig. 5.3 (e). Using a counting mismatch argument that we developed in the previous chapter, we show that the edge and corner states originate from multiple bands, suggesting a phenomenon analogous to the pairing of Wannier centers due to a filling anomaly in obstructed atomic limits. The state counting and a schematic of the photonic density of states (DoS) for the first four TM bands is shown in Fig. 5.3 (f). We see here that the state counting for both edge and corner states is identical for the obstructed atomic limit bands (bands 1 and 2), and Chern bands (bands 3 and 4), due to the identical values of $\Delta\mathbf{P}$ and ΔQ_{corner} that they possess.

Along with the quantization of boundary charge and existence of adiabatic current in the tight-binding model, the edge and corner states in the Chern PhCs demonstrate that

[2]For Wyckoff positions, see inset of Fig. 5.3 (a)

a notion of a relative polarization is indeed well-defined for the Chern bands and the bulk-boundary correspondence operates similarly to that in obstructed atomic limits.

5.3 Conclusion

In this chapter, we have proposed that a well-defined, observable response to polarization can exist in systems without a Wannier representation, particularly in Chern insulators. We have demonstrated the consequences of this, i.e., quantization of boundary charges under inversion symmetry, and the presence of adiabatic currents, using a tight-binding model. We have further demonstrated the existence of a bulk-boundary correspondence resulting in edge and corner states in Chern photonic crystals that could lead to an experimental realization of this phenomenon.

Chapter 6
Point-defect-localized bound states in the continuum

In this chapter, we show that point defects in two-dimensional photonic crystals can support bound states in the continuum (BICs). The mechanism of confinement is a symmetry mismatch between the defect mode and the Bloch modes of the photonic crystal. These BICs occur in the absence of bandgaps and therefore provide an alternative mechanism to confine light. Furthermore, we show that such BICs can propagate in a fiber geometry and exhibit arbitrarily small group velocity which could serve as a platform for enhancing non-linear effects and light-matter interactions in structured fibers. This chapter is based on work that was done in collaboration with Wladimir A. Benalcazar, Alexander Cerjan and Mikael C. Rechtsman [137].

6.1 Overview

Over the last three decades, photonic crystals (PhCs) have been shown to exhibit exceptional confinement and transport properties that exploit the existence of a photonic bandgap, a band of frequencies where no electromagnetic waves may propagate [3, 4, 160, 161]. Photonic bandgaps can inhibit spontaneous emission of embedded quantum emitters [162–165], facilitate slow-light through band-edge operation [166] or host localized defect modes that can serve as high-Q resonators or waveguides. Confined defect modes form the basis of many devices such as PhC fibers [167, 168], spectral filters, and lasers [169, 170] and to achieve near-perfect confinement, defect modes are constructed to lie within photonic bandgaps so as to spectrally isolate them from the extended states of the PhC. However, this necessitates the use of materials with a sufficiently high refractive index to open complete gaps. An alternative mechanism for confinement

could circumvent the need for bandgaps, enabling the use of many low-refractive index materials such as glasses and polymers as well as increasing design flexibility for the realization of PhC-based devices.

One possible way to achieve this is by using bound states in the continuum (BICs). BICs are eigenmodes of a system that, despite being degenerate with a continuum of extended states, stay confined – this confinement may result from a variety of mechanisms [171]. For example, modes of a PhC slab that lie above the light line of vacuum and therefore could radiate, can remain perfectly bound to the slab due to symmetry mismatch or due to topological vortices in the far-field radiation [172–177]. Previous designs with BICs have mostly shown confinement of a mode in one dimension lower than that of the environment. Recently, corner-localized BICs were predicted and observed in two-dimensional chiral-symmetric systems with higher-order topology [178, 179]. However, chiral (sub-lattice) symmetry is, in general, strongly broken in all-dielectric PhCs. Indeed, confinement in the continuum has to this point not yet been achieved in point defects embedded inside multi-dimensional PhCs.

In this chapter, we predict the existence of BICs that are exponentially confined to point defects in a two-dimensional PhC environment. The defect cavity and bulk PhC are designed such that radiation leakage is prohibited due to a symmetry mismatch between the defect mode and the ambient continuum states. The BICs proposed here are protected by the simultaneous presence of time-reversal symmetry (TRS) and the point group of the lattice and as such are robust as long as these symmetries are maintained. As an application for these BICs, we also show how they can circumvent bandgap requirements and be used as propagating fiber modes with arbitrarily small group velocity in a low-contrast slow-light PhC fiber.

We draw a distinction between our BICs and the previously reported defect modes degenerate with Dirac points in 2D PhC [82–84, 180–182]. In the latter case, the confinement of light to a defect site is due to a vanishing density of states at the Dirac point, which is where that confined mode's frequency lies. Characteristically, such defect modes exhibit weak confinement due to the algebraic mode profile away from the defect site. In contrast, the defect modes presented here are bona fide symmetry protected BICs that are exponentially localized to the defect site.

6.2 Results

6.2.1 Two-dimensional photonic crystals with spectrally-isolated two-fold degeneracies

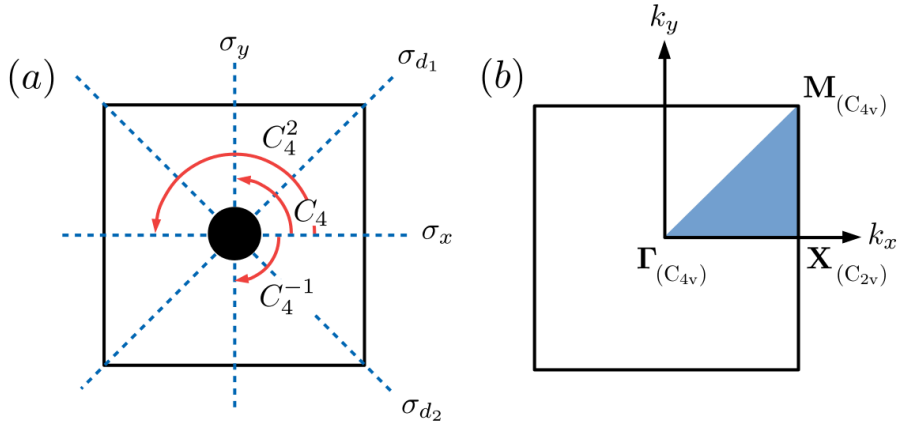

Figure 6.1. (a) The unit cell of a two-dimensional PhC consisting of circular discs. The symmetry operators of the C_{4v} point group are labelled. (b) The Brillouin zone of the PhC showing its HSPs and the little groups under which the HSPs are invariant. The solid color consists of all momenta that lie within the irreducible Brillouin zone.

Consider a two-dimensional PhC consisting of a square lattice of discs with dielectric constant ε and radius r embedded in vacuum. This PhC, as shown in Fig. 6.1 (a) is invariant under 90° rotations (C_4, C_4^2, C_4^{-1}), and reflections along the x, y axes and two diagonals (σ_x, σ_y, σ_{d_1}, σ_{d_2}). These symmetry operations constitute the C_{4v} point group. The irreducible Brillouin zone of this lattice contains three inequivalent high symmetry points (HSPs), namely, $\mathbf{\Gamma} = (0, 0)$, $\mathbf{X} = (\pi/a, 0)$ and $\mathbf{M} = (\pi/a, \pi/a)$, as shown in Fig. 6.1 (b). The HSPs $\mathbf{\Gamma}$ and $\mathbf{M}$ are invariant under the full C_{4v} group, while $\mathbf{X}$ is invariant only under the little group, C_{2v}. Eigenmodes of the PhC at a HSP transform according to the irreducible symmetry representations (irrep) of the group under which the HSP is invariant. The $\mathbf{X}$ point has four possible one-dimensional irreps (a_1, a_2, b_1, b_2) with character table as shown in Table 6.1. Similarly, the $\mathbf{\Gamma}$ and $\mathbf{M}$ points have four one-dimensional irreps (A_1, A_2, B_1, B_2) and one two-dimensional irrep (E) with character table as shown in Table 6.2 [4]. The eigenmodes of a C_{4v} symmetric PhC that transform according to the two-dimensional irrep (E) of the C_{4v} point group, commonly manifest as quadratic two-fold degeneracies at $\mathbf{\Gamma}$ and $\mathbf{M}$ in the presence of TRS. When C_{4v} is broken, this degeneracy splits into two Dirac points as long as inversion and TRS are retained. However, breaking TRS can lift the degeneracy completely [183].

C_{2v}	I	C_2	σ_x	σ_y
a_1	1	1	1	1
a_2	1	1	-1	-1
b_1	1	-1	1	-1
b_2	1	-1	-1	1

Table 6.1. Character table for the C_{2v} point group.

C_{4v}	I	$2C_4$	C_2	$2\sigma_{x,y}$	$2\sigma_{d_1,d_2}$
A_1	1	1	1	1	1
A_2	1	1	1	-1	-1
B_1	1	-1	1	1	-1
B_2	1	-1	1	-1	1
E	2	0	-2	0	0

Table 6.2. Character table for the C_{4v} point group.

We now describe the general mechanism for creating defect-localized BICs. By changing the geometric parameters of the lattice, the band dispersion of a C_{4v} and TRS-symmetric PhC can be designed such that the two-fold degeneracy at either $\mathbf{\Gamma}$ or $\mathbf{M}$ is spectrally isolated from other bands. In a large system consisting of many unit cells of such a PhC (a supercell), a single defect site with radius $r_d \neq r$ is introduced at the center. This creates modes with a significant support on the defect site that generally radiate by hybridizing with the bulk states of the PhC, forming leaky resonances that are characterized by a complex frequency with a negative imaginary part. The frequency of such modes can be tuned by changing the parameters of the defect site such as size or dielectric constant. When the real part of the frequency of the defect mode exactly matches that of the spectrally-isolated two-fold degeneracy of the bulk, it becomes a perfectly confined BIC provided that the defect mode transforms according to a one-dimensional irrep that is orthogonal to the two-dimensional irrep of the bulk. The presence of this BIC can be inferred from the vanishing of the imaginary part of the frequency and hence a diverging quality factor, $Q = -\mathrm{Re}(\omega)/2\mathrm{Im}(\omega)$, of the defect mode.

6.2.2 FDTD simulations

To demonstrate this, we simulate this system using finite-difference time domain method (FDTD) as implemented in MEEP [1]. The bulk band requirements are easily met in

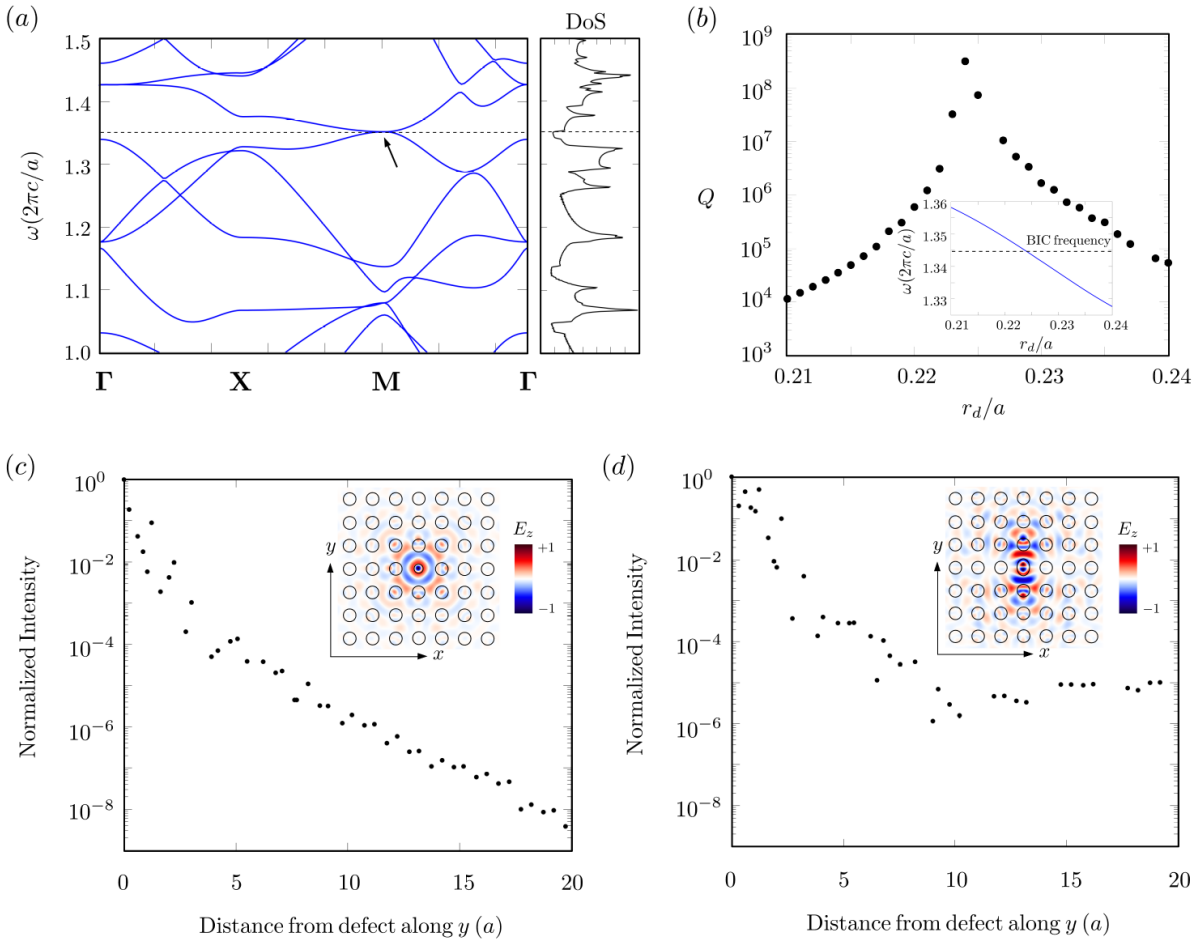

Figure 6.2. (a) The TM bands and photonic DoS of a square lattice of dielectric discs of $\varepsilon = 4$ and $r/a = 0.275$ calculated using MPB [2]. The spectrally-isolated two-fold degeneracy is marked with an arrow. (b) Quality factor (Q) of the defect mode as a function of defect radius (r_d). The sharp divergence in Q indicates the existence of a BIC at $r_d/a = 0.224$. The inset shows the dependence of the defect mode frequency on r_d. (c) The **E**-field intensity envelope of the BIC showing exponential localization as a function of distance (along the y-axis) from the defect site. The inset shows the z-component of the **E**-field of the BIC, extracted from FDTD simulations. (d) The **E**-field intensity envelope of the resonance when the symmetry of the supercell is reduced from C_{4v} to C_{2v}. The inset shows the z-component of the **E**-field of the resonance, extracted from FDTD simulations.

a simple square lattice of discs with dielectric constant $\varepsilon = 4$ and radius $r/a = 0.275$, where a is the lattice constant in both x- and y-directions. The chosen values of ε and r/a allow the spectrally-isolated two-fold degeneracy to occur between TM bands 10 and 11 at the **M** point as shown in Fig. 6.2 (a). The photonic density of states (DoS), also shown in the same figure, is given by $\mathrm{DoS}(\omega) = \sum_n \int_{\mathbf{k}\in\mathrm{BZ}} \delta[\omega - \omega_n(\mathbf{k})]\mathrm{d}\mathbf{k}$, where $\omega_n(\mathbf{k})$ is the frequency eigenvalue at the momentum $\mathbf{k}$ and band index n. Since each band

undergoes an extremum at the degeneracy, the DoS exhibits a jump-discontinuity-type Van Hove singularity between two finite and non-zero values. The non-vanishing set of states at the degeneracy forms the continuum within which a BIC can be created.

In a large supercell, we now introduce a defect by changing the radius ($r_d \neq r$) of a single disc in the center of the supercell. As we scan the values of r_d, a BIC emerges for the specific value of the defect radius that corresponds to a mode with the exact frequency of the bulk degeneracy. This is seen from the sharp divergence of the Q-factor of the defect mode as shown in Fig. 6.2 (b). Examining the mode profile shown in the inset of Fig. 6.2 (c) reveals that the defect mode transforms according to the irrep A_1 which is prevented from mixing with the basis modes of the orthogonal two-dimensional irrep, E, of the bulk. Moreover, the mode shows very strong exponential localization to the defect site which can be seen by plotting the intensity envelope as shown in Fig. 6.2 (c). Another important feature of this BIC is its occurrence above $\omega a/2\pi c = 1$. This implies that the lattice constant of the bulk PhC is larger than the wavelength of the BIC mode, a property which could prove useful for fabrication, because features sizes would need not be subwavelength.

To conclusively show that this BIC is indeed symmetry protected, we change the defect site from a disc to a filled ellipse, which reduces the symmetry of the supercell from C_{4v} to C_{2v}. Due to this deformation, the degeneracy between the two modes that formed the two-dimensional irrep, E, of C_{4v} is very slightly lifted and the resultant non-degenerate modes have the one-dimensional irreps b_1 and b_2 of C_{2v}. This symmetry breaking is achieved by changing the defect site from a circular disc to an elliptical disc with semi-major and semi-minor axes lengths of $0.53a \times t_d$ and $0.4a \times t_d$ respectively where a is the lattice constant and t_d is a tuning parameter which is varied. Fig. 6.3 shows a comparison of quality factors of the defect mode for the two cases and clearly shows the lack of divergence of Q in the C_{2v} symmetric supercell, indicating that the defect mode is not a BIC but a resonance.

Indeed, the field pattern of the defect mode as shown in the inset of Fig. 6.2 (d), transforms according to b_2, which coincides with one of the irreps of the bulk enabling the defect and bulk modes to couple and create a leaky resonance with a finite Q. This is also evident from the intensity envelope of the resonance as shown in Fig. 6.2 (d) that markedly demonstrates the lack of exponential confinement to the defect site.

To further assess the impact of symmetry breaking due to fabrication imperfections, we consider the same 2D PhC system as discussed in Fig. 6.2. We then calculate the Q-factor of the defect mode from FDTD simulations where the defect site is displaced

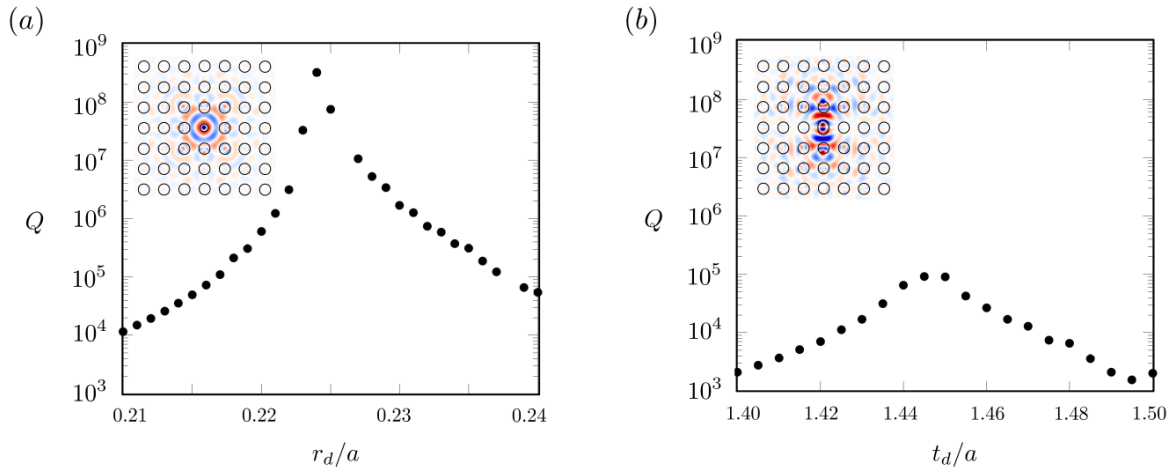

Figure 6.3. (a) Quality factor of the defect mode (irrep A_1) in a supercell with C_{4v} symmetry. The divergence in Q shows the appearance of a BIC. (b) Quality factor of a defect mode (irrep b_2) in a supercell with only C_{2v} symmetry. The lack of divergence indicates that the defect mode is a resonance. The insets show the defect mode profiles for parameter values corresponding to the maximum Q.

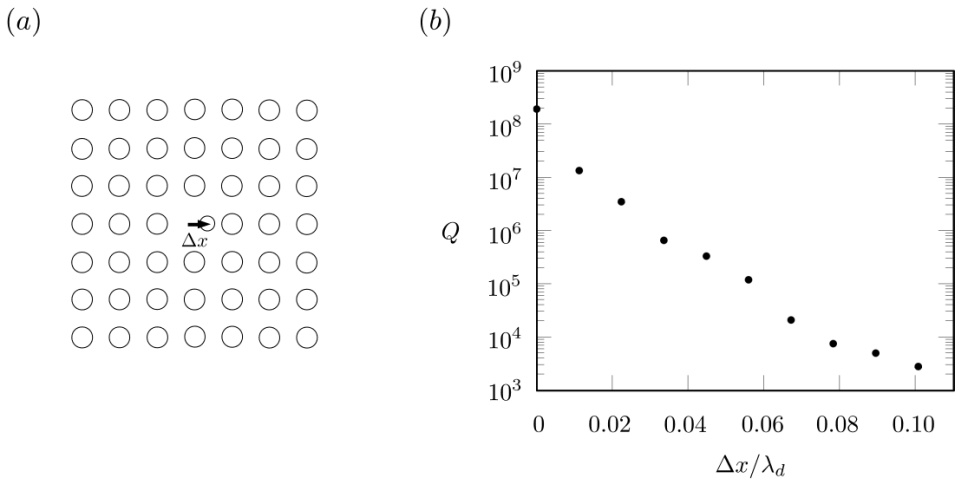

Figure 6.4. (a) Displaced defect site inducing a symmetry breaking in the supercell. (b) Quality factor of the defect mode as a function of the normalized displacement of the defect site.

along the x-direction as shown in Fig. 6.4 (a). Fig. 6.4 (b) shows a plot of the Q-factor as a function of the displacement, Δx, normalized to the wavelength of the defect mode, λ_d. As is expected for any symmetry-protected BIC, this perturbation degrades the Q-factor of the BIC. However, we can see that the defect mode still exhibits high Q-factors for typical PhC slab and fiber fabrication errors, which are much less than $\lambda_d/10$. Therefore, any perturbations that are much smaller than the scale of the wavelength will still allow

the system to exhibit an ultra-high-Q resonance.

6.2.3 Scheme for finding photonic crystals with desired properties

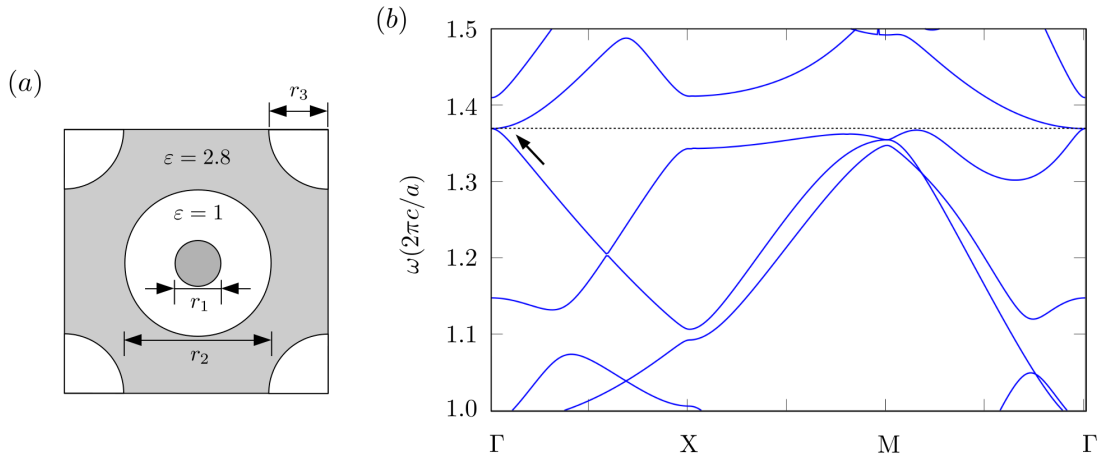

Figure 6.5. (a) The PhC design with three parameters: r_1, r_2, and r_3 made out of a dielectric material with $\varepsilon = 2.8$ (b) TM bands of the PhC shown in (a) for optimized values $r_1/a = 0.0924$, $r_2/a = 0.4066$ and $r_3/a = 0.4238$. The spectrally isolated degeneracy occurs at $\mathbf{\Gamma}$ and is marked with an arrow.

The symmetry mismatch between the defect mode and bulk bands requires the existence of a spectrally-isolated two-fold degeneracy in the bulk PhC, so the question naturally arises: how easy is it to design this bulk band requirement? It is clear from our findings that even simple C_{4v}-symmetric PhC designs are able to satisfy the requirements for reasonably low dielectric contrast and in fact, the feature in the TM bands of the PhC discussed in Fig. 6.2 (a) persists down to $\varepsilon = 3$ for a slightly smaller value of r/a. Furthermore, the search space can be expanded to include C_{3v} and C_{6v} point groups since such quadratic degeneracies can also occur at the $\mathbf{\Gamma}$ point in those lattices, forming two-dimensional irreps of the respective point groups.

We now describe a scheme for finding PhCs with the desired property of hosting spectrally-isolated two-fold degeneracies. The software package MPB [2] outputs the bandgap along a given trajectory in $\mathbf{k}$-space and provides optimization routines to find bandgaps given some free parameters. We can utilize this function to find isolated degeneracies in PhCs. The idea is based on the fact that in a PhC where spectrally-isolated degeneracies occur at HSPs, simply detuning away from HSPs by a small amount $\Delta\mathbf{k}$ results in the opening of a small stop band proportional to $\Delta\mathbf{k}^2$. The structural parameters of the PhC can then be optimized to find these small stop bands.

To demonstrate this, we consider the PhC shown in Fig. 6.5 (a) which consists of three circular discs of radii r_1, r_2 and r_3. The dielectric constant of the high-index material (gray) is $\varepsilon = 2.8$ and that of the low-index material (white) is $\varepsilon = 1$. Using MPB, we run an optimization function on the radii to find the aforementioned stop bands by computing the band structure along the path $(\mathbf{\Gamma} + \Delta\mathbf{k_1}) \rightarrow \mathbf{X} \rightarrow (\mathbf{M} + \Delta\mathbf{k_2}) \rightarrow (\mathbf{\Gamma} + \Delta\mathbf{k_1})$ for some small $\Delta\mathbf{k_1}$, $\Delta\mathbf{k_2}$. A stop band along the detuned path and hence the required degeneracy is found between TM bands 7 and 8 at $\mathbf{\Gamma}$ for $r_1/a = 0.0924$, $r_2/a = 0.4066$ and $r_3/a = 0.4238$, as shown in Fig. 6.5 (b).

6.2.4 BICs enabling slow light in low-contrast photonic crystal fibers

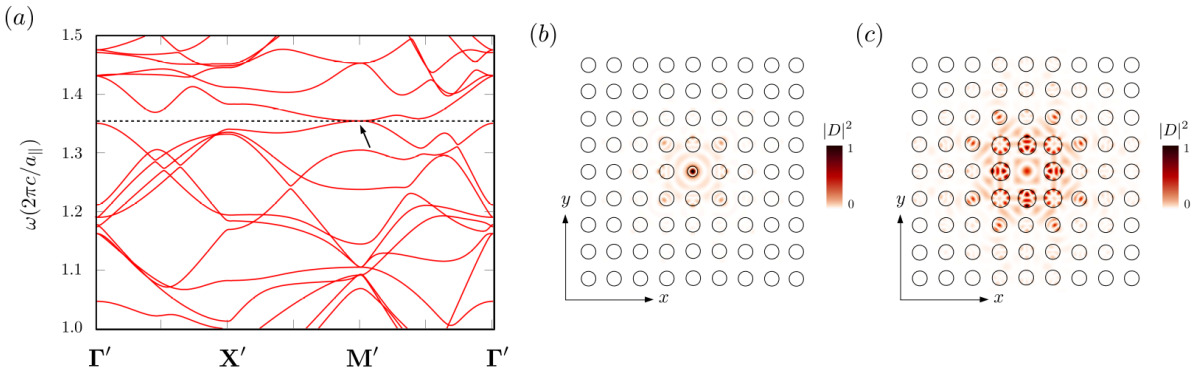

Figure 6.6. (a) The $k_\parallel$-band structure of the defect-free PhC fiber at $k_z = 0.18$ $(2\pi/a_\parallel)$. The spectrally-isolated two-fold degeneracy is marked with an arrow. (b) **D**-field intensity profile of a solid-core fiber BIC mode that occurs at $k_z = 0.18$ $(2\pi/a_\parallel)$. (c) **D**-field intensity profile of a hollow-core-like fiber BIC mode.

For traditional defect modes in 2D PhCs, it suffices to have a bandgap for one polarization, either TE or TM, since they constitute orthogonal subspaces that do not mix. However, for applications such as PhC fibers, (i.e., where the 2D pattern described above is extruded in the third direction, z, and $k_z \neq 0$ generally), the distinction between TE and TM is lost and one requires an overlapping bandgap for both polarizations to confine defect modes. In particular, slow-light PhC fibers rely on the existence of a complete bandgap at $k_z = 0$ which persists for a small range of k_z [184–186]. The arbitrarily small group velocity of the propagating modes in such fibers is achieved by operating near the $k_z = 0$ band edge. These slowly-propagating modes can then be used to strongly enhance interactions of light with either the dielectric material itself or an infiltrated material [187,188], depending on whether the fiber hosts a solid or hollow core. Thus, the design of these fibers requires a high dielectric contrast to open a complete

bandgap at $k_z = 0$. To the best of our knowledge, the smallest contrast for which a complete bandgap exists for 2D PhCs is for $\varepsilon = 4.41$ [189]. We now extend the idea of point-defect-localized BICs to propagating slow-light fiber modes, circumventing the requirement for a complete bandgap.

The fiber design that we propose is identical to an extruded version of the 2D PhC discussed before, now consisting of cylinders extended along the direction of propagation in the fiber. However, since the distinction between TE and TM polarizations is lost, the spectrally-isolated two-fold degeneracy of the bulk must occur in the full band structure in order to create a BIC. This is easily achieved in our structure for a range of k_z values around 0. For instance, Fig. 6.6 (a) shows the band structure of the fiber with $\varepsilon = 4$, $r/a = 0.2755$ at $k_z = 0.18$ $(2\pi/a_\parallel)$, where $a_\parallel$ is the lattice constant in the x, y plane. As before, we introduce a defect site and tune the radius r_d and find a BIC at $r_d/a = 0.230$ for this particular value of k_z. The field profile of the BIC is plotted in Fig. 6.6 (b), forming a solid-core mode and displaying strong confinement to the defect site. Since the spectrally-isolated two-fold degeneracy persists down to $k_z = 0$, the group velocity of this BIC along the length of the fiber ($v_{g_z} = \mathrm{d}\omega/\mathrm{d}k_z$) can be made arbitrarily small with an appropriate choice of r_d. It is also possible to create a hollow-core-like fiber mode where the BIC has reasonable support in the air region. To achieve this, we omit the central defect site and instead tune the radius of the nearest eight sites uniformly so as to maintain C_{4v} and find a BIC as shown in Fig. 6.6 (c).

6.3 Outlook and Conclusion

In conclusion, we have proposed BICs that are exponentially localized to defects beyond bandgaps in both 2D PhCs and structured fibers. The PhC slow-light fiber implementation relaxes the need for bandgaps at $k_z = 0$ and thus allows for a wider range of materials to be used for their implementation. The results presented here have consequences for the general design of PhC-based devices since the requirement for finding bandgaps could potentially be replaced with finding isolated degeneracies at HSPs, which occur more commonly, at lower dielectric contrast and at higher frequencies in the band structure.

The BICs presented here could be experimentally realized in a variety of systems. For example, these principles could be applied to create high-Q nanocavities in gapless PhC slabs where some vertical leakage is unavoidable but in-plane leakage could be suppressed through the symmetry mismatch mechanism. Functionally, these modes would behave similarly to run-of-the-mill PhC slab-based cavities that rely on a bandgap

but could be realizable in alternative structures with potentially lower dielectric contrast. Similarly, the PhC fiber design discussed here could be implemented straightforwardly by complex fiber drawing techniques [168]. Furthermore, such isolated degeneracies are also known to occur in 3D PhCs which could lead to true gapless confinement of light in all directions such as in structures that are precursors to ones with Weyl points [6, 190–192]. Evidently, these BICs rely solely on symmetry considerations and can also be readily realized using other periodic systems such as acoustic crystals, waveguides [179, 193] and coupled resonator arrays.

Chapter 7
Reentrant delocalization transition in 1D photonic quasicrystals

Waves propagating in certain one-dimensional quasiperiodic lattices are known to exhibit a sharp localization transition. In this chapter, we theoretically predict and experimentally observe that the localization of light in one-dimensional photonic quasicrystals is followed by a second delocalization transition for some states on increasing quasiperiodic modulation strength - an example of a reentrant transition. We further propose that this phenomenon can be qualitatively captured by a dimerized tight-binding model with long-range couplings. This chapter is based on work that was done in collaboration with Christina Jörg, Kyle Linn, Megan Goh and Mikael C. Rechtsman [194].

7.1 Overview

Anderson localization is a generic phenomenon of wave localization in randomly disordered media [195]. The presence of localized states implies the cessation of all wave transport in the thermodynamic limit and thus the Anderson model has provided deep insights into the nature of metal to insulator transitions for electrons in disordered solids [196] as well as for light propagating in disordered photonic structures [197]. Specifically in photonics, localization has been proposed and observed in photonic crystals (PhCs) and waveguide arrays, both in truly random [197–202] and quasicrystalline cases [203–205]. Furthermore, this localization phenomenon can be employed for various photonic applications, such as for random nanolasing [206], formation of photonic pseudogaps [207], formation of high Q/V nanocavities [204, 205, 208, 209] and for reducing the crosstalk between waveguides in fiber arrays for endoscopy and telecommunications [210].

It can be shown that in one and two dimensions, an infinitesimal amount of random

disorder causes wave localization but in three dimensions, a sharp transition occurs between extended and localized regimes at a finite value of disorder strength [211, 212]. Such a sharp transition between localized and extended regimes can also occur in one dimension when the random disorder of lattice potentials is replaced by quasiperiodicity. A model first proposed by Aubry and André consists of a one-dimensional lattice with quasiperiodic on-site-energy modulation and nearest-neighbor couplings that exhibits a sharp localization transition [213]. Specifically, the on-site potential for the n-th site in a chain of atoms is modulated according to $E_n = E_0 + \xi \cos(2\pi\beta n)$, where E_0 is the unperturbed on-site energy, β is an irrational number and ξ is the strength of the quasiperiodic modulation. For this simple model, the localization transition occurs for the entire spectrum at a single value of ξ due to a duality between the extended and localized regimes [213].

Extensions of the Aubry-André model with long-range couplings [214–216] and non-Hermiticity [217, 218] were investigated theoretically and found to possess single-particle mobility edges and consequently intermediate regimes, where both extended and localized states co-exist. Moreover, some dimerized tight-binding models [218–222] and driven Aubry-André systems [223] were recently found to exhibit a second reentrant transition of some states back to the same localization regime. Simple two-component one-dimensional PhCs can be thought of as naturally dimer-like due to the patterning of their different dielectrics and may exhibit non-Hermiticity from gain or radiative loss. They are therefore a potentially useful platform for exploring the rich localization physics in complex models.

In this chapter, we experimentally demonstrate a surprising localization phenomenon in multi-layer structures with quasiperiodic thickness modulation, i.e., one-dimensional photonic quasicrystals (PhQCs). In particular, we observe that in addition to the complete inhibition of transmission corresponding to a sharp localization transition, there is a second transition to an extended regime upon increasing the quasiperiodic modulation strength. The experimental signature of this is the complete recovery of transmission through the structure as the quasiperiodic modulation increases beyond the localized regime. This reentrant delocalization transition is not known to occur in random potentials and is a unique feature of quasicrystalline systems. To further explore the reentrant transition, we develop a tight-binding model inspired by our PhQCs, that captures the physics of localization and delocalization in our system.

7.2 Results

7.2.1 Photonic quasicrystal states, their localization measure and transmission spectra

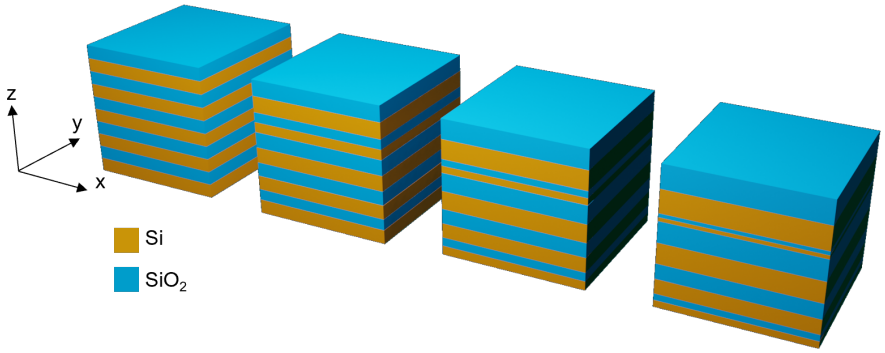

Figure 7.1. Schematic of multi-layer photonic structures made out of Si and SiO_2 layers. The structures have increasing quasiperiodic modulation of layer thicknesses (from left to right); the leftmost structure is a perfect one-dimensional photonic crystal and the rest are photonic quasicrystals.

The system considered here is shown in Fig. 7.1 and consists of a set of multi-layer structures made out of two materials, silicon and silica (SiO_2), with refractive indices $n_{\mathrm{Si}} = 3.5$ and $n_{\mathrm{SiO_2}} = 1.5$, respectively. These layers are stacked along the z-direction and define the dielectric function, $\epsilon(z)$. When propagation purely along the z-direction is considered, this system is described by the following Maxwell eigenvalue problem for a single scalar field $\mathcal{H}(z)$ [3, 4]:

$$-\partial_z \left(\frac{1}{\epsilon(z)} \partial_z \right) \mathcal{H}(z) = \left(\frac{\omega}{c} \right)^2 \mathcal{H}(z), \tag{7.1}$$

where $\mathbf{H}_{\mathrm{TE}} = \mathcal{H}(z)\hat{\mathbf{x}}$ and $\mathbf{H}_{\mathrm{TM}} = \mathcal{H}(z)\hat{\mathbf{y}}$ are the TE- and TM-polarized magnetic field solutions respectively, with frequency eigenvalue ω.

Motivated by the Aubry-André model, we modulate the thicknesses of each layer in a unit cell, defined as a pair of neighboring Si and SiO_2 layers, according to

$$t_n = t_0[1 + A\cos(2\pi\beta n)], \tag{7.2}$$

where $n \in \{1, 2, ..., N\}$ identifies a pair of layers, $2N$ is the total number of layers, A is the strength of the spatial modulation and β is the closest Diophantine (rational)

approximation to the golden mean, $\phi = (1 + \sqrt{5})/2$, for a given value of system size, N.

When $A = 0$, all layers have the same thickness t_0 and the system is a 1D PhC with a lattice constant of $a = 2t_0$, whereas for non-zero values of A, the integer sampling frequency of the cosine term and the irrational modulation frequency β provide two competing and incommensurate periods that result in a 1D PhQC. In the latter case, the average lattice constant $\langle a \rangle = 2t_0$ provides a convenient length scale. We note that since A modulates the thicknesses of layers, it is a bounded parameter with $|A| \leq 1$.

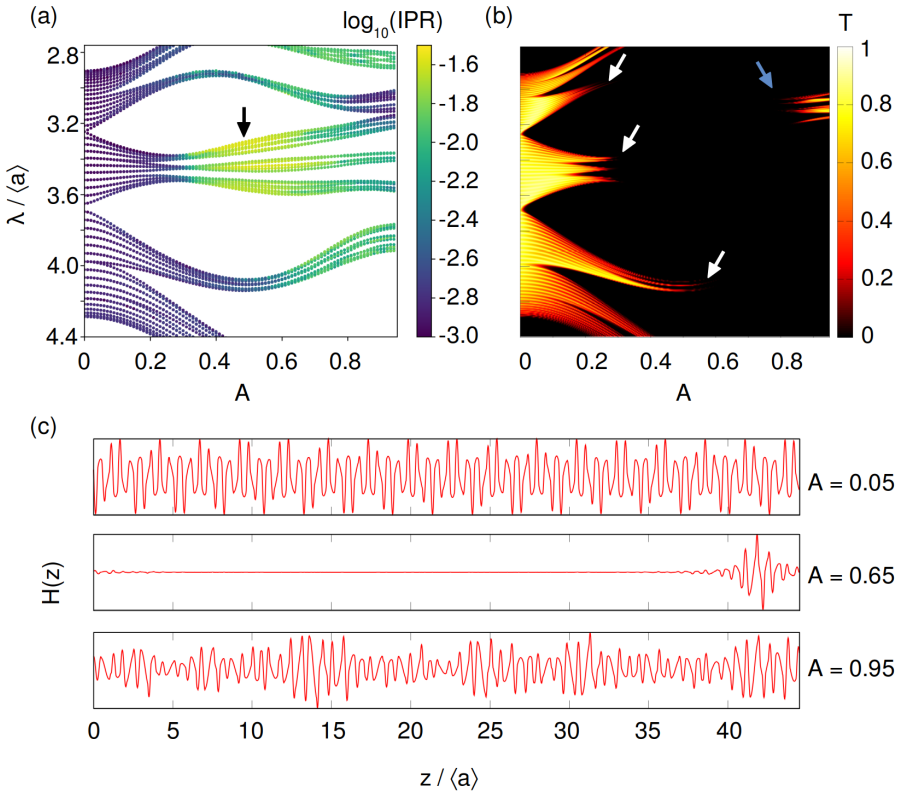

Figure 7.2. (a) Eigenvalue spectrum of the PhQC states and their corresponding IPR as a function of A for $N = 89$. (b) The transmission spectrum as a function of A for $N = 89$. Localization of various states corresponds to sharp drops in transmission (white arrows). Some states undergo a second delocalization transition around $A = 0.8$, which results in a sharp recovery of transmission (blue arrow). (c) $\mathcal{H}(z)$-field profiles of the state marked with the black arrow in (a), for various values of A.

We obtain the states of our PhQCs using the plane-wave expansion method, as implemented in the open source software package MIT Photonic Bands (MPB) [2], and calculate their inverse participation ratios (IPR) given by

$$\mathrm{IPR}_p = \frac{\int |\mathcal{H}_p(z)|^4 dz}{\left[\int |\mathcal{H}_p(z)|^2 dz\right]^2}, \tag{7.3}$$

where $\mathcal{H}_p$ is the scalar field in (7.1), corresponding to the p-th state and the integral is taken over the entire finite system. IPR is a measure of localization of states, where small (large) values of IPR indicate extended (localized) states.

The results for a system size of $N = 89$ are shown in Fig. 7.2. Figure 7.2 (a) shows a plot of the eigenvalue spectrum of the PhQC states as a function of A and their corresponding IPR. In this plot, we focus on states corresponding to the second band in the PhC limit (i.e., at $A = 0$), and convert their corresponding frequency eigenvalues to dimensionless wavelength. For small values of A ($A < 0.3$), the states are extended since the structure may be thought of as being crystalline with a small quasicrystalline perturbation. For larger values of A, the states undergo transitions to a localized regime, as indicated by a sharp increase in their IPR. However, as seen from Fig. 7.2 (a), these transitions do not all occur at the same value of A. Moreover, for some states around $\lambda/\langle a \rangle = 3.2$ and $A = 0.8$, we observe a sharp reduction in IPR on further increasing A, marking a reentrant transition to a second extended regime for these states. In Fig. 7.2 (c), we also examine the $\mathcal{H}(z)$-field profile for one such state that undergoes a reentrant transition, marked by the arrow in Fig. 7.2 (a). The field profiles show the transition from extended to localized and back to extended as A is increased.

Our system thus exhibits some crucial distinctions from the simple Aubry-André model. Each pair of layers that forms a unit cell in our PhQCs is not well approximated as a resonator or atomic potential that is evanescently coupled only to its nearest neighbors. If the PhQC corresponds to a tight-binding model at all, it must be thought of as possessing long-range couplings that can be accurately computed using Wannier-function methods [224]. The presence of these effectively long-range couplings creates single-particle mobility edges that result in intermediate regimes where both extended and localized states co-exist [214]. In fact, we find that due to the bounded nature of the quasiperiodic modulation strength via the parameter A, a large part of the spectrum of the PhQC is in an intermediate regime [216]. Moreover, the states corresponding to the lowest band of the PhC limit never localize for any value of A up to its bounds. This is because PhQCs act as effectively homogeneous dielectric media at long wavelengths. Finally, the presence of a reentrant transition suggests the breakdown of the duality between the localized and extended regimes that exists in the simple Aubry-André model.

Since the localization of states causes the cessation of wave transport, we explore its consequences in the transmission spectrum of the PhQCs. Fig. 7.2 (b) shows a plot of the transmission spectrum of the PhQCs as a function of A, calculated using a transfer matrix approach. We see that the localization transitions from Fig. 7.2 (a) correspond

to the vanishing of transmission through the structures. This occurs because the system size is larger than the localization length of the localized states and as such these states are unable to form a transmission channel across the structures. Furthermore, we also see a recovery of transmission around $\lambda/\langle a \rangle = 3.2$, which corresponds to the reentrant transition of some of the states to an extended regime. This observation is not a finite size effect and persists for much larger system sizes. PhQCs and their transmission spectra therefore provide an accessible experimental setting in which to explore localization phenomena in one-dimensional systems.

7.2.2 Experimental results

For the fabrication of 1D PhQCs, we employ the plasma-enhanced chemical vapor deposition (PECVD) process to deposit alternating layers of silicon (Si) and silica (SiO_2). The layers are deposited onto a glass substrate (Corning 18 mm square microscope glass cover slide). Si is deposited from Ar and SiH_4 precursor gases at 220 °C and a pressure of 4.5 Torr, while silica is deposited from N_2O and SiH_4 precursor gases at 300 °C and pressure of 3.5 Torr. The thicknesses of the layers are controlled by the deposition time. We fabricate a total of ten samples with $\langle a \rangle = 0.25\,\mu m$, $t_0 = 0.125\,\mu m$, $N = 13$, $\beta = 21/13$ and varying values of A. A scanning electron microscope (SEM) image of a typical sample is shown in Fig. 7.3 (a).

To characterize the fabrication imperfections in our system and show that the observed features are robust against fabrication disorder, we extract the layer thicknesses of one of the samples from SEM images and compare them with the targeted thicknesses given by Eq. (2) in the main text. We observe random fluctuations in the layer thicknesses with respect to the target thickness by a maximum of ±8% and an average of 2%. This is most likely caused by the fabrication process, where the chemical reaction, and thus the layer formation, is controlled purely by a timed precursor release into the chamber (a process which inherently is prone to fluctuations). We find that these fabrication errors are not large enough to cause any meaningful deviation of the observed localization features compared to simulations.

For the measurements, a collimated, unpolarized laser beam is sent through the PhQCs at normal incidence, and the transmitted power is measured via a powermeter (Thorlabs S120c). To sweep through the wavelengths in the range of 690 nm to 1100 nm, a SuperK EVO white light laser (NKT Photonics) and a SuperK Select filter box are used. The transmitted power is normalized to that from the bare glass substrate. The measured transmission spectrum is shown in Fig. 7.3 (b), along with the simulation results for

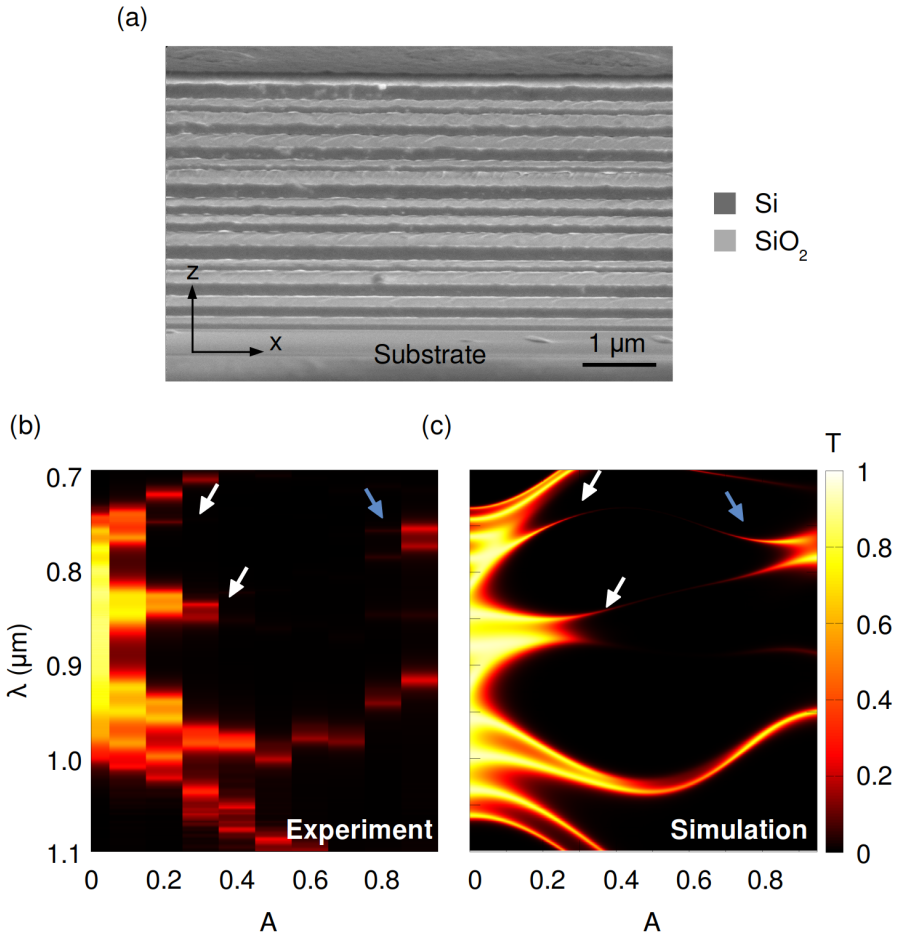

Figure 7.3. (a) Scanning electron microscope (SEM) image of a cut through a typical one-dimensional photonic quasicrystal fabricated by PECVD. Both layers in a pair of neighboring Si and SiO_2 layers have identical thicknesses. The thickness values of each such pair are modulated according to Eq. (7.2). (b) Experimentally measured transmission spectrum as a function of A for $N = 13$. (c) Simulated transmission spectrum as a function of A for $N = 13$. In (b) and (c), the localization transitions are marked with white arrows and the reentrant delocalization transition is marked with a blue arrow.

comparison in Fig. 7.3 (c). We find that despite the relatively small system size, the localization transitions for states near $\lambda \sim 0.85$ and $0.75\,\mu$m are clearly observed as the sharp inhibition of transmission. Furthermore, the second transition to an extended regime near $\lambda \sim 0.78\,\mu$m is observed as a sharp recovery of transmission for $A > 0.8$. The states near $\lambda \sim 1\,\mu$m are localized for $A > 0.5$, however the system size in the experiment is smaller than the localization length of these states and as such we measure finite transmission around this wavelength. Therefore it would be possible in principle to extract the localization length of states directly from the transmission spectrum of PhQCs by varying the system size.

7.3 Tight-binding model

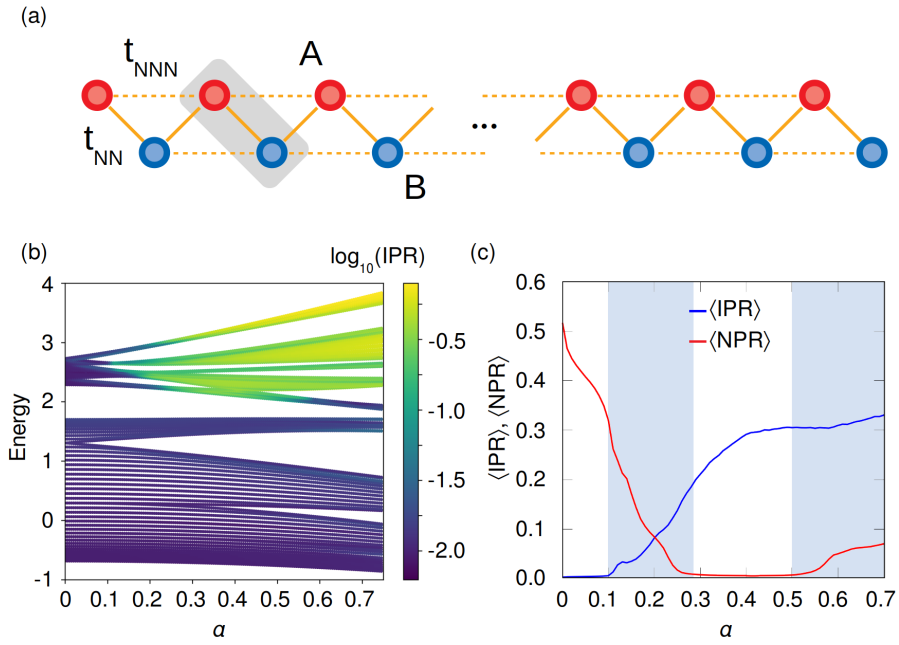

Figure 7.4. (a) Schematic of the tight binding model. The dimerized unit cell for the periodic system ($\alpha = 0$) is highlighted. The solid (dotted) lines represent nearest-neighbor (next-nearest-neighbor) couplings. (b) The energy spectrum and IPR of the corresponding states of the model for $E_{i,A} = 1$, $E_{i,B} = 2$, $t_{\mathrm{NN}} = 0.7$, $t_{\mathrm{NNN}} = 0.35$ and $N = 89$. The states of the second band exhibit a mobility edge and are localized for $0.25 < \alpha < 0.6$. Some states of this band undergo a reentrant delocalization transition at $\alpha \sim 0.6$ (c) A plot of the $\langle \mathrm{IPR} \rangle$ and $\langle \mathrm{NPR} \rangle$ for the states of the second band. The highlighted areas indicate intermediate regimes, where both $\langle \mathrm{IPR} \rangle$ and $\langle \mathrm{NPR} \rangle$ are non-zero, and localized and extended states co-exist.

To further explore the observed localization features, we develop a tight-binding model that qualitatively captures the physics of localization in our PhQCs. In particular, we consider a 1D quasiperiodic model with nearest and next-nearest neighbor couplings given by the Hamiltonian

$$\begin{aligned} H = & \sum_{j=A,B} \sum_{i=1}^{N} E_{i,j} \left[1 + \alpha \cos(2\pi\beta i)\right] n_{i,j} \\ & - t_{\mathrm{NN}} \sum_{i=1}^{N} \left(c_{i,A}^{\dagger} c_{i,B} + \mathrm{h.c.} \right) - t_{\mathrm{NN}} \sum_{i=1}^{N-1} \left(c_{i,B}^{\dagger} c_{i+1,A} + \mathrm{h.c.} \right) \\ & - t_{\mathrm{NNN}} \sum_{j=A,B} \sum_{i=1}^{N-1} \left(c_{i,j}^{\dagger} c_{i+1,j} + \mathrm{h.c.} \right), \end{aligned} \tag{7.4}$$

where $c^{\dagger}_{i,j}$, $c_{i,j}$ and $n_{i,j}$ are respectively the creation, annihilation and number operators on site i of sublattice $j = A, B$. t_{NN}, t_{NNN} are the nearest- and next-nearest-neighbor couplings respectively and $E_{i,j}$ are the unperturbed on-site energies of site i of sublattice j. This lattice of $2N$ sites is shown schematically in Fig. 7.4 (a). We choose $E_{i,A} = 1$ as the energy scale and set $\beta = (1 + \sqrt{5})/2$. α is an unbounded parameter that governs the strength of the quasiperiodic modulation of the on-site energies and we choose $E_{i,B} \neq E_{i,A}$ to introduce dimerization, akin to the two different layers in the PhQCs.

We plot the IPR of the states of this model for $N = 89$ in Fig. 7.4 (b), where we observe some important qualitative similarities with our PhQCs. The states of the lower band stay extended until a much larger value of α, compared to the upper band, similar to the lowest two bands in the PhQCs. We also observe that the states of the upper band exhibit mobility edges and an intermediate regime, before undergoing a transition to a completely localized regime at $\alpha \sim 0.25$. Moreover, some states of this band undergo a second transition at $\alpha \sim 0.6$ and remain extended for a range of α values. Eventually all states of this model become localized for a large enough value of α ($\alpha > 2$). We find that these features are generic and persist for a range of parameters of the model.

We also calculate the average IPR and average normalized participation ratio (NPR) for a set of M states, given by

$$\langle \mathrm{IPR} \rangle = \frac{1}{M} \sum_{n=1}^{M} \sum_{i=1}^{2N} |\psi_{n,i}|^4, \tag{7.5}$$

$$\langle \mathrm{NPR} \rangle = \frac{1}{M} \sum_{n=1}^{M} \left(2N \sum_{i=1}^{2N} |\psi_{n,i}|^4 \right)^{-1}, \tag{7.6}$$

where $|\psi_{n,i}\rangle$ is the normalized n-th eigenstate of H and i labels the sites. The extended regime is characterized by near-zero $\langle \mathrm{IPR} \rangle$ and non-zero $\langle \mathrm{NPR} \rangle$ and vice versa for the localized regime. A non-zero value for both $\langle \mathrm{IPR} \rangle$ and $\langle \mathrm{NPR} \rangle$ implies the presence of an intermediate regime in the spectrum. The plot of $\langle \mathrm{IPR} \rangle$ and $\langle \mathrm{NPR} \rangle$ for the states of the upper band is shown in Fig. 7.4 (c). Comparing this plot with Fig. 7.4 (b), we can see that the first intermediate regime arises due to a moblity edge and the second intermediate regime arises due to a reentrant delocalization transition for the lowest lying states of the band.

Through this model, we see that a combination of staggered potentials and long-range couplings, competing with quasiperiodicity, can cause the delocalization of previously localized states for a range of parameter values. These findings are consistent with other models with similar qualities that are known to host reentrant transitions [219–221].

7.4 Conclusion

In conclusion, we have observed a reentrant delocalization transition – a feature that is not present in the standard Aubry-André model – in 1D PhQCs with an Aubry-André-type quasiperiodic modulation by measuring their transmission spectra. The PhQCs and their transmission spectra thus provide a means to experimentally explore more complex models with richer localization physics, as compared with simple nearest-neighbor tight-binding models. Inspired by the PhQCs, we have also explored the localization features of our system in a tight-binding setting, in order to lend physical insight into the nature of the transition. In the future, it will be interesting to explore localization in passive non-Hermitian 1D PhQCs enabled via a patterning of lossy dielectric materials. Furthermore, examining localized states in higher dimensional realizations of PhQCs is warranted since it could lead to better-performing photonic nanocavities with lower index materials.

Chapter 8
Summary

In this dissertation, we presented a series of studies examining various phenomena in photonic crystals. In chapter 1, we reviewed the mathematical treatment of photonic crystals and elements of topological band theory.

In chapter 2, we presented the experimental realization of a charge-2 Weyl point in a chiral woodpile photonic crystal. The three-dimensional photonic crystal was fabricated using a state-of-the-art 3D micro-printing technique using the Nanoscribe Photonic Professional GT printer. We showed that despite the absence of a band gap around the Weyl point due to the low index contrast, it was possible to observe the dispersion features associated with the Weyl point in the reflection spectrum of the photonic crystal.

In chapter 3, we observed the splitting of this charge-2 Weyl point into two charge-1 Weyl points by breaking the protecting non-symmorphic symmetry of the structure. Rather than introducing random perturbations to the system, we carefully introduced defects that preserved several other symmetries while breaking only the non-symmorphic symmetry. This restricted the splitting to occur along high-symmetry directions in momentum space and allowed for unprecedented control over the location of Weyl points in photonic crystals. Moreover, the experiments were performed at technologically-relevant near-infrared wavelengths.

In chapter 4, we developed a complete classification of topological bands in one- and two-dimensional C_n-symmetric photonic crystals, with and without time-reversal symmetry. Our approach followed previous works in electronic systems and relied on constructing symmetry-indicator invariants that only require looking at symmetry representations of the field eigenmodes at high-symmetry points in momentum space. We then used this classification to proposed a strategy to diagnose and design a wide variety of topological photonic crystals.

In chapter 5, we showed that Chern insulators can have a well-defined notion of relative

polarization, despite their bands being non-Wannierizable. In particular, we showed that electronic boundary charges and adiabatic currents can exist in Chern insulators that are accounted for by a notion of relative polarization. We then demonstrated that these boundary charges are quantized in the presence of inversion symmetry, similar to conventional insulators. Using the classification developed in chapter 4, we predicted that higher-order states induced by polarization should be present at the corners between two Chern insulators with the same Chern number but different values of relative polarization. We then numerically demonstrated the presence of these corner states in an experimentally-realizable Chern photonic crystal.

In chapter 6, we predicted a new method for trapping light within nanocavities embedded inside two-dimensional photonic crystals that do not possess band gaps. We showed that it is possible to engineer the photonic crystal and nanocavity such that light within the cavity is prohibited from leaking away due to a symmetry mismatch with the photonic crystal's modes. This state of light is an example of a "bound state in the continuum" which is a perfectly localized state co-existing with a continuum of propagating states of the photonic crystal. We then showed that the same state can also be used to create slow-light modes in complex photonic crystal fibers with a low index contrast. This opens up the possibility of constructing nanocavities within photonic crystals that are made of lower-index versatile materials like glasses and polymers.

Finally, in chapter 7, we experimentally explored localization and delocalization transitions in one-dimensional photonic quasicrystals. These structures were inspired by the Aubry-André model which exhibits a singular sharp transition between extended and localized regimes. In contrast to the model, we observed the presence of mobility edges that separate the different localization regimes as well as a reentrant delocalization transition that occurs upon increasing the quasiperiodic modulation strength.

Bibliography

[1] Oskooi, A. F., D. Roundy, M. Ibanescu, P. Bermel, J. Joannopoulos, and S. G. Johnson (2010) "Meep: A flexible free-software package for electromagnetic simulations by the FDTD method," *Computer Physics Communications*, **181**(3), pp. 687–702.

[2] Johnson, S. G. and J. D. Joannopoulos (2001) "Block-iterative frequency-domain methods for Maxwell's equations in a planewave basis," *Opt. Express*, **8**(3), pp. 173–190.

[3] Joannopoulos, J. D., S. G. Johnson, J. N. Winn, and R. D. Meade (2008) *Photonic Crystals: Molding the Flow of Light*, second ed., Princeton University Press.

[4] Sakoda, K. (2005) *Optical Properties of Photonic Crystals*, second ed., Springer Series in Optical Sciences Vol. 80.

[5] Vanderbilt, D. (2018) *Berry Phases in Electronic Structure Theory: Electric Polarization, Orbital Magnetization and Topological Insulators*, Cambridge University Press.

[6] Vaidya, S., J. Noh, A. Cerjan, C. Jörg, G. von Freymann, and M. C. Rechtsman (2020) "Observation of a Charge-2 Photonic Weyl Point in the Infrared," *Phys. Rev. Lett.*, **125**, p. 253902.

[7] Berry, M. V. (1984) "Quantal phase factors accompanying adiabatic changes," *Proceedings of the Royal Society of London. A. Mathematical and Physical Sciences*, **392**(1802), pp. 45–57.

[8] Xu, S.-Y., I. Belopolski, N. Alidoust, M. Neupane, G. Bian, C. Zhang, R. Sankar, G. Chang, Z. Yuan, C.-C. Lee, S.-M. Huang, H. Zheng, J. Ma, D. S. Sanchez, B. Wang, A. Bansil, F. Chou, P. P. Shibayev, H. Lin, S. Jia, and M. Z. Hasan (2015) "Discovery of a Weyl fermion semimetal and topological Fermi arcs," *Science*, **349**(6248), pp. 613–617.

[9] Wan, X., A. M. Turner, A. Vishwanath, and S. Y. Savrasov (2011) "Topological semimetal and Fermi-arc surface states in the electronic structure of pyrochlore iridates," *Phys. Rev. B*, **83**, p. 205101.

[10] Armitage, N. P., E. J. Mele, and A. Vishwanath (2018) "Weyl and Dirac semimetals in three-dimensional solids," *Rev. Mod. Phys.*, **90**, p. 015001.

[11] Lv, B. Q., H. M. Weng, B. B. Fu, X. P. Wang, H. Miao, J. Ma, P. Richard, X. C. Huang, L. X. Zhao, G. F. Chen, Z. Fang, X. Dai, T. Qian, and H. Ding (2015) "Experimental Discovery of Weyl Semimetal TaAs," *Phys. Rev. X*, **5**, p. 031013.

[12] Yang, K.-Y., Y.-M. Lu, and Y. Ran (2011) "Quantum Hall effects in a Weyl semimetal: Possible application in pyrochlore iridates," *Phys. Rev. B*, **84**, p. 075129.

[13] Lv, B. Q., N. Xu, H. M. Weng, J. Z. Ma, P. Richard, X. C. Huang, L. X. Zhao, G. F. Chen, C. E. Matt, F. Bisti, V. N. Strocov, J. Mesot, Z. Fang, X. Dai, T. Qian, M. Shi, and H. Ding (2015) "Observation of Weyl nodes in TaAs," *Nature Physics*, **11**, pp. 724–727.

[14] Yang, L. X., Z. K. Liu, Y. Sun, H. Peng, H. F. Yang, T. Zhang, B. Zhou, Y. Zhang, Y. F. Guo, M. Rahn, D. Prabhakaran, Z. Hussain, S.-K. Mo, C. Felser, B. Yan, and Y. L. Chen (2015) "Weyl semimetal phase in the non-centrosymmetric compound TaAs," *Nature Physics*, **11**, pp. 728–732.

[15] Soluyanov, A. A., D. Gresch, Z. Wang, Q. Wu, M. Troyer, X. Dai, and B. A. Bernevig (2015) "Type-II Weyl semimetals," *Nature*, **527**, pp. 495–498.

[16] Lu, L., L. Fu, J. D. Joannopoulos, and M. Soljačić (2013) "Weyl points and line nodes in gyroid photonic crystals," *Nature Photonics*, **7**, pp. 294–299.

[17] Lu, L., Z. Wang, D. Ye, L. Ran, L. Fu, J. D. Joannopoulos, and M. Soljačić (2015) "Experimental observation of Weyl points," *Science*, **349**(6248), pp. 622–624.

[18] Goi, E., Z. Yue, B. P. Cumming, and M. Gu (2018) "Observation of Type I Photonic Weyl Points in Optical Frequencies," *Laser Photonics Rev.*, **12**(2), p. 1700271.

[19] Noh, J., S. Huang, D. Leykam, Y. D. Chong, K. P. Chen, and M. C. Rechtsman (2017) "Experimental Observation of optical Weyl points and Fermi arc-like surface states," *Nature Physics*, **13**, pp. 611–617.

[20] Cerjan, A., S. Huang, M. Wang, K. P. Chen, Y. Chong, and M. C. Rechtsman (2019) "Experimental realization of a Weyl exceptional ring," *Nature Photonics*, **13**(9), pp. 623–628.

[21] Lu, Y., N. Jia, L. Su, C. Owens, G. Juzeliūnas, D. I. Schuster, and J. Simon (2019) "Probing the Berry curvature and Fermi arcs of a Weyl circuit," *Phys. Rev. B*, **99**, p. 020302.

[22] Takahashi, Y., T. Kariyado, and Y. Hatsugai (2019) "Weyl points of mechanical diamond," *Phys. Rev. B*, **99**, p. 024102.

[23] Li, F., X. Huang, J. Lu, J. Ma, and Z. Liu (2018) "Weyl points and Fermi arcs in a chiral phononic crystal," *Nature Physics*, **14**, pp. 30–34.

[24] Meng, X., W.-J. Chen, W.-Y. He, and C. T. Chan (2015) "Synthetic gauge flux and Weyl points in acoustic systems," *Nature Physics*, **11**, pp. 920–924.

[25] Xiao, M., Q. Lin, and S. Fan (2016) "Hyperbolic Weyl Point in Reciprocal Chiral Metamaterials," *Phys. Rev. Lett.*, **117**, p. 057401.

[26] Gao, W., B. Yang, M. Lawrence, F. Fang, B. Béri, and S. Zhang (2016) "Photonic Weyl degeneracies in magnetized plasma," *Nature Communications*, **7**, p. 12435.

[27] Lin, Q., M. Xiao, L. Yuan, and S. Fan (2016) "Photonic Weyl point in a two-dimensional resonator lattice with a synthetic frequency dimension," *Nature communications*, **7**, p. 13731.

[28] Fang, C., M. J. Gilbert, X. Dai, and B. A. Bernevig (2012) "Multi-Weyl Topological Semimetals Stabilized by Point Group Symmetry," *Phys. Rev. Lett.*, **108**, p. 266802.

[29] Chang, M.-L., M. Xiao, W.-J. Chen, and C. T. Chan (2017) "Multiple Weyl points and the sign change of their topological charges in woodpile photonic crystals," *Phys. Rev. B*, **95**, p. 125136.

[30] Takahashi, S., S. Oono, S. Iwamoto, Y. Hatsugai, and Y. Arakawa (2018) "Circularly Polarized Topological Edge States Derived from Optical Weyl Points in Semiconductor-Based Chiral Woodpile Photonic Crystals," *Journal of the Physical Society of Japan*, **87**(12), p. 123401.

[31] Chen, W.-J., M. Xiao, and C. T. Chan (2016) "Photonic crystals possessing multiple Weyl points and the experimental observation of robust surface states," *Nature communications*, **7**, p. 13038.

[32] He, H., C. Qiu, X. Cai, M. Xiao, M. Ke, F. Zhang, and Z. Liu (2020) "Observation of quadratic Weyl points and double-helicoid arcs," *Nature Communications*, **11**.

[33] Fullager, D. B., G. D. Boreman, and T. Hofmann (2017) "Infrared dielectric response of nanoscribe IP-dip and IP-L monomers after polymerization from 250 cm-1 to 6000 cm-1," *Opt. Mater. Express*, **7**(3), pp. 888–894.

[34] Resta, R. (2000) "Manifestations of Berry's phase in molecules and condensed matter," *Journal of Physics: Condensed Matter*, **12**(9), pp. R107–R143.

[35] von Freymann, G., A. Ledermann, M. Thiel, I. Staude, S. Essig, K. Busch, and M. Wegener (2010) "Three-Dimensional Nanostructures for Photonics," *Advanced Functional Materials*, **20**(7), pp. 1038–1052.

[36] Bückmann, T., N. Stenger, M. Kadic, J. Kaschke, A. Frölich, T. Kennerknecht, C. Eberl, M. Thiel, and M. Wegener (2012) "Tailored 3D Mechanical Metamaterials Made by Dip-in Direct-Laser-Writing Optical Lithography," *Advanced Materials*, **24**(20), pp. 2710–2714.

[37] Staude, I., M. Thiel, S. Essig, C. Wolff, K. Busch, G. von Freymann, and M. Wegener (2010) "Fabrication and characterization of silicon woodpile photonic crystals with a complete bandgap at telecom wavelengths," *Opt. Lett.*, **35**(7), pp. 1094–1096.

[38] Liu, V. and S. Fan (2012) "S4 : A free electromagnetic solver for layered periodic structures," *Computer Physics Communications*, **183**, pp. 2233–2244.

[39] Kao, T.-H., L.-Y. C. Chien, and Y.-C. Hung (2015) "Dual circular polarization gaps in helix photonic metamaterials," *Opt. Express*, **23**(19), pp. 24416–24425.

[40] Karakasoglu, I., M. Xiao, and S. Fan (2018) "Polarization control with dielectric helix metasurfaces and arrays," *Opt. Express*, **26**(17), pp. 21664–21674.

[41] Saba, M., M. Thiel, M. D. Turner, S. T. Hyde, M. Gu, K. Grosse-Brauckmann, D. N. Neshev, K. Mecke, and G. E. Schröder-Turk (2011) "Circular Dichroism in Biological Photonic Crystals and Cubic Chiral Nets," *Phys. Rev. Lett.*, **106**, p. 103902.

[42] Takahashi, S., T. Tajiri, Y. Ota, J. Tatebayashi, S. Iwamoto, and Y. Arakawa (2014) "Circular dichroism in a three-dimensional semiconductor chiral photonic crystal," *Applied Physics Letters*, **105**(5), p. 051107.

[43] Wan, X., A. M. Turner, A. Vishwanath, and S. Y. Savrasov (2011) "Topological semimetal and Fermi-arc surface states in the electronic structure of pyrochlore iridates," *Phys. Rev. B*, **83**, p. 205101.

[44] Jörg, C., S. Vaidya, J. Noh, A. Cerjan, S. Augustine, G. von Freymann, and M. C. Rechtsman (2022) "Observation of Quadratic (Charge-2) Weyl Point Splitting in Near-Infrared Photonic Crystals," *Laser & Photonics Reviews*, **16**(1), p. 2100452.

[45] Fang, C., M. J. Gilbert, X. Dai, and B. A. Bernevig (2012) "Multi-Weyl Topological Semimetals Stabilized by Point Group Symmetry," *Phys. Rev. Lett.*, **108**, p. 266802.

[46] Chang, M.-L., M. Xiao, W.-J. Chen, and C. T. Chan (2017) "Multiple Weyl points and the sign change of their topological charges in woodpile photonic crystals," *Phys. Rev. B*, **95**, p. 125136.

[47] Hirschmann, M. M., A. Leonhardt, B. Kilic, D. H. Fabini, and A. P. Schnyder (2021) "Symmetry-enforced band crossings in tetragonal materials: Dirac and Weyl degeneracies on points, lines, and planes," *Phys. Rev. Materials*, **5**, p. 054202.

[48] Chen, T.-G., J.-R. Jiao, H.-Q. Dai, and D.-J. Yu (2018) "Acoustic Weyl points in a square lattice," *Phys. Rev. B*, **98**, p. 214110.

[49] Roy, B., P. Goswami, and V. Juričić (2017) "Interacting Weyl fermions: Phases, phase transitions, and global phase diagram," *Phys. Rev. B*, **95**, p. 201102.

[50] Chua, S.-L., L. Lu, J. Bravo-Abad, J. D. Joannopoulos, and M. Soljačić (2014) "Larger-area single-mode photonic crystal surface-emitting lasers enabled by an accidental Dirac point," *Opt. Lett.*, **39**(7), pp. 2072–2075.

[51] Yang, B., Q. Guo, B. Tremain, R. Liu, L. E. Barr, Q. Yan, W. Gao, H. Liu, Y. Xiang, J. Chen, C. Fang, A. Hibbins, L. Lu, and S. Zhang (2018) "Ideal Weyl points and helicoid surface states in artificial photonic crystal structures," *Science*, **359**(6379), pp. 1013–1016.

[52] Lu, L., Z. Wang, D. Ye, L. Ran, L. Fu, J. D. Joannopoulos, and M. Soljačić (2015) "Experimental observation of Weyl points," *Science*, **349**(6248), pp. 622–624.

[53] Li, F., X. Huang, J. Lu, J. Ma, and Z. Liu (2018) "Weyl points and Fermi arcs in a chiral phononic crystal," *Nature Physics*, **14**(1), pp. 30–34.

[54] Deubel, M., G. von Freymann, and M. Wegener (2004) "Direct laser writing of three-dimensional photonic-crystal templates for telecommunications," *Nature Materials*, **3**(7), p. 444.

[55] Schulz, J., S. Vaidya, and C. Jörg (2021) "Topological photonics in 3D micro-printed systems," *APL Photonics*, **6**(8), p. 080901.

[56] Johnson, S. G. and J. D. Joannopoulos (2001) "Block-iterative frequency-domain methods for Maxwell's equations in a planewave basis," *Opt. Express*, **8**(3), pp. 173–190.

[57] Oakdale, J. S., J. Ye, W. L. Smith, and J. Biener (2016) "Post-print UV curing method for improving the mechanical properties of prototypes derived from two-photon lithography," *Opt. Express*, **24**(24), pp. 27077–27086.

[58] Cerjan, A., C. Jörg, S. Vaidya, S. Augustine, W. A. Benalcazar, C. W. Hsu, G. von Freymann, and M. C. Rechtsman (2021), "Creating Bound States in the Continuum using Three-Dimensional Photonic Crystal Environments," `2104.09603`.

[59] Fullager, D. B., G. D. Boreman, and T. Hofmann (2017) "Infrared dielectric response of nanoscribe IP-dip and IP-L monomers after polymerization from 250 cm-1 to 6000 cm-1," *Opt. Mater. Express*, **7**(3), pp. 888–894.

[60] Ozawa, T., H. M. Price, A. Amo, N. Goldman, M. Hafezi, L. Lu, M. C. Rechtsman, D. Schuster, J. Simon, O. Zilberberg, et al. (2019) "Topological photonics," *Reviews of Modern Physics*, **91**(1), p. 015006.

[61] Lu, L., J. D. Joannopoulos, and M. Soljačić (2014) "Topological photonics," *Nature photonics*, **8**(11), pp. 821–829.

[62] Kim, M., Z. Jacob, and J. Rho (2020) "Recent advances in 2D, 3D and higher-order topological photonics," *Light: Science & Applications*, **9**(1), pp. 1–30.

[63] Rechtsman, M. C., J. M. Zeuner, Y. Plotnik, Y. Lumer, D. Podolsky, F. Dreisow, S. Nolte, M. Segev, and A. Szameit (2013) "Photonic Floquet topological insulators," *Nature*, **496**(7444), pp. 196–200.

[64] Hafezi, M., S. Mittal, J. Fan, A. Migdall, and J. Taylor (2013) "Imaging topological edge states in silicon photonics," *Nature Photonics*, **7**(12), pp. 1001–1005.

[65] Gao, W., X. Hu, C. Li, J. Yang, Z. Chai, J. Xie, and Q. Gong (2018) "Fano-resonance in one-dimensional topological photonic crystal heterostructure," *Optics express*, **26**(7), pp. 8634–8644.

[66] Li, C., X. Hu, W. Gao, Y. Ao, S. Chu, H. Yang, and Q. Gong (2018) "Thermo-optical tunable ultracompact chip-integrated 1D photonic topological insulator," *Advanced Optical Materials*, **6**(4), p. 1701071.

[67] Ota, Y., R. Katsumi, K. Watanabe, S. Iwamoto, and Y. Arakawa (2018) "Topological photonic crystal nanocavity laser," *Communications Physics*, **1**(1), pp. 1–8.

[68] Raghu, S. and F. D. M. Haldane (2008) "Analogs of quantum-Hall-effect edge states in photonic crystals," *Physical Review A*, **78**(3), p. 033834.

[69] Wang, Z., Y. Chong, J. D. Joannopoulos, and M. Soljačić (2009) "Observation of unidirectional backscattering-immune topological electromagnetic states," *Nature*, **461**(7265), pp. 772–775.

[70] Wang, Z., Y. Chong, J. D. Joannopoulos, and M. Soljacic (2008) "Reflection-free one-way edge modes in a gyromagnetic photonic crystal," *Physical review letters*, **100**(1), p. 013905.

[71] Liu, K., L. Shen, and S. He (2012) "One-way edge mode in a gyromagnetic photonic crystal slab," *Optics Letters*, **37**(19), pp. 4110–4112.

[72] Skirlo, S. A., L. Lu, Y. Igarashi, Q. Yan, J. Joannopoulos, and M. Soljačić (2015) "Experimental observation of large Chern numbers in photonic crystals," *Physical review letters*, **115**(25), p. 253901.

[73] Wu, L.-H. and X. Hu (2015) "Scheme for achieving a topological photonic crystal by using dielectric material," *Physical review letters*, **114**(22), p. 223901.

[74] Xie, B., G. Su, H.-F. Wang, F. Liu, L. Hu, S.-Y. Yu, P. Zhan, M.-H. Lu, Z. Wang, and Y.-F. Chen (2020) "Higher-order quantum spin Hall effect in a photonic crystal," *Nature communications*, **11**(1), pp. 1–8.

[75] Barik, S., H. Miyake, W. DeGottardi, E. Waks, and M. Hafezi (2016) "Two-dimensionally confined topological edge states in photonic crystals," *New Journal of Physics*, **18**(11), p. 113013.

[76] Cheng, X., C. Jouvaud, X. Ni, S. H. Mousavi, A. Z. Genack, and A. B. Khanikaev (2016) "Robust reconfigurable electromagnetic pathways within a photonic topological insulator," *Nature materials*, **15**(5), pp. 542–548.

[77] Mattei, M. S., B. Liu, G. A. Mazzei Capote, Z. Liu, B. G. Hacha, T. Osswald, Z. Yu, and R. H. Goldsmith (2022) "Three-Dimensional Printed Planar Polymer Photonic Topological Insulator Waveguides and Their Robustness to Lattice Defects," *ACS Photonics*, **9**(5), pp. 1793–1802.

[78] He, W.-Y. and C. T. Chan (2015) "The emergence of Dirac points in photonic crystals with mirror symmetry," *Scientific reports*, **5**(1), pp. 1–7.

[79] Lin, H. and L. Lu (2020) "Dirac-vortex topological photonic crystal fibre," *Light: Science & Applications*, **9**(1), pp. 1–7.

[80] Huang, X., Y. Lai, Z. H. Hang, H. Zheng, and C. Chan (2011) "Dirac cones induced by accidental degeneracy in photonic crystals and zero-refractive-index materials," *Nature materials*, **10**(8), pp. 582–586.

[81] Xie, K., H. Jiang, A. D. Boardman, Y. Liu, Z. Wu, M. Xie, P. Jiang, Q. Xu, M. Yu, and L. E. Davis (2014) "Trapped photons at a Dirac point: a new horizon for photonic crystals," *Laser & Photonics Reviews*, **8**(4), pp. 583–589.

[82] Hu, L., K. Xie, Z. Hu, Q. Mao, J. Xia, H. Jiang, J. Zhang, J. Wen, and J. Chen (2018) "Experimental observation of wave localization at the Dirac frequency in a two-dimensional photonic crystal microcavity," *Opt. Express*, **26**(7), pp. 8213–8223.

[83] Yang, L., G. Qian, G. Tang, F. Yuan, Z. Zhang, K. Huang, Z. Shi, Q. Qian, and Z. Yang (2019) "Observation of Dirac mode in modified honeycomb hollow core photonic crystal fiber," *Optical Materials*, **89**, pp. 203–208.

[84] Xie, K., W. Zhang, A. D. Boardman, H. Jiang, Z. Hu, Y. Liu, M. Xie, Q. Mao, L. Hu, Q. Li, T. Yang, F. Wen, and E. Wang (2015) "Fiber guiding at the Dirac frequency beyond photonic bandgaps," *Light: Science & Applications*, **4**(6), pp. e304–e304.

[85] Shalaev, M. I., W. Walasik, and N. M. Litchinitser (2019) "Optically tunable topological photonic crystal," *Optica*, **6**(7), pp. 839–844.

[86] Ma, T. and G. Shvets (2016) "All-Si valley-Hall photonic topological insulator," *New Journal of Physics*, **18**(2), p. 025012.

[87] Xi, X., K.-P. Ye, and R.-X. Wu (2020) "Topological photonic crystal of large valley Chern numbers," *Photonics Research*, **8**(9), pp. B1–B7.

[88] Chen, X.-D., W.-M. Deng, F.-L. Shi, F.-L. Zhao, M. Chen, and J.-W. Dong (2019) "Direct observation of corner states in second-order topological photonic crystal slabs," *Physical review letters*, **122**(23), p. 233902.

[89] Xie, B.-Y., G.-X. Su, H.-F. Wang, H. Su, X.-P. Shen, P. Zhan, M.-H. Lu, Z.-L. Wang, and Y.-F. Chen (2019) "Visualization of higher-order topological insulating phases in two-dimensional dielectric photonic crystals," *Physical review letters*, **122**(23), p. 233903.

[90] Xie, B.-Y., H.-F. Wang, H.-X. Wang, X.-Y. Zhu, J.-H. Jiang, M.-H. Lu, and Y.-F. Chen (2018) "Second-order photonic topological insulator with corner states," *Physical Review B*, **98**(20), p. 205147.

[91] Ota, Y., F. Liu, R. Katsumi, K. Watanabe, K. Wakabayashi, Y. Arakawa, and S. Iwamoto (2019) "Photonic crystal nanocavity based on a topological corner state," *Optica*, **6**(6), pp. 786–789.

[92] Liu, F., H.-Y. Deng, and K. Wakabayashi (2018) "Topological photonic crystals with zero Berry curvature," *Physical Review B*, **97**(3), p. 035442.

[93] Luo, J., Z. Du, Y. Guo, C. Liu, W. Zhang, and X. Guo (2021) "Multi-class, multi-functional design of photonic topological insulators by rational symmetry-indicators engineering," *Nanophotonics*.

[94] He, L., Z. Addison, E. J. Mele, and B. Zhen (2020) "Quadrupole topological photonic crystals," *Nature communications*, **11**(1), pp. 1–6.

[95] Zhou, X., Z.-K. Lin, W. Lu, Y. Lai, B. Hou, and J.-H. Jiang (2020) "Twisted quadrupole topological photonic crystals," *Laser & Photonics Reviews*, **14**(8), p. 2000010.

[96] Jin, J., L. He, J. Lu, E. J. Mele, and B. Zhen (2021) "Floquet quadrupole photonic crystals protected by space-time symmetry," *arXiv preprint arXiv:2103.01198*.

[97] de Paz, M. B., M. G. Vergniory, D. Bercioux, A. García-Etxarri, and B. Bradlyn (2019) "Engineering fragile topology in photonic crystals: Topological quantum chemistry of light," *Physical Review Research*, **1**(3), p. 032005.

[98] Han, C., M. Kang, and H. Jeon (2020) "Lasing at multidimensional topological states in a two-dimensional photonic crystal structure," *ACS Photonics*, **7**(8), pp. 2027–2036.

[99] Kim, H.-R., M.-S. Hwang, D. Smirnova, K.-Y. Jeong, Y. Kivshar, and H.-G. Park (2020) "Multipolar lasing modes from topological corner states," *Nature communications*, **11**(1), pp. 1–8.

[100] Bahari, B., A. Ndao, F. Vallini, A. El Amili, Y. Fainman, and B. Kanté (2017) "Nonreciprocal lasing in topological cavities of arbitrary geometries," *Science*, **358**(6363), pp. 636–640.

[101] Chen, Y., Z. Lan, J. Li, and J. Zhu (2021) "Topologically protected second harmonic generation via doubly resonant high-order photonic modes," *Physical Review B*, **104**(15), p. 155421.

[102] Smirnova, D., S. Kruk, D. Leykam, E. Melik-Gaykazyan, D.-Y. Choi, and Y. Kivshar (2019) "Third-harmonic generation in photonic topological metasurfaces," *Physical review letters*, **123**(10), p. 103901.

[103] Iwamoto, S., Y. Ota, and Y. Arakawa (2021) "Recent progress in topological waveguides and nanocavities in a semiconductor photonic crystal platform," *Optical Materials Express*, **11**(2), pp. 319–337.

[104] Lan, Z., J. W. You, and N. C. Panoiu (2020) "Nonlinear one-way edge-mode interactions for frequency mixing in topological photonic crystals," *Physical Review B*, **101**(15), p. 155422.

[105] Shalaev, M. I., W. Walasik, and N. M. Litchinitser (2019) "Optically tunable topological photonic crystal," *Optica*, **6**(7), pp. 839–844.

[106] Zhong, J., K. Wang, Y. Park, V. Asadchy, C. C. Wojcik, A. Dutt, and S. Fan (2021) "Nontrivial point-gap topology and non-Hermitian skin effect in photonic crystals," *Physical Review B*, **104**(12), p. 125416.

[107] Chen, M. L., L. J. Jiang, S. Zhang, R. Zhao, Z. Lan, and E. Wei (2021) "Comparative study of Hermitian and non-Hermitian topological dielectric photonic crystals," *Physical Review A*, **104**(3), p. 033501.

[108] Ryu, S., A. P. Schnyder, A. Furusaki, and A. W. Ludwig (2010) "Topological insulators and superconductors: tenfold way and dimensional hierarchy," *New Journal of Physics*, **12**(6), p. 065010.

[109] Chiu, C.-K., J. C. Teo, A. P. Schnyder, and S. Ryu (2016) "Classification of topological quantum matter with symmetries," *Reviews of Modern Physics*, **88**(3), p. 035005.

[110] Bradlyn, B., L. Elcoro, J. Cano, M. Vergniory, Z. Wang, C. Felser, M. I. Aroyo, and B. A. Bernevig (2017) "Topological quantum chemistry," *Nature*, **547**(7663), pp. 298–305.

[111] Marzari, N., A. A. Mostofi, J. R. Yates, I. Souza, and D. Vanderbilt (2012) "Maximally localized Wannier functions: Theory and applications," *Reviews of Modern Physics*, **84**(4), p. 1419.

[112] Po, H. C., H. Watanabe, and A. Vishwanath (2018) "Fragile topology and wannier obstructions," *Physical review letters*, **121**(12), p. 126402.

[113] Song, Z.-D., L. Elcoro, and B. A. Bernevig (2020) "Twisted bulk-boundary correspondence of fragile topology," *Science*, **367**(6479), pp. 794–797.

[114] Benalcazar, W. A., T. Li, and T. L. Hughes (2019) "Quantization of fractional corner charge in C n-symmetric higher-order topological crystalline insulators," *Physical Review B*, **99**(24), p. 245151.

[115] Po, H. C., A. Vishwanath, and H. Watanabe (2017) "Symmetry-based indicators of band topology in the 230 space groups," *Nature communications*, **8**(1), pp. 1–9.

[116] Benalcazar, W. A., J. C. Y. Teo, and T. L. Hughes (2014) "Classification of two-dimensional topological crystalline superconductors and Majorana bound states at disclinations," *Phys. Rev. B*, **89**, p. 224503.

[117] Cano, J., B. Bradlyn, Z. Wang, L. Elcoro, M. Vergniory, C. Felser, M. I. Aroyo, and B. A. Bernevig (2018) "Building blocks of topological quantum chemistry: Elementary band representations," *Physical Review B*, **97**(3), p. 035139.

[118] Bradlyn, B., L. Elcoro, J. Cano, M. G. Vergniory, Z. Wang, C. Felser, M. I. Aroyo, and B. A. Bernevig (2017) "Topological quantum chemistry," *Nature*, **547**, pp. 298 EP –.

[119] Kohn, W. (1959) "Analytic properties of Bloch waves and Wannier functions," *Physical Review*, **115**(4), p. 809.

[120] Tanaue, H. B. and A. Bruno-Alfonso (2020) "Wannier-function expansion of localized modes in 1D photonic crystals without inversion symmetry," *JOSA B*, **37**(12), pp. 3698–3706.

[121] Romano, M. C., D. R. Nacbar, and A. Bruno-Alfonso (2010) "Wannier functions of a one-dimensional photonic crystal with inversion symmetry," *Journal of Physics B: Atomic, Molecular and Optical Physics*, **43**(21), p. 215403.

[122] Busch, K., S. F. Mingaleev, A. Garcia-Martin, M. Schillinger, and D. Hermann (2003) "The Wannier function approach to photonic crystal circuits," *Journal of Physics: Condensed Matter*, **15**(30), p. R1233.

[123] Romano, M. C., A. Vellasco-Gomes, and A. Bruno-Alfonso (2018) "Wannier functions and the calculation of localized modes in one-dimensional photonic crystals," *JOSA B*, **35**(4), pp. 826–834.

[124] Stollenwerk, T., D. N. Chigrin, and J. Kroha (2011) "Efficient construction of maximally localized photonic Wannier functions: locality criterion and initial conditions," *JOSA B*, **28**(8), pp. 1951–1958.

[125] Gupta, V. and B. Bradlyn (2022) "Wannier-function methods for topological modes in one-dimensional photonic crystals," *Physical Review A*, **105**(5), p. 053521.

[126] Alexandradinata, A., X. Dai, and B. A. Bernevig (2014) "Wilson-loop characterization of inversion-symmetric topological insulators," *Physical Review B*, **89**(15), p. 155114.

[127] Hughes, T. L., E. Prodan, and B. A. Bernevig (2011) "Inversion-symmetric topological insulators," *Phys. Rev. B*, **83**, p. 245132.

[128] Fang, Y. and J. Cano (2021) "Filling anomaly for general two-and three-dimensional C 4 symmetric lattices," *Physical Review B*, **103**(16), p. 165109.

[129] Peterson, C. W., T. Li, W. A. Benalcazar, T. L. Hughes, and G. Bahl (2020) "A fractional corner anomaly reveals higher-order topology," *Science*, **368**(6495), pp. 1114–1118.

[130] Song, Z., Z. Fang, and C. Fang (2017) "(d- 2)-dimensional edge states of rotation symmetry protected topological states," *Physical review letters*, **119**(24), p. 246402.

[131] Thonhauser, T. and D. Vanderbilt (2006) "Insulator/Chern-insulator transition in the Haldane model," *Physical Review B*, **74**(23), p. 235111.

[132] Wang, H.-X., G.-Y. Guo, and J.-H. Jiang (2019) "Band topology in classical waves: Wilson-loop approach to topological numbers and fragile topology," *New Journal of Physics*, **21**(9), p. 093029.

[133] Blanco de Paz, M., C. Devescovi, G. Giedke, J. J. Saenz, M. G. Vergniory, B. Bradlyn, D. Bercioux, and A. García-Etxarri (2020) "Tutorial: Computing topological invariants in 2d photonic crystals," *Advanced Quantum Technologies*, **3**(2), p. 1900117.

[134] Teo, J. C. Y. and C. L. Kane (2010) "Topological defects and gapless modes in insulators and superconductors," *Phys. Rev. B*, **82**, p. 115120.

[135] Teo, J. C. Y. and T. L. Hughes (2013) "Existence of Majorana-Fermion Bound States on Disclinations and the Classification of Topological Crystalline Superconductors in Two Dimensions," *Phys. Rev. Lett.*, **111**, p. 047006.

[136] Li, T., P. Zhu, W. A. Benalcazar, and T. L. Hughes (2020) "Fractional disclination charge in two-dimensional C n-symmetric topological crystalline insulators," *Physical Review B*, **101**(11), p. 115115.

[137] Vaidya, S., W. A. Benalcazar, A. Cerjan, and M. C. Rechtsman (2021) "Point-defect-localized bound states in the continuum in photonic crystals and structured fibers," *Physical review letters*, **127**(2), p. 023605.

[138] Chua, S.-L., L. Lu, J. Bravo-Abad, J. D. Joannopoulos, and M. Soljačić (2014) "Larger-area single-mode photonic crystal surface-emitting lasers enabled by an accidental Dirac point," *Optics Letters*, **39**(7), pp. 2072–2075.

[139] Bravo-Abad, J., J. D. Joannopoulos, and M. Soljačić (2012) "Enabling single-mode behavior over large areas with photonic Dirac cones," *Proceedings of the National Academy of Sciences*, **109**(25), pp. 9761–9765.

[140] Guglielmon, J. and M. C. Rechtsman (2019) "Broadband topological slow light through higher momentum-space winding," *Physical review letters*, **122**(15), p. 153904.

[141] Mann, S. A. and A. Alù (2021) "Broadband Topological Slow Light through Brillouin Zone Winding," *Physical Review Letters*, **127**(12), p. 123601.

[142] Yu, L., H. Xue, and B. Zhang (2021) "Topological slow light via coupling chiral edge modes with flatbands," *Applied Physics Letters*, **118**(7), p. 071102.

[143] Liu, S., A. Vishwanath, and E. Khalaf (2019) "Shift insulators: Rotation-protected two-dimensional topological crystalline insulators," *Physical Review X*, **9**(3), p. 031003.

[144] Bernevig, B. A. and S.-C. Zhang (2006) "Quantum spin Hall effect," *Physical review letters*, **96**(10), p. 106802.

[145] Kane, C. L. and E. J. Mele (2005) "Quantum spin Hall effect in graphene," *Physical review letters*, **95**(22), p. 226801.

[146] Bernevig, B. A., T. L. Hughes, and S.-C. Zhang (2006) "Quantum spin Hall effect and topological phase transition in HgTe quantum wells," *science*, **314**(5806), pp. 1757–1761.

[147] Palmer, S. J. and V. Giannini (2021) "Berry bands and pseudo-spin of topological photonic phases," *Physical Review Research*, **3**(2), p. L022013.

[148] Benalcazar, W. A., B. A. Bernevig, and T. L. Hughes (2017) "Quantized electric multipole insulators," *Science*, **357**(6346), pp. 61–66.

[149] Benalcazar, W. A., B. A. Bernevig, and T. L. Hughes (2017) "Electric multipole moments, topological multipole moment pumping, and chiral hinge states in crystalline insulators," *Physical Review B*, **96**(24), p. 245115.

[150] Wheeler, W. A., L. K. Wagner, and T. L. Hughes (2019) "Many-body electric multipole operators in extended systems," *Phys. Rev. B*, **100**, p. 245135.

[151] Kang, B., K. Shiozaki, and G. Y. Cho (2019) "Many-body order parameters for multipoles in solids," *Phys. Rev. B*, **100**, p. 245134.

[152] Resta, R. (1998) "Quantum-Mechanical Position Operator in Extended Systems," *Phys. Rev. Lett.*, **80**, pp. 1800–1803.

[153] Agarwala, A., V. Juričić, and B. Roy (2020) "Higher-order topological insulators in amorphous solids," *Phys. Rev. Research*, **2**, p. 012067.

[154] Li, C.-A., B. Fu, Z.-A. Hu, J. Li, and S.-Q. Shen (2020) "Topological Phase Transitions in Disordered Electric Quadrupole Insulators," *Phys. Rev. Lett.*, **125**, p. 166801.

[155] Yang, Y.-B., K. Li, L.-M. Duan, and Y. Xu (2021) "Higher-order topological Anderson insulators," *Phys. Rev. B*, **103**, p. 085408.

[156] Benalcazar, W. A. and A. Cerjan (2022) "Chiral-Symmetric Higher-Order Topological Phases of Matter," *Physical Review Letters*, **128**(12), p. 127601.

[157] Yariv, A. (1991) *Optical electronics*, Saunders College Publishing.

[158] Thonhauser, T. and D. Vanderbilt (2006) "Insulator/Chern-insulator transition in the Haldane model," *Physical Review B*, **74**(23), p. 235111.

[159] Coh, S. and D. Vanderbilt (2009) "Electric Polarization in a Chern Insulator," *Phys. Rev. Lett.*, **102**, p. 107603.

[160] Joannopoulos, J. D., P. R. Villeneuve, and S. Fan (1997) "Photonic crystals: putting a new twist on light," *Nature*, **386**(6621), pp. 143–149.

[161] John, S. (1987) "Strong localization of photons in certain disordered dielectric superlattices," *Phys. Rev. Lett.*, **58**, pp. 2486–2489.

[162] Yablonovitch, E. (1987) "Inhibited Spontaneous Emission in Solid-State Physics and Electronics," *Phys. Rev. Lett.*, **58**, pp. 2059–2062.

[163] Noda, S., M. Fujita, and T. Asano (2007) "Spontaneous-emission control by photonic crystals and nanocavities," *Nature Photonics*, **1**(8), pp. 449–458.

[164] Fujita, M., S. Takahashi, Y. Tanaka, T. Asano, and S. Noda (2005) "Simultaneous Inhibition and Redistribution of Spontaneous Light Emission in Photonic Crystals," *Science*, **308**(5726), pp. 1296–1298.

[165] Singh, M. R. (2007) "Controlling spontaneous emission in photonic-band-gap materials doped with nanoparticles," *Phys. Rev. A*, **75**, p. 033810.

[166] Baba, T. (2008) "Slow light in photonic crystals," *Nature Photonics*, **2**(8), pp. 465–473.

[167] Knight, J. C. (2003) "Photonic crystal fibres," *Nature*, **424**(6950), pp. 847–851.

[168] Russell, P. (2003) "Photonic Crystal Fibers," *Science*, **299**(5605), pp. 358–362.

[169] Imada, M., S. Noda, A. Chutinan, T. Tokuda, M. Murata, and G. Sasaki (1999) "Coherent two-dimensional lasing action in surface-emitting laser with triangular-lattice photonic crystal structure," *Applied Physics Letters*, **75**(3), pp. 316–318.

[170] Kurosaka, Y., S. Iwahashi, Y. Liang, K. Sakai, E. Miyai, W. Kunishi, D. Ohnishi, and S. Noda (2010) "On-chip beam-steering photonic-crystal lasers," *Nature Photonics*, **4**(7), pp. 447–450.

[171] Hsu, C. W., B. Zhen, A. D. Stone, J. D. Joannopoulos, and M. Soljačić (2016) "Bound states in the continuum," *Nature Reviews Materials*, **1**(9), p. 16048.

[172] Pankin, P. S., B.-R. Wu, J.-H. Yang, K.-P. Chen, I. V. Timofeev, and A. F. Sadreev (2020) "One-dimensional photonic bound states in the continuum," *Communications Physics*, **3**(1), p. 91.

[173] Taghizadeh, A. and I.-S. Chung (2017) "Quasi bound states in the continuum with few unit cells of photonic crystal slab," *Applied Physics Letters*, **111**(3), p. 031114.

[174] Cerjan, A., C. W. Hsu, and M. C. Rechtsman (2019) "Bound States in the Continuum through Environmental Design," *Phys. Rev. Lett.*, **123**, p. 023902.

[175] Hsu, C. W., B. Zhen, J. Lee, S.-L. Chua, S. G. Johnson, J. D. Joannopoulos, and M. Soljačić (2013) "Observation of trapped light within the radiation continuum," *Nature*, **499**(7457), pp. 188–191.

[176] Lee, J., B. Zhen, S.-L. Chua, W. Qiu, J. D. Joannopoulos, M. Soljačić, and O. Shapira (2012) "Observation and Differentiation of Unique High-Q Optical Resonances Near Zero Wave Vector in Macroscopic Photonic Crystal Slabs," *Phys. Rev. Lett.*, **109**, p. 067401.

[177] Liu, V., M. Povinelli, and S. Fan (2009) "Resonance-enhanced optical forces between coupled photonic crystal slabs," *Opt. Express*, **17**(24), pp. 21897–21909.

[178] Benalcazar, W. A. and A. Cerjan (2020) "Bound states in the continuum of higher-order topological insulators," *Phys. Rev. B*, **101**, p. 161116.

[179] Cerjan, A., M. Jürgensen, W. A. Benalcazar, S. Mukherjee, and M. C. Rechtsman (2020) "Observation of a Higher-Order Topological Bound State in the Continuum," *Phys. Rev. Lett.*, **125**, p. 213901.

[180] Xie, K., H. Jiang, A. D. Boardman, Y. Liu, Z. Wu, M. Xie, P. Jiang, Q. Xu, M. Yu, and L. E. Davis (2014) "Trapped photons at a Dirac point: a new horizon for photonic crystals," *Laser & Photonics Reviews*, **8**(4), pp. 583–589.

[181] Mao, Q., K. Xie, L. Hu, Q. Li, W. Zhang, H. Jiang, Z. Hu, and E. Wang (2016) "Light trapping at Dirac point in 2D triangular Archimedean-like lattice photonic crystal," *Appl. Opt.*, **55**(12), pp. B139–B143.

[182] Mao, Q., K. Xie, L. Hu, Q. Li, W. Zhang, Z. H. Haiming Jiang, and E. Wang (2017) "Light confinement at a Dirac point in honeycomb-like lattice photonic crystal," *Optics Communications*, **384**, pp. 11–15.

[183] Chong, Y. D., X.-G. Wen, and M. Soljačić (2008) "Effective theory of quadratic degeneracies," *Phys. Rev. B*, **77**, p. 235125.

[184] Grgić, J., S. Xiao, J. Mørk, A.-P. Jauho, and N. A. Mortensen (2010) "Slow-light enhanced absorption in a hollow-core fiber," *Opt. Express*, **18**(13), pp. 14270–14279.

[185] Lægsgaard, J. (2011) "Zero-velocity solitons in high-index photonic crystal fibers," *J. Opt. Soc. Am. B*, **28**(1), pp. 37–44.

[186] Oskooi, A. F., J. D. Joannopoulos, and S. G. Johnson (2009) "Zero—group-velocity modes in chalcogenide holey photonic-crystal fibers," *Opt. Express*, **17**(12), pp. 10082–10090.

[187] Donvalkar, P. S., S. Ramelow, S. Clemmen, and A. L. Gaeta (2015) "Continuous generation of rubidium vapor in hollow-core photonic bandgap fibers," *Opt. Lett.*, **40**(22), pp. 5379–5382.

[188] Sparks, J. R., J. L. Esbenshade, R. He, N. Healy, T. D. Day, D. W. Keefer, P. J. A. Sazio, A. C. Peacock, and J. V. Badding (2011) "Selective Semiconductor Filling of Microstructured Optical Fibers," *J. Lightwave Technol.*, **29**(13), pp. 2005–2008.

[189] Cerjan, A. and S. Fan (2017) "Complete photonic band gaps in supercell photonic crystals," *Phys. Rev. A*, **96**, p. 051802.

[190] Lu, L., L. Fu, J. D. Joannopoulos, and M. Soljačić (2013) "Weyl points and line nodes in gyroid photonic crystals," *Nature Photonics*, **7**(4), pp. 294–299.

[191] Wang, L., S.-K. Jian, and H. Yao (2016) "Topological photonic crystal with equifrequency Weyl points," *Phys. Rev. A*, **93**, p. 061801.

[192] Yang, Z., M. Xiao, F. Gao, L. Lu, Y. Chong, and B. Zhang (2017) "Weyl points in a magnetic tetrahedral photonic crystal," *Opt. Express*, **25**(14), pp. 15772–15777.

[193] Plotnik, Y., O. Peleg, F. Dreisow, M. Heinrich, S. Nolte, A. Szameit, and M. Segev (2011) "Experimental Observation of Optical Bound States in the Continuum," *Phys. Rev. Lett.*, **107**, p. 183901.

[194] Vaidya, S., C. Jörg, K. Linn, M. Goh, and M. C. Rechtsman (2022) "Reentrant delocalization transition in one-dimensional photonic quasicrystals," *arXiv preprint arXiv:2211.06047*.

[195] Anderson, P. W. (1958) "Absence of diffusion in certain random lattices," *Physical review*, **109**(5), p. 1492.

[196] Lagendijk, A., B. Van Tiggelen, and D. S. Wiersma (2009) "Fifty years of Anderson localization," *Phys. today*, **62**(8), pp. 24–29.

[197] Segev, M., Y. Silberberg, and D. N. Christodoulides (2013) "Anderson localization of light," *Nature Photonics*, **7**(3), pp. 197–204.

[198] John, S. (1987) "Strong localization of photons in certain disordered dielectric superlattices," *Physical review letters*, **58**(23), p. 2486.

[199] Wolf, P.-E. and G. Maret (1985) "Weak localization and coherent backscattering of photons in disordered media," *Physical review letters*, **55**(24), p. 2696.

[200] Genack, A. and N. Garcia (1991) "Observation of photon localization in a three-dimensional disordered system," *Physical review letters*, **66**(16), p. 2064.

[201] Lahini, Y., A. Avidan, F. Pozzi, M. Sorel, R. Morandotti, D. N. Christodoulides, and Y. Silberberg (2008) "Anderson localization and nonlinearity in one-dimensional disordered photonic lattices," *Physical Review Letters*, **100**(1), p. 013906.

[202] García, P., S. Smolka, S. Stobbe, and P. Lodahl (2010) "Density of states controls Anderson localization in disordered photonic crystal waveguides," *Physical Review B*, **82**(16), p. 165103.

[203] Lahini, Y., R. Pugatch, F. Pozzi, M. Sorel, R. Morandotti, N. Davidson, and Y. Silberberg (2009) "Observation of a localization transition in quasiperiodic photonic lattices," *Physical review letters*, **103**(1), p. 013901.

[204] Alpeggiani, F., L. C. Andreani, and D. Gerace (2015) "Effective bichromatic potential for ultra-high Q-factor photonic crystal slab cavities," *Applied Physics Letters*, **107**(26), p. 261110.

[205] Simbula, A., M. Schatzl, L. Zagaglia, F. Alpeggiani, L. Andreani, F. Schäffler, T. Fromherz, M. Galli, and D. Gerace (2017) "Realization of high-Q/V photonic crystal cavities defined by an effective Aubry-André-Harper bichromatic potential," *APL photonics*, **2**(5), p. 056102.

[206] Liu, J., P. Garcia, S. Ek, N. Gregersen, T. Suhr, M. Schubert, J. Mørk, S. Stobbe, and P. Lodahl (2014) "Random nanolasing in the Anderson localized regime," *Nature Nanotechnology*, **9**(4), pp. 285–289.

[207] Froufe-Pérez, L. S., M. Engel, J. J. Sáenz, and F. Scheffold (2017) "Band gap formation and Anderson localization in disordered photonic materials with structural correlations," *Proceedings of the National Academy of Sciences*, **114**(36), pp. 9570–9574.

[208] Vasco, J. and S. Hughes (2019) "Exploiting Long-Range Disorder in Slow-Light Photonic Crystal Waveguides: Anderson Localization and Ultrahigh Q/V Cavities," *Acs Photonics*, **6**(11), pp. 2926–2932.

[209] Sapienza, L., H. Thyrrestrup, S. Stobbe, P. D. Garcia, S. Smolka, and P. Lodahl (2010) "Cavity quantum electrodynamics with Anderson-localized modes," *Science*, **327**(5971), pp. 1352–1355.

[210] Guglielmon, J. and M. C. Rechtsman (2019) "Inducing maximal localization with fractal waveguide arrays," *Physical Review A*, **99**(6), p. 063807.

[211] Thouless, D. J. (1972) "A relation between the density of states and range of localization for one dimensional random systems," *Journal of Physics C: Solid State Physics*, **5**(1), p. 77.

[212] Abrahams, E., P. Anderson, D. Licciardello, and T. Ramakrishnan (1979) "Scaling theory of localization: Absence of quantum diffusion in two dimensions," *Physical Review Letters*, **42**(10), p. 673.

[213] Aubry, S. and G. André (1980) "Analyticity breaking and Anderson localization in incommensurate lattices," *Ann. Israel Phys. Soc*, **3**(133), p. 18.

[214] Biddle, J., D. Priour Jr, B. Wang, and S. D. Sarma (2011) "Localization in one-dimensional lattices with non-nearest-neighbor hopping: Generalized Anderson and Aubry-André models," *Physical Review B*, **83**(7), p. 075105.

[215] Biddle, J. and S. D. Sarma (2010) "Predicted mobility edges in one-dimensional incommensurate optical lattices: An exactly solvable model of Anderson localization," *Physical review letters*, **104**(7), p. 070601.

[216] Li, X., X. Li, and S. D. Sarma (2017) "Mobility edges in one-dimensional bichromatic incommensurate potentials," *Physical Review B*, **96**(8), p. 085119.

[217] Longhi, S. (2019) "Metal-insulator phase transition in a non-Hermitian Aubry-André-Harper model," *Physical Review B*, **100**(12), p. 125157.

[218] Han, W. and L. Zhou (2022) "Dimerization-induced mobility edges and multiple reentrant localization transitions in non-Hermitian quasicrystals," *Physical Review B*, **105**(5), p. 054204.

[219] Roy, S., T. Mishra, B. Tanatar, and S. Basu (2021) "Reentrant localization transition in a quasiperiodic chain," *Physical Review Letters*, **126**(10), p. 106803.

[220] Roy, S., S. Chattopadhyay, T. Mishra, and S. Basu (2022) "Critical analysis of the reentrant localization transition in a one-dimensional dimerized quasiperiodic lattice," *Physical Review B*, **105**(21), p. 214203.

[221] Padhan, A., M. K. Giri, S. Mondal, and T. Mishra (2022) "Emergence of multiple localization transitions in a one-dimensional quasiperiodic lattice," *Physical Review B*, **105**(22), p. L220201.

[222] Goblot, V., A. Štrkalj, N. Pernet, J. L. Lado, C. Dorow, A. Lemaître, L. Le Gratiet, A. Harouri, I. Sagnes, S. Ravets, et al. (2020) "Emergence of criticality through a cascade of delocalization transitions in quasiperiodic chains," *Nature Physics*, **16**(8), pp. 832–836.

[223] Shimasaki, T., M. Prichard, H. Kondakci, J. Pagett, Y. Bai, P. Dotti, A. Cao, T.-C. Lu, T. Grover, and D. M. Weld (2022) "Anomalous localization and multifractality in a kicked quasicrystal," *arXiv preprint arXiv:2203.09442*.

[224] Gupta, V. and B. Bradlyn (2022) "Wannier-function methods for topological modes in one-dimensional photonic crystals," *Physical Review A*, **105**(5), p. 053521.

Vita

Sachin Vaidya

Education:

- Ph.D. in Physics (Expected), The Pennsylvania State University, 2017-2023
- M.Sc. (5-year integrated), University of Hyderabad, 2012-2017

Publications: (* equal contribution)

- **Sachin Vaidya***, Christina Jörg*, Kyle Linn, Megan Goh, Mikael C. Rechtsman, 'Reentrant delocalization transition in one-dimensional photonic quasicrystals', (under review) arXiv:2211.06047 (2022)
- Christina Jörg*, **Sachin Vaidya***, Jiho Noh, Alexander Cerjan, Shyam Augustine, Georg von Freymann, Mikael C. Rechtsman, 'Observation of Quadratic (Charge-2) Weyl Point Splitting in Near-Infrared Photonic Crystals', Laser & Photonics Reviews, **2100452** (2022)
- Alexander Cerjan*, Christina Jörg*, **Sachin Vaidya**, Shyam Augustine, Wladimir A. Benalcazar, Chia Wei Hsu, Georg von Freymann, Mikael C. Rechtsman, 'Observation of Bound States in the Continuum Embedded in Symmetry Bandgaps', Science Advances, **7 (52)** (2021)
- Julian Schulz, **Sachin Vaidya**, Christina Jörg, 'Topological photonics in 3D micro-printed systems', APL Photonics **6**, 080901 (2021)
- **Sachin Vaidya**, Wladimir A. Benalcazar, Alexander Cerjan, Mikael C. Rechtsman, 'Point-Defect-Localized Bound States in the Continuum in Photonic Crystals and Structured Fibers', Phys. Rev. Lett. **127**, 023605 (2021)
- **Sachin Vaidya***, Jiho Noh*, Alexander Cerjan, Christina, Jörg, Georg von Freymann, Mikael C. Rechtsman, 'Observation of a Charge-2 Photonic Weyl Point in the Infrared', Phys. Rev. Lett. **125**, 253902 (2020)

Selected Awards:

- David C. Duncan Graduate Fellowship in Physics, Penn State, 2022
- Downsbrough Graduate Fellowship in Physics, Penn State, 2021 and 2022
- David H. Rank Memorial Physics Award, Penn State, 2018
- Graduate Teaching Assistant Award, Penn State, 2018
- University Medal in Physics, University of Hyderabad, 2017